Development Of Quantum Cascade Laser (QCL)-Based Spectroscopic Techniques And Their Applications In Trace Gas Analysis

Thesis submitted for the degree of

Doctor of Philosophy (Science)

in

Physics (Experimental)

by

Mithun Pal

Department of Physics
University of Calcutta

2019

Dedicated to My Parents and Supervisor...

Acknowledgement

The present research work has been carried out at Laser Spectroscopy and Biomedical Science Laboratory (LSBSL) of S. N. Bose National Centre for Basic Sciences, Kolkata during the years between 2014 and 2019.

I owe my gratitude to a numerous number of people without whom the accomplishment of the thesis would not be possible. In particular, I would like to express my sincere gratitude to my supervisor Dr. Manik Pradhan for giving me the opportunity to work in his lab and the interesting field of science. I would also like to thank my supervisor for his continuous support and great encouragement in my research work.

I would also like to give thanks to our collaborator Dr. Sujit Chaudhri, AMRI Hospitals, Salt Lake, Kolkata for his fruitful discussion and help in bio-medical studies performed in the hospital.

I would also address my special thanks to Dr. Abhijit Maity for his productive discussion on my research work throughout my journey. I would also thank Sanchi Maithani for her help in experiment days. I am also thankful for my lab seniors: Dr. Chiranjit Ghosh, Dr. Gourab Dutta Banik and Dr. Suman Som for their continuous support and valuable discussions. I would also thank my other lab members: Sayoni Bhattacharya, Akash Das, Biswajit Panda, Swarnava Biswas. Besides, I would like to convey my sincere gratitude to Prof. Debnarayan Jana of the department of physics, Calcutta University, for his motivation in doing research during my post graduate studies. I would also thank Prof. Mainak Gupta of the department of Physics in Asutosh College, Kolkata for giving the motivation for studying Physics in my under graduation days.

I would also like to thank my school friends: Pradipta, Saikat (Das), Arunavo, Saikat (Dhara), Sandeep for staying beside me from school

days to till now. I also convey my gratitude to my friends in B.Sc. and M.Sc. days: Sauradip, Sayan, Sukriti, Atri, Shuvayan, and Ishita. I convey my heartiest gratitude to my fellow SNBNCBS mates for their wonderful company during my hostel days at SNBNCBS for almost five years, in particular, Atanu, Juriti, Samrat, Dhimadri, Prantik, Anuvab, Debabrata, Sandip, Keshab, Mahebub and Shankar da.

I also wish to express my love and gratitude to my parents and my elder sister for their continuous support and encouragement during bad days and good days, without whom the journey would not be possible. I am greatly thankful to my special person in my life, Sayoni for her persistent encouragement and mental support during my PhD tenure, which helped me a lot to overcome difficulties in the research and personal life.

Mithun Pal

Department of Chemical, Biological and Macro-Molecular Sciences,

S. N. Bose Centre for Basic Sciences

Salt lake, Kolkata-700106

India

Abstract

This thesis has been mainly focused on the development of widely tuneable quantum cascade laser based spectroscopic techniques for high sensitive gas detection and their potential applications in atmospheric sensing, biomedical science and high resolution fundamental molecular spectroscopy. First, we developed a high resolution continuous wave cavity ring-down spectrometer (cw-CRDS) coupled with an external cavity continuous-wave quantum cascade laser (cw-EC-QCL) operating between the wavenumber range of 1250 cm^{-1} to 1333 cm^{-1}. We subsequently utilised the EC-QCL coupled cw-CRDS system for monitoring three sulphur isotopes of the H_2S in a small spectral region and evaluated their natural abundances by acquiring high-resolution experimental CRDS spectra of the individual isotopic species. We finally employed our CRDS system for simultaneous monitoring of three important hazardous gases N_2O, CH_4, and H_2S within a small tuning range. Next, we exploited the CRDS system to measure N_2O concentration in human exhaled breath and the gastric environment in ppb range. We subsequently investigated the exhaled breath N_2O excretion dynamics in response to the enzymatic activity of gastric pathogen *H. pylori* for indirect assessment of the infection. We also explored the high resolution C_2H_2 spectroscopy using our *cw*-CRDS system and calculated spectroscopic parameters such as line intensities, N_2 broadening coefficient of transition lines, originating from allowed $(\nu_4+\nu_5)^0$ band and forbidden $(\nu_4+\nu_5)^2$ band.

Next, we developed EC-QCL coupled *2f*-wavelength modulation spectroscopy technique, which has been employed to measure atmospheric CH_4 concentration at different anthropogenic sources by probing the strongest interference-free absorption-line centred at 1327.072 cm^{-1} of the ν_4 fundamental vibrational bands of CH_4. The minimum detectable concentration of 11 ppb was achieved for methane measurement.

Finally, we utilised highly sensitive diode laser spectroscopy for measurement of quadruple water isotopes in drinking water,

gastrointestinal (G.I) fluid and human exhaled breath. Here, we provided the direct evidence of the mass-dependent isotopic fractionation of water in the human GI tract, mass-independent isotope exchange-reaction in the respiratory system by monitoring water isotopic fractionations. This study also provides the experimental evidence of the respired semi-heavy water vapour isotope (i.e. HDO) alteration due to the enzymatic activity of *H. pylori* infection in the GI tract.

List of publications related to thesis work

1. "*Simultaneous monitoring of ^{32}S, ^{33}S and ^{34}S isotopes of H_2S using cavity ring-down spectroscopy with a mid-infrared external-cavity quantum cascade laser*", **M. Pal**, A. Maity, S. Maithani, M. Pradhan, *Journal of Analytical Atomic Spectrometry*, , 34(5), 860-866, (2019)

2. "*Exploring the physiological link of breath N_2O through nitrification and denitrification processes in human gastric juice*", **M. Pal**, S. Maithani, A. Maity, S. Chaudhuri, M. Pradhan, *Journal of breath research*, 13 (1), 016002, (2018)

3. "*A continuous-wave quantum cascade laser near 7.5 µm combined with 2f-wavelength modulation spectroscopy for trace monitoring of ambient CH_4 concentrations*", **M. Pal**, A. Maity, M. Pradhan, *Laser Physics* ,28 (10), (2018)

4. "*Quadruple-isotopic signatures of water-metabolism at physio-biological interface*", **M. Pal**, S. Bhattacharya, A. Maity, S. Chowdhury, M. Pradhan. **(Manuscript in communication, 2019)**

5. "*Accurate measurements of line strengths and air-broadening coefficients in acetylene around 7.5 µm using cavity ring down spectroscopy coupled with QCL*", **M. Pal**, A. Maity, S. Maithani, M. Pradhan. **(Manuscript under preparation, 2019)**

List of Publications (Not included in Thesis Chapters)

1. "*Cavity ring-down spectroscopy using an EC-QCL operating at 7.5 μm for direct monitoring of methane isotopes in air*", A. Maity, **M. Pal**, G. D. Banik, S. Maithani and M. Pradhan, ***Laser Phys. Lett.*** 14,115701, (2017).

2. "*Isotope selective activation: a new insight into the catalytic activity of urease*", S. Maithani, **M. Pal**, A. Maity, M. Pradhan, ***RSC Advances*** 7 (50), 31372-31376, (2017).

3. "*Natural 18O and 13C-urea in gastric juice: a new route for non-invasive detection of ulcers*", A. Maity, **M. Pal**, S. Som, S. Maithani, S. Chaudhuri, M. Pradhan, ***Analytical and bioanalytical chemistry*** 409 (1), 193-200, (2017).

4. "*Molecular hydrogen in human breath: a new strategy for selectively diagnosing peptic ulcer disease, non-ulcerous dyspepsia and Helicobacter pylori infection*", A. Maity, **M. Pal**, S. Maithani, B. Ghosh, S. Chaudhuri, M. Pradhan, ***Journal of breath research*** 10 (3), 03600, (2016).

5. "*An EC-QCL based N_2O sensor at 5.2 μm using cavity ring-down spectroscopy for environmental applications*", G.D. Banik, S. Som, A. Maity, **M. Pal**, S. Maithani, S. Mandal, M. Pradhan, ***Analytical Methods*** 9 (15), 2315-2320, (2017).

6. "*Isotopic evidences of the preferential coordination between $^{12}CO_2$ and urease enzyme*" S. Maithani, A. Maity, **M. Pal**, S. Bhattacharya, G.D. Banik, C. Ghosh, ***Chemical Physics***, 520, 21-26, (2019).

7. "*High-resolution spectral analysis of ammonia near 6.2 μm using a cw EC-QCL coupled with cavity ring-down spectroscopy*", S. Maithani, S. Mandal, A. Maity, **M. Pal**, M. Pradhan, ***Analyst***, 143 (9), 2109-2114, (2018).

8. "*New Strategy for in Vitro Determination of Carbonic Anhydrase Activity from Analysis of Oxygen-18 Isotopes of CO_2*", C. Ghosh, S.

Mandal, **M. Pal**, M. Pradhan, *Analytical chemistry,* 90 (2), 1384-1387, (2017).

9. *"Wavelength modulation spectroscopy coupled with an external-cavity quantum cascade laser operating between 7.5 and 8 µm"* A. Maity, **M. Pal**, S. Maithani, G.D. Banik, M. Pradhan*, Laser Physics Letters,* 15 (4), 045701, (2018).

Conference Publications

10. *"Detection of isotopic $^{12}CH_4$ and $^{13}CH_4$ using cavity ring-down spectroscopy coupled with an external-cavity quantum cascade laser"*, **M. Pal**, A. Maity, S. Maithani, M. Pradhan, *Mid-Infrared Coherent Sources, MT3C. 1.(Conference Processing)* **(2018)**

11. *"Spectroscopic analysis of Nitrous Oxide (N_2O) using Wavelength Modulation technique coupled with a mid-IR Quantum Cascade Laser"*, **M. Pal**, A. Maity, S. Maithani, M. Pradhan, *Proceedings of PHOTONICS-2018, IIT Delhi, 12-15 December, 2018, Paper No.FA1-C2,* **(2018)**

12. *"Ro-vibrational analysis of ammonia at 6.2 µm using high-precision cavity ring-down spectroscopy"*, S. Maithani, A. Maity, **M. Pal**, M. Pradhan, *Optics and Photonics for Energy and the Environment, EW3A,* **(2018)**

Table of Contents

Thesis Title: Development Of Quantum Cascade Laser (QCL)-Based Spectroscopic Techniques And Their Applications In Trace Gas Analysis

Abstract: This thesis has been mainly focused on the development of widely tuneable quantum cascade laser based spectroscopic techniques for high sensitive gas detection and their potential applications in atmospheric sensing, biomedical science and high resolution fundamental molecular spectroscopy. First, we developed a high resolution continuous wave cavity ring-down spectrometer (cw-CRDS) coupled with an external cavity continuous-wave quantum cascade laser (cw-EC-QCL) operating between the wavenumber range of 1250 cm^{-1} to 1333 cm^{-1}. We subsequently utilised the EC-QCL coupled cw-CRDS system for monitoring three sulphur isotopes of the H_2S in a small spectral region and evaluated their natural abundances by acquiring high-resolution experimental CRDS spectra of the individual isotopic species. We finally employed our CRDS system for simultaneous monitoring of three important hazardous gases N_2O, CH_4, and H_2S within a small tuning range. Next, we exploited the CRDS system to measure N_2O concentration in human exhaled breath and the gastric environment in ppb range. We subsequently investigated the exhaled breath N_2O excretion dynamics in response to the enzymatic activity of gastric pathogen *H. pylori* for indirect assessment of the infection. We also explored the high resolution C_2H_2 spectroscopy using our *cw*-CRDS system and calculated spectroscopic parameters such as line intensities, N_2 broadening coefficient of transition lines, originating from allowed $(v_4+v_5)^0$ band and forbidden $(v_4+v_5)^2$ band.

Next, we developed EC-QCL coupled 2*f*-wavelength modulation spectroscopy technique, which has been employed to measure atmospheric CH_4 concentration at different anthropogenic sources by probing the strongest interference-free absorption-line centred at 1327.072 cm^{-1} of the v_4 fundamental vibrational bands of CH_4. The minimum detectable concentration of 11 ppb was achieved for methane measurement.

Finally, we utilised highly sensitive diode laser spectroscopy for measurement of quadruple water isotopes in drinking water, gastrointestinal (G.I) fluid and human exhaled breath. Here, we provided the direct evidence of the mass-dependent isotopic fractionation of water in the human GI tract, mass-independent isotope exchange-reaction in the respiratory system by monitoring water isotopic fractionations. This study also provides the experimental evidence of the respired semi-heavy water vapour isotope (i.e. HDO) alteration due to the enzymatic activity of *H. pylori* infection in the GI tract.

Chapter 1

Introduction

1.1 Background and motivation

Trace gases in the Earth's atmosphere, existing in a small concentration (0.1% in total atmospheric gases), are composed of carbon dioxide (CO_2), methane (CH_4), nitrous oxide (N_2O), ozone (O_3), hydrogen sulphide (H_2S), sulphur dioxide (SO_2) and oxides of nitrogen (NOx). In spite of their low concentrations, they have immense importance in making the stability of the atmosphere. However, deforestation, the industrial revolution, use of fossils fuels and accumulation of waste products in a random manner have accelerated the enhancement of the concentration of those trace constituents during the last two centuries, which eventually causes a climate change. But the concentration of major gases except for water vapour, having concentration more than 99.9% of the terrestrial atmosphere (such as oxygen, nitrogen and the noble gases) remained the same before the existence of mankind. Hence, the quantitative monitoring of those harmful trace gases is very much essential in the current scenario.

Apart from the importance of atmospheric monitoring, trace gas detection in human exhaled breath has paved the way for understanding the physiological metabolism and non-invasive clinical diagnosis. The detection of exhaled air trace constituents has become a promising tool for holistically measuring the physiological status of the patient in real-time comfortably. Typically, the exhaled air contains nearly 2000 trace constituents, out of which most of them are volatile organic compounds (VOCs). Methane, hydrogen sulphide, nitric oxide, nitrous oxide, ammonia and formaldehyde are such important trace molecules present in the exhaled breath. However, the trace concentration lies in parts per

million levels to parts per billion levels in exhaled breath, which has become a challenging task for quantitative detection of them.

Nowadays, laser-based absorption spectroscopy (LAS) technique has become an effective trace gas sensing tool. The LAS has conquered against conventional gas detection systems such as gas chromatography (GC) and mass spectroscopy (MS) technique by offering fast response, high sensitivity and high selectivity with measurement capability up to parts per billion (ppb) to parts per trillion level (ppt). The recent invention of quantum cascade laser (QCL) has given us the opportunity to LAS technique to access the mid-infrared electro-magnetic spectrum (2.5 μm - 25μm), which is considered as a molecular finger-print region. In this region, most of the important trace molecules, which have immense importance in both atmospheric monitoring and exhaled breath diagnosis, have strong fundamental absorption band with less overlapping transition lines.

Therefore, the goal of the present thesis goal is to develop a mid-IR continuous wave (cw) QCL coupled gas sensing method and its real-time applications in trace gas monitoring. In this thesis, we have demonstrated the development of two highly sensitive LAS based gas detection techniques i.e. cavity ring-down spectroscopy (CRDS) and wavelength modulation spectroscopy (WMS) coupled with an external cavity (EC) cw-QCL working at 7.5-8 μm. The reason behind choosing such wavelength region is that most of the atmospheric pollutants and breath bio markers such as CH_4, C_2H_2, H_2S, H_2O_2, N_2O and their isotopes have strong fundamental absorption bands in this wavelength window. However, this new-generation laser-based technique also provides the opportunity to explore the high-resolution spectroscopic investigation of aforementioned important molecular species. We have also described the real time application of water vapour isotopes using another high-sensitive cavity-enhanced technique coupled with near-IR diode laser.

In this thesis, we have monitored four important trace molecules such as H_2S isotopes, N_2O, C_2H_2 and CH_4 using two-developed high-resolution spectroscopy techniques. H_2S and CH_4 molecules have an immense

impact in environmental monitoring. Isotopes of H_2S molecule are the tracers of sulphur flux in the atmosphere, rivers, lake water, and ground water. It also provides the information about biological sulphur cycle, along with origin and nature of fossil fuel. On the other hand, methane (CH_4) is the second most contributing greenhouse gas, which has a global warming potential 25 times higher than carbon dioxide. N_2O is also an important trace molecule in atmospheric science due to its potential in global warming. However, the monitoring of the excretion of N_2O in human breath has significance in biomedical science. In addition, the acetylene (C_2H_2) has astrophysical importance for spectroscopic studies.

1.2 Overview of the thesis

The thesis is aimed at describing in detail the outstanding features of the quantum cascade laser-based gas sensor and its real-time application in the environmental and biomedical science along with high-resolution spectroscopic studies. At first, we have developed cavity ring down spectrometer coupled with quantum cascade laser at 7.5 μm and we employed the spectrometer for monitoring the H_2S isotopes for environmental application, detection of N_2O in exhaled breath and high-resolution spectroscopy study of C_2H_2. Next, we have developed the 2*f*-wavelength modulation spectroscopy (WMS) technique coupled with same QCL for real-time detection of atmospheric CH_4 at different sources. The thesis has been divided into several chapters. The first two chapters cover the basics of quantum cascade lasers, its application in trace gas sensing and a brief overview of infrared laser absorption spectroscopy.

Chapter 4 describes the basic principle of the CRDS technique and its development using cw-EC-QCL. The sensitivity of the developed system and its validation using standard gases have also been demonstrated.

Chapter 5 demonstrates the H_2S isotopes measurement using our developed CRDS setup. The exploration of the natural abundances of three isotopes of sulphur of Na_2S has been demonstrated.

Chapter 6 demonstrates the measurement of trace amount of N_2O dissolved in gastric juice and human exhaled breath using the EC-QCL based CRD spectrometer.

Chapter 7 describes the high-resolution spectroscopic studies of C_2H_2 for evaluation of spectroscopic parameters like line-strength, pressure broadening coefficients and transition dipole moment.

Chapter 8 demonstrates the development of 2*f*-WMS technique and its field deployment efficacy by monitoring CH_4 concentrations at different anthropogenic sources.

Chapter 9 describes the monitoring of water isotopes in drinking water, human exhaled breath and gastric fluid using cavity enhanced absorption spectroscopy (CEAS).

Chapter 10 summarizes all the research work described in the present thesis. The future outlook of the research work has also been described in this chapter.

Chapter2

Quantum cascade laser (QCL) in trace gas sensing

2.1 Introduction

In recent years, the development of Quantum cascade lasers (QCLs) has paved the revolution in trace gas analysis as it can easily access the entire mid-infrared (mid-IR) region, covering 4–12 µm. This is considered to be the molecular fingerprint region; hence the fundamental and combinational vibrational bands of important trace molecules can be probed with unprecedented molecular selectivity and sensitivity. Moreover, other salient features of QCL such as room temperature operation, high optical output power, spectral purity, compactness, mode-hop-free (MHF) broad tunability ($\geqslant$100 cm^{-1}) and extremely narrow linewidth ($\leqslant$0.0002 cm^{-1}) make this laser source popular in the QCL-based absorption spectroscopy (QCLAS) for trace gas monitoring in real time. In this chapter, we will discuss about the operating principle of QCL and its applications in trace molecules detection in atmospheric research and human exhaled breath.

2.2 The architecture and working principles of QCL

The main principle of LASER (Light Amplification by Stimulated Emission of Radiation) is based on the stimulated emission of photons followed by coherent radiation. Laser radiation exhibits high-temporal and spatial coherence with high spectral power densities leading to a significant advantage in various spectroscopic techniques. However, the main criterion for lasing action is the population inversion of electronic states in the active medium followed by substantial optical feedback by a resonator [1]. The conventional semiconductor lasers emit wavelength dependent radiation due to radiative electron-hole recombination

between the valence and conduction band (inter-band transition) for different bandgap of different materials [2-3]. But in Quantum Cascade Laser (QCL), the emission is achieved by utilising intersubband transition of only one type of charge carrier (electrons). Thus, QCL is called as unipolar laser source, of which lasing principle is quite different with respect to the conventional bipolar semiconductor laser. Typically, QCL is made of a superlattice with periodic series of thin layers of varying material compositions, which leads to forming an electric potential gradient across the length of the device. Thus, formation of such one-dimensional multiple quantum well confinement splits the energy level to a number of discrete electronic subbands leading to cascade down the electrons through identical energy steps followed by emitting one photon at every step. As a result, hence the laser emission is occurred with high optical power due to population inversion between those discrete conduction band-excited states successively [4].
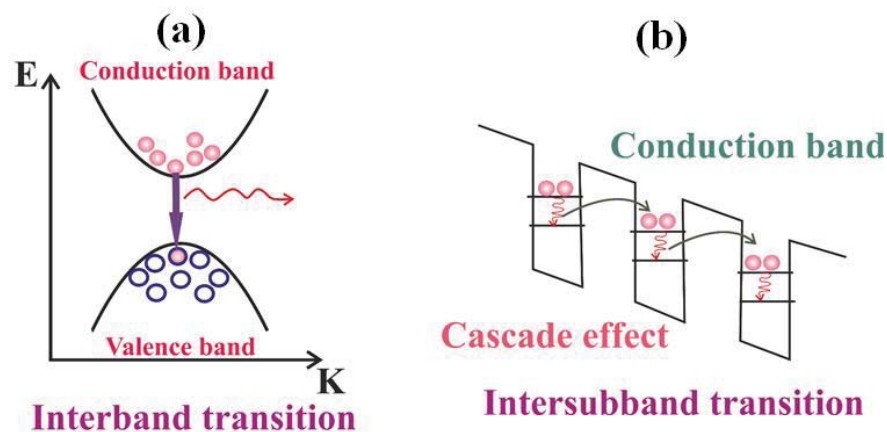
Figure 2.1 *(a) illustrates the conventional electron-hole recombination for the diode laser. (b) demonstrates the cascade effect during the intersubband transition of electrons in a typical QCL structure.*

In 1971, Kazarunov and Suris first conceived the concept of optical gain due to intra-band electron transition [5]. Later in 1994, Faist first demonstrated the QCL experimentally in Bell Laboratories (USA) [6]. The most common material, which is used to fabricate QCL is InGas/AlInAs on an InP substrate [7]. Researchers have also used InGaAs/AlInAs, GaAs/AlGaAs AlGaN/GaN and AlN/GaN materials to manufacture the QCL devices. For production of such crystalline heterostructures with

atomic level resolution, few new-generation crystal growth technologies like molecular beam epitaxy (MBE) and metal-organic vapour phase epitaxy (MOVPE) have been deployed [8-9]. The interesting fact for fabrication of such sophisticated lasing device is that output wavelength from QCL depends on spacing between subbands irrespective of materials used to manufacture, which gives freedom to material technology for mass production requirements [10].

Top Contact Layer (Ti/Au)

Waveguide Layers (lnGaAs)

Cladding (lnP)

Substrate (lnP)

Laser emission

Active region
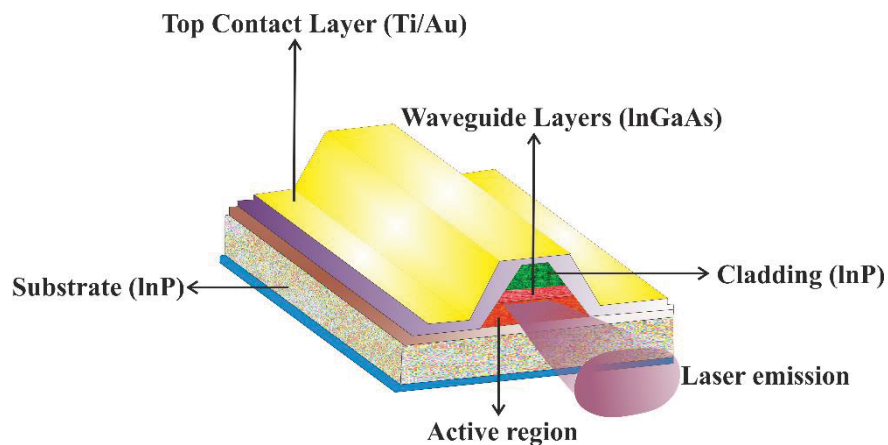
Figure 2.2 *Schematic diagram of material composition of a QCL chip*

Quantum cascade lasers are generally classified into three types, which are Fabry-Pérot, distributed feedback (DFB) and external cavity (EC), depending on the resonator design [11-12]. The overall gain obtained from active region of the QCL is abridged by the sum of all losses, including waveguide losses due to light propagation in laser chip, mirror losses originated from their configuration and losses from selection for a particular emission wavenumber within the available gain curve. In this thesis work, we are concerned about only EC-QCL, as it was employed in the development of spectroscopic techniques. However, other QCL's properties will be elaborated briefly.

In Fabry-Pérot QCL, a bare QCL chip with high reflection coatings on the end surfaces of the laser crest has been exploited. This resonator configuration is considered to be one of the simplest design among other QCLs. However, it emits hundreds of longitudinal modes with wide spectral range (multimode emission), which is detrimental for spectroscopic applications in the gas-phase. Nevertheless, this type of

QCLs has been deployed in liquid-phase analysis, as absorption bands of liquid are much broader than gas [13-14].

The DFB-QCLs was first validated in 1997 by integrating a Bragg grating on the top of the laser ridge along the light propagation direction [15]. The tunability of the DFB-QCL can be achieved up to 5 cm^{-1} by tuning the operational temperature and/or injection current [16] and to overcome the limiting tunability of this type of laser, multiple numbers of DFB-QCLs (DFB-QCL array) can be incorporated simultaneously [17-20]. The associated disadvantage of DFB-QCL is its beam divergence up to 10^0, which needs to be amended by collimation optics. However, its narrowband single mode emission makes it most preferable laser source for gas spectroscopy and use of DFB-QCL array offers broad tunability which is very much helpful for liquid-analytes analysis as well as for multiple trace gas sensing [21-23].
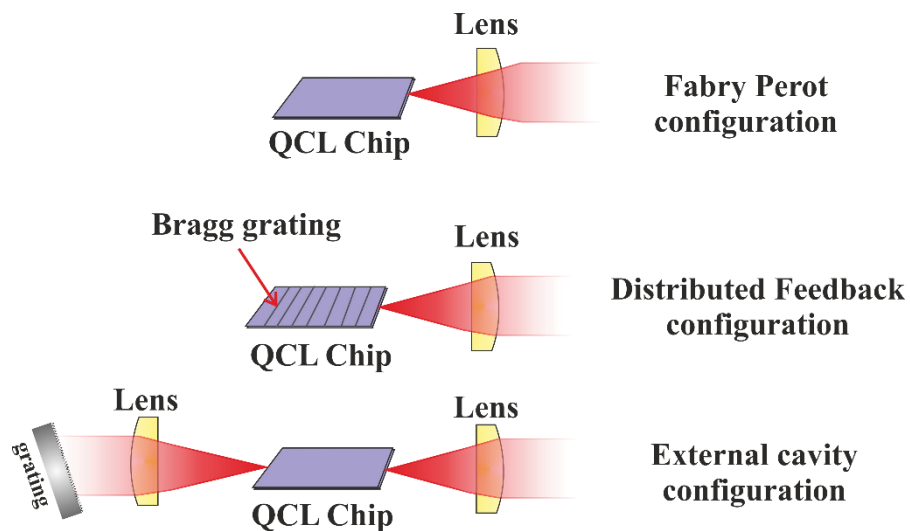
Figure 2.3 *Configuration of different types of QCL*

Next, incorporation of an external cavity coupled with an external diffraction grating in QCL chip overcomes the limited tunability of DFB-QCL and offers several hundreds of wavenumbers of tuning range [24-25]. This broad tuning range from the QCL chip is actually achieved by changing the angle of the diffraction grating. Luo et. al. demonstrated the first EC-QCL at cryogenic temperature in 2001[26] and in the next year 2002, the room temperature operable pulsed mode EC-QCL was reported at 10.4 μm by Totsching et al. [27] The EC-QCLs are classified into three

types depending on their emission characteristics which are pulsed, standard continuous wave (CW) and mode-hop-free (MHF)-CW configurations. But there is a disadvantage present in using pulsed and continuous wave QCL in gas-phase spectroscopy due to mode-hopping phenomena during tuning [28]. Moreover, this unwanted phenomenon is originated from competition between different optical modes to avail the net gain in laser medium leading to distinctive gaps in the emission curve [29-31]. Thus, a mode tracking system has been incorporated in the EC-QCL for exactly matching the diffraction grating angle with external cavity length during the tuning process [28].

2.3 Importance of trace gas sensing with the help of QCL

The trace gases are defined as the gases that exist in small concentrations in a gas mixture. Despite of their low concentration, its quantitative detection has immense importance in numerous fields such as in environmental sensing, trace amounts of explosive detection and non-invasive medical diagnostics by means of exhaled breath analysis. The recent advancement of infrared laser absorption spectroscopy (LAS) has become the most promising tool for quantitative and selective gas detection with demonstrated detection sensitivities ranging from ppmv and ppbv, even pptv levels depending on the detection method employed. Moreover, the invention and advancement of QCL play a paramount roll in trace gas detection as it is capable of accessing entire mid-infrared molecular 'finger-print' region (3-15 μm) and this spectral region is considered to be the choice for high-sensitivity laser absorption spectroscopy [32-33]. Since most of the important trace molecules, being a simple or moderately complex structure, have fundamental ro-vibrational transition frequencies lying in this spectral region (see the figure 2.4). Thus, the transition strengths are several orders of higher magnitude compared to near-IR region leading to high sensitivity measurement [34].
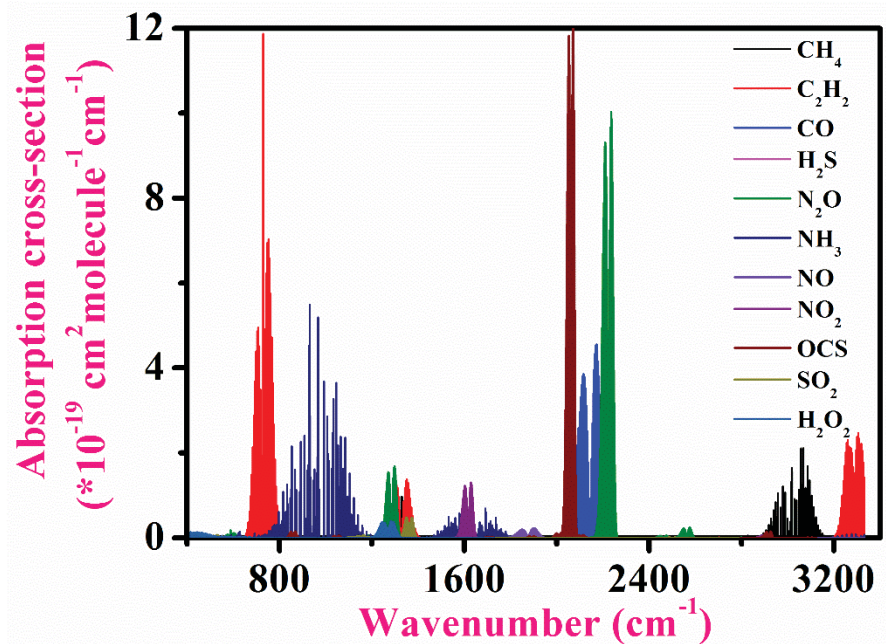
Figure 2.4 *The simulated spectra from the HITRAN database for important trace molecules in the mid-IR electromagnetic region.*

2.3.1 Atmospheric Research

The trace gases play an important role in global warming, reduction of the ozone layer, the formation of photochemical smog and acid rain. They are the cause of several health problems. Hence, public awareness regarding environmental pollution by hazardous atmospheric pollutants and greenhouse gases enroots the demand for trace gas detection devices and systems. The main sources for greenhouse gases and other pollutants present in the Earth's atmosphere are the burning of fossil fuels and different anthropogenic activities. Hence detection and quantification of the composition of trace gases for various scientific, industrial, and environmental purposes are essential. Table 2.1 shows the typical mixing ratios of selected trace gases present in the troposphere **[35-38]**. It has been found that most of the trace gas concentration would normally be in parts per billion (ppb, 10^{-9}) to parts per million (ppm, 10^{-6}) range. Most of the trace molecules present in the atmosphere have strong line strengths due to occurrence of their molecular transitions between ro-vibrational

Table 2.1 *Globally averaged tropospheric concentrations of important trace gases*

Trace Gases	Globally averaged Gas concentration (ppbv)	Atmospheric Lifetime yr
CH_4	1859	10
CO	100	0.2
N_2O	329.9	150
O_3	30-500	Weeks
CCL_2F_2	0.39	111
CCL_3F	0.23	74
CCL_4	0.13	40
NO_x	Highly variable	Days

states in infrared 'fingerprint' region in the exposure of electromagnetic spectrum between 3 and 24 μm. Eventually, this transition forms the absorption spectra consisting of a number of discrete absorption lines for different molecules with or without overlapping features with other molecules and those lines are probed by means of selective detection of a particular trace molecule by utilizing very narrow line-width of QCL for specific detection strategies. The summary of QCL applications in atmospheric trace measurement has been summarised in table 2.2.

Table 2.2 *Summary of deployments of QCL for atmospheric trace analytes measurement*

Atmospheric trace analytes	QCL types	Working wavenumber	Spectroscopic techniques	Citations
N_2O, NO_2 and CH_4	CW-QCL	7.84μm	QCLAS	Tuzson et.al [39](2010)
$^{12}CH_4$ and $^{13}CH_4$	CW-QCL	7.77μm	QCLAS	Santoni, G.W [40]et.al (2012)
$^{12}CH_4$,$^{13}CH_4$ and $^{13}CH_3D$	CW-QCL	8.1 μm	DAS	Kosterev, A.A [41]et.al (1999) .
N_2O and CH_4	DFB-QCL	7.9 μm	DAS	Christopher R. et al[42]
N_2O and CH_4	DFB-QCL	7.8 μm	WMS	K. Namjou et al[43]
N_2O isotopes	DFB-QCL	8.06 μm	WMS	Gagliardu[44]
$^{12}CO_2$,$^{13}CO_2$	QCL	4.3 μm	QCLAS	Weidmann, D et.al [45] (2005)
Water isotopes	CW-DFB-QCL	4.3 μm	QCLAS coupled with white cell	L. Joly et al [46]

2.3.2 Breath Research

The several studies based on exhaled breath and breath odour have been widely utilised to determine the well-being of a subject since the ancient Greeks **[47-48]**. Rollo first reported in 1798 that the odour of

decaying apple was related to those subjects suffering from Diabetes Mellitus [49]. It was also reported that several diseases like kidney diseases, liver complications are related to ammonia smell and rotten egg odour respectively [50].

Table 2.3 *Human exhaled breath trace gases and their concentration range*

Exhaled Breath Compound	Concentration	Physiological Origin
Acetone (C_3H_6O)	ppm	Diabetes
Ammonia (NH_3)	ppb	Liver and renal disease
^{13}Carbon dioxide ($^{13}CO_2$)	ppm	Helicobacter pylori
Carbonyl sulphide (OCS)	ppb	Gut bacteria and liver disease
Ethane (C_2H_6)	ppb	Oxidative stress, cancer
Formaldehyde (CH_2O)	ppm	Breast and Lung cancer
Hydrogen (H_2)	ppm	Gut bacteria
Isoprene (C_5H_8)	ppb	Cholesterol biosynthesis
Methanol (CH_3OH)	ppb	Fruit metabolism
Methane (CH_4)	ppm	Gut bacteria
Nitric Oxide (NO)	ppb	Asthma

However, in 1971, Pauling did the ground breaking discovery about the presence of hundreds of volatile organic compounds (VOCs) in human exhaled breath [51]. The main gas matrix present in the exhaled air contains nitrogen, oxygen, carbon dioxide, argon and water vapour with high concentration. However, other trace gases like nitric oxide, ammonia, hydrogen, nitrous oxide, methane and hydrogen sulphide are also present in the exhaled breath [52].

The main source of the molecules in exhaled air may be either endogenous or exogenous. Endogenous molecules, which are produced in response to the metabolic process in the human body, are transported through the blood stream and subsequently they are exhaled via an alveolar pulmonary membrane. The concentration of exhaled air trace molecules generally varies with patient's diet, state of health and stress level. Therefore, exhaling excessive amount of some compounds might be the cause of some diseases. In this way, exhaled breath analysis has become one of most promising methodologies for clinical diagnostics for early

detection of pathogenic changes at the molecular level. In table 2.3, few bio-markers concerning particular diseases have been mentioned [47, 52]. The recent advancement of QCL-based detection schemes become the most viable alternatives for exhaled breath analysis. The traditional gas analysis systems such as mass spectroscopy (MS), Proton transfer reaction-MS and gas chromatography impede the real-time online exhaled breath analysis due to their size, high cost for handling, complicated maintenance and complex sample pre-treatment process [53]. Alternatively, other gas detection systems with a low cost, such as pellistors, semiconductor and electrochemical sensors do not provide the sensitivity and selectivity in comparison with QCL coupled gas detection tools [54]. The important thing to be required during exhaled breath trace constituents detection by QCL is the selection of analyte-specific absorption line. The targeted absorption line should be chosen in such a way that other interfering matrix compounds, present in exhaled air with higher concentration, do not overlap with the selected absorption line. However, several researchers have employed the detection of isotope species in exhaled breath for clinical diagnostic purposes. For example, many ^{13}C-labelled substrates are often utilized for the clinical diagnostic procedure during pharmacokinetics and other studies regarding the evaluation of specific enzyme activities. Table 2.4 demonstrates the few applications of QCL for breath bio markers detection.

2.3.3 High Resolution Spectroscopy

The emergence of external-cavity continuous wave Quantum Cascade lasers (cw EC-QCL) paved the way for high resolution spectroscopy research [64]. Its access to the MIR region can probe the fundamental and combinational bands of several important molecules with selectively. However, those bands were previously not accessible with diode lasers. Important spectroscopic parameters e.g. line strength, temperature dependant exponent, broadening coefficients can be measured with greater accuracy by QCL based spectroscopic techniques that provide high-precision and high resolution.

Table 2.4 *Summary of deployments of QCL for human exhaled breath analysis*

Exhaled breath trace analytes	QCL types	Working wavenumber	Spectroscopic techniques	Citations
$^{12}CO_2$ and $^{13}CO_2$	DFB-QCL Pulsed	4.35 μm	DAS	T Rubin et.al[55] 2011
CO	DFB-QCL Pulsed	4.59 μm	DAS	Moeskops et [56]al., 2006
NH_3	DFB-QCL	10.3 μm	CRDS	Manne et al., 2006[57]
CO	EC-QCL CW	4.7 μm	Multipass 2f-WMS	Ghorbani et al., 2017[58]
Acetone	DFB-QCL CW	8.2 μm	CEAS	Ciaffoni et al., 2012[59]
NO	DFB-QCL CW	5.2 μm	2f-WMS-OA-ICOS	Bakhirkin et al., 2004[60]
NH_3	DFB-QCL	9.06 μm	2f/1f WMS	Owen et al., 2014[61]
NO	DFB-QCL CW	5.47	ICOS	McCurdy et[62] al., 2006
OCS	EC-QCL CW	5.26 μm	CEAS	Jacek Wojtas[63]

2.4 Reference

[1] A. E. Siegman, Lasers, University Science Books, Mill Valley, California, USA, 1986.

[2] Yao Y, Hoffman AJ, Gmachl CF., *Mid-infrared quantum cascade lasers,* **Nature Photonics**,2012, 6, 432-9.

[3] Razeghi M, Slivken S, Bai Y, Darvish SR.,*The quantum cascade laser: a versatile and powerful tool,* **Optics and Photonics News**, 2008, 19, 42.

[4] A. Schwaighofer, M. Brandstetter and B. Lendl, *Quantum cascade lasers (QCLs) in biomedical spectroscopy*, **Chem. Soc. Rev.,** 2017, 46, 5903.

[5] R. F. Kazarinov and R. A. Suris, *Possibility of amplification of electromagnetic waves in a semiconductor with superlattice*, **Sov. Phys. Semicond.,** 1971, 5, 707–709.

[6] J. Faist, F. Capasso, D. L. Sivco, C. Sirtori, A. L. Hutchinson and A. Y. Cho, *Quantum cascade laser*, **Science**, 1994, 264, 553–556.

[7] Esaki L, Tsu R, *Superlattice and negative differential conductivity in semiconductors,* **IBM Journal of Research and Development,** 1970, 14(1):61–65. DOI: 10.1147/rd.141.0061.

[8] L. Diehl, D. Bour, S. Corzine, J. Zhu, G. Höfler, M. Lončar, M. Troccoli, and F. Capasso, *High-temperature continuous wave operation of strain-balanced quantum cascade lasers grown by metal organic vapor-phase epitaxy*, **Appl. Phys. Lett.**, 2006, 89, 081101.

[9] Y. Bai, S. Slivken, S. R. Darvish, and M. Razeghi, *Room temperature continuous wave operation of quantum cascade lasers with 12:5% wall plug efficiency.* **Appl. Phys. Lett.**, 2008, 93, 021103.

[10] B. Meng and Q. J. Wang, *Broadly tunable single-mode mid-infrared quantum cascade lasers*, **J. Opt.**, 2015, 17, 023001.

[11] Y. Yao, A. J. Hoffman and C. F. Gmachl, *Mid-infrared quantum cascade lasers,* **Nat. Photonics**, 2012, 6, 432–439.

[12] J. Faist, *Quantum cascade lasers*, **Oxford University Press**, Oxford, UK, 1st edn, 2013.

[13] B. Lendl, J. Frank, R. Schindler, A. Muller, M. Beck and J. Faist, *Mid-Infrared Quantum Cascade Lasers for Flow Injection Analysis*, **Anal. Chem.**, 2000, 72, 1645–1648.

[14] J. Kuligowski, G. Quintas and B. Lendl, *High Performance Liquid Chromatography with On-line Dual Quantum Cascade Laser Detection for the Determination of Carbohydrates, Alcohols and Organic Acids in Wine and Grape Juice*, **Appl. Phys. B: Lasers Opt.**, 2010, 99, 833–840.

[15] J.Faist, C. Gmachl, F. Capasso, C. Sirtori, D.L.Sivco, J. N. Billargeon, A.Y.Cho, *Distributed feedback quantum cascade lasers*, **Applied Physics Letters**.1997, 70(20), 2670–2673. DOI: 10.1063/1.119208.

[16] P. Fuchs, J. Friedl, S. Hofling, J. Koeth, A. Forchel and L. Worschech, et al., *Single mode quantum cascade lasers with shallow-etched distributed Bragg reflector*, **Opt. Express**, 2012, 20, 3890–3897.

[17] B. G. Lee, M. A. Belkin, C. Pflugl, L. Diehl, H. F. A. Zhang and R. M. Audet, et al., *DFB quantum cascade laser arrays*, **IEEE J. Quantum Electron.**, 2009, 45, 554–565.

[18] B. G. Lee, H. A. Zhang, C. Pflugl, L. Diehl, M. A. Belkin and M. Fischer, et al., *Broadband Distributed-Feedback Quantum Cascade Laser Array Operating From 8.0 to 9.8 μm*, **IEEE Photonics Technol. Lett.**, 2009, 21, 914–916.

[19] R. Lewicki, M. Witinski, B. Li and G. Wysocki, *Spectroscopic benzene detection using a broadband monolithic DFB-QCL array*, **SPIE, San Francisco,** USA, 2016.

[20] P. Rauter and F. Capasso, *Multi-wavelength quantum cascade laser arrays*, **Laser Photonics Rev.**, 2015, 9, 452–477.

[21] J.P.Waclawek, R. Lewicki, H.Moser,M. Brandstetter, F.K.Tittel and B. Lendl, *Quartz-enhanced photoacoustic spectroscopy-based sensor system for sulfur dioxide detection using a CW DFB-QCL*, **Appl. Phys. B: Lasers Opt.**, 2014, 117, 113–120.

[22] C. Reidl-Leuthner, A. Viernstein, K. Wieland, W. Tomischko, L. Sass and G. Kinger, et al., *Quasi-simultaneous in-line flue gas monitoring of NO and NO_2 emissions at a caloric power plant employing mid-IR laser spectroscopy*, **Anal. Chem.**, 2014, 86, 9058–9064.

[23] G. Duxbury, N. Langford, M. T. McCulloch and S. Wright, *Quantum cascade semiconductor infrared and far-infrared lasers: from trace gas sensing to non-linear optics*, **Chem. Soc. Rev.**, 2005, 34, 921–934.

[24] A. Hugi, R. Terazzi, Y. Bonetti, A. Wittmann, M. Fischer, M. Beck, J. Faist and E. Gini, *External cavity quantum cascade laser tunable from 7.6 to 11.4µm.* **Applied Physics Letters**, 95, 061103 (2009), http://dx.doi.org/10.1063/1.3193539

[25] G. Wysocki, R. Lewicki, R. Curl, F. Tittel, L. Diehl, F. Capasso, M. Troccoli, G. Hoer, D. Bour, S. Corzine, R. Maulini, M. Giovannini and J. Faist. *Widely tunable mode-hop free external cavity quantum cascade lasers for high resolution spectroscopy and chemical sensing*. **Applied Physics B**, 2008, 92, 305-311, http://dx.doi.org/10.1007/s00340-008-3047-x

[26] G. P. Luo, C. Peng, H. Q. Le, S. S. Pei, W. Y. Hwang, B. Ishaug, J. Um, J. N. Baillargeon, and C. H. Lin, *Grating-tuned external-cavity quantum-cascade semiconductor lasers*, **Applied Physics Letters**, 2001, 78, 19, pp. 2834-2836.

[27] G. Totsching, F. Winter, V. Pustogov, J. Faist and A. Muller, *Mid-infrared externalcavity quantum cascade laser*, **Optics letters**, 27, 1788-90, 2002.

[28] G. Wysocki, R. F. Curl, F. K. Tittel, R. Maulini, J. M. Bulliard and J. Faist, *Widely tunable mode-hop free external cavity quantum cascade laser for high resolution spectroscopic applications*, **Appl. Phys. B: Lasers Opt.**, 2005, 81, 769–777.

[29] S. D. Saliba, M. Junker, L. D. Turner and R. E. Scholten, *Mode stability of external cavity diode lasers*, **Appl. Opt.**, 2009, 48, 6692–6700.

[30] M. Yamada, *Theory of mode competition noise in semiconductor injection lasers*, **IEEE J. Quantum Electron.**, 1986, 22, 1052–1059.

[31] F. Fuchs, B. Kirn, C. Mann, Q. Yang, W. Bronner and B. Raynor, et al., *Spectral tuning and mode competition of quantum cascade lasers studied by time-resolved Fourier transform spectroscopy*, **SPIE, Boston, USA**, 2006.

[32] R. F. Curl, F. Capasso, C. Gmachl, A. A. Kosterev, J. B. McManus, R. Lewicki, M. Pusharsky, G. Wysocki, and F. K. Tittel, *Quantum cascade lasers in chemical physics*, **Chem. Phys. Lett.** , 2010, 487, 1–18.

[33] F. K. Tittel, Y. Bakhirkin, A. A. Kosterev, and G. Wysocki, *Recent advances in trace gas detection using quantum and interband cascade lasers*, **Rev. Laser Eng.,** 2006**,** 34, 275–282.

[34] F. K. Tittel, D. Richter, and A. Fried, *Mid-infrared laser applications in spectroscopy*, **Applied Physics** Vol. 89, I. T. Sorokina and K. L. Vodopyanov, Eds., pp. 445–516, Springer-Verlag, Berlin, (2003).

[35] Concentrations and Distributions of Atmospheric Trace Gases, D. H. Ehhalt, **Ber. Buriseiiyrs. Pkys. Cheiii. 96** lYY2 **No.** 3

[36] R.P. Wayen, *Chemistry of Atmospheres*, **Oxford University Press**, third edition, 2000.

[37] R.Goody, *Principles of Atmospheric Chemistry and Physics*, **Oxford University Press,** 1995.

[38] M.Z.Jacobson, *Atmospheric Pollution*, **Cambridge University Press**, 2002.

[39] B.Tuzson, R.V.Hiller, K. Zeyer, W.Eugster, A.Neftel, C.Ammann, and L. Emmenegger, *Field intercomparison of two optical analyzers for CH_4 eddy covariance flux measurements*. **Atmos. Meas. Tech.**, 2010, 3, 1519–1531.

[40] G. W. Santoni, , B. H. Lee, , J. P. Goodrich, , Varner, R. K. Crill, P. M., J. B. McManus, D. D. Nelson, M. S. Zahniser, and S.C. Wofsy, *Mass fluxes and isofluxes of methane (CH_4) at a New Hampshire fen measured by a continuous wave quantum cascade laser spectrometer*. **J. Geophys. Res.**, 2012,117, D10301.

[41] A. A. Kosterev, , R.F. Curl, , F.K.Tittel, , C.Gmachl, , F.Capasso, D.L.Sivco, J. N. Baillargeon, , A. L. Hutchinson, and A. Y. Cho, *Methane concentration and isotopic composition measurements with a mid-infrared quantum-cascade laser*. **Optic. Lett.**, 1999, 24: 1762–1764.

[42] C. R. Webster, G. J. Flesch, D. C. Scott, J. E. Swanson, R. D. May, W. S. Woodward, Cl. Gmachl, F. Capasso, D.L. Sivco, J. N. Baillargeon, A. L. Hutchinson, and A. Y. Cho, *Quantum-cascade laser measurements of stratospheric methane and nitrous oxide*, **Appl. Opt.** 2001, 40, 321-326.

[43] K. Namjou, S. Cai, E. A. Whittaker, J. Faist, C. Gmachl, F. Capasso, D. L. Sivco, and A. Y. Cho, *Sensitive absorption spectroscopy with a room-temperature distributed-feedback quantum-cascade laser*, **Opt. Lett.** 1998, 23, 219-221.

[44] G. Gagliardi, S.Borri, F. Tamassia, , F. Capasso, , C. Gmachl, , D.L.Sivco, , J.N. Baillargeon, A.L.Hutchinson, , and A.Y. Cho, *A frequency-modulated quantum cascade laser for spectroscopy of CH4 and N2O isotopomers*. **Isot. Environ. Health Stud.,** 2005, 41, 313–321.

[45] Weidmann, D., Wysocki, G., Oppenheimer, C., and Tittel, F.K. *Development of a compact quantum cascade laser spectrometer for field measurements of CO_2 isotopes*. **Appl. Phys. B**, 2005, 80, 255–260.

[46] L. Joly, V. Zéninari, B. Parvitte, D. Courtois, and G. Durry, *Water-vapor isotope ratio measurements in air with a quantum-cascade laser spectrometer*, **Opt. Lett.**, 2006, 31, 143-145.

[47] T. H. Risby and F. K. Tittel. *Current status of midinfrared quantum and interband cascade lasers for clinical breath analysis*. **Optical Engineering**, 2010. 49, 111123 http://dx.doi.org/10.1117/1.3498768

[48] W. Miekisch, J. K. Schubert and G. F. E. Noeldge-Schomburg. *Diagnostic potential of breath analysis focus on volatile organic compounds*. **Clinica Chimica Acta; International Journal of Clinical Chemistry**, 2004, 347, 25-39.

[49] J. Rollo. Cases of the Diabetes Mellitus. . . ". Printed by T. Gillet for C. Dilly, in the Poultry, Second Edition, London (1798).

[50] A. Manolis. *The diagnostic potential of breath analysis*. **Clinical Chemistry**, 1983, 29, 5-15.

[51] L. Pauling and A. Robinson. *Quantitative analysis of urine vapor and breath by gas-liquid partition chromatography*. **Proceedings of the National Academy of Sciences of the United States of America**, 1971, 68, 2374-2376.

[52] C. Wang and P. Sahay. *Breath Analysis Using Laser Spectroscopic Techniques: Breath Biomarkers, Spectral Fingerprints, and Detection Limits*, **Sensors**, 2009, 9, 8230- 8262.

[53] Z. Bielecki, T. Stacewicz, J. Wojtas and J. Mikolajczyk, *Application of quantum cascade lasers to trace gas detection*, **Bull. Pol. Acad. Sci.: Tech. Sci.**, 2015, 63, 515–525.

[54] J. Mikolajczyk, Z. Bielecki, T. Stacewicz, J. Smulko, J. Wojtas and D. Szabra, et al., *Detection of gaseous compounds with different techniques*, **Metrol. Meas. Syst.**, 2016, 23, 205–224.

[55] T. Rubin, T. von Haimberger, A. Helmke and K. Heyne, *Quantitative determination of metabolization dynamics by a real-time $^{13}CO_2$ breath test*, **J. Breath Res.**, 2011, 5, 027102.

[56] B. W. M. Moeskops, H. Naus, S. M. Cristescu and F. J. M. Harren, *Quantum cascade laser-based carbon monoxide detection on a second time scale from human breath*, **Appl. Phys. B: Lasers Opt.**, 2006, 82, 649–654.

[57] J. Manne, O. Sukhorukov, W. Jager and J. Tulip, *Pulsed quantum cascade laser-based cavity ring-down spectroscopy for ammonia detection in breath*, **Appl. Opt.**, 2006, 45, 9230–9237.

[58] R. Ghorbani and F. M. Schmidt, *Real-time breath gas analysis of CO and CO_2 using an EC-QCL*, **Appl. Phys. B: Lasers Opt.**, 2017, 123, 144.

[59] L. Ciaffoni, G. Hancock, J. J. Harrison, J. P. van Helden, C. E. Langley and R. Peverall, et al., *Demonstration of a mid-infrared cavity enhanced absorption spectrometer for breath acetone detection*, **Anal. Chem.**, 2013, 85, 846–850.

[60] Y. A. Bakhirkin, A. A. Kosterev, C. Roller, R. F. Curl and F. K. Tittel, *Mid-infrared quantum cascade laser based off-axis integrated cavity output spectroscopy for biogenic nitric oxide detection*, **Appl. Opt.,** 2004, 43, 2257–2266.

[61] K. Owen and A. Farooq, *A calibration-free ammonia breath sensor using a quantum cascade laser with WMS 2f/1f*, **Appl. Phys. B: Lasers Opt.,** 2014, 116, 371–383.

[62] M. R. McCurdy, Y. A. Bakhirkin and F. K. Tittel, *Quantum cascade laser-based integrated cavity output spectroscopy of exhaled nitric oxide*, **Appl. Phys. B: Lasers Opt.**, 2006, 85, 445–452.

[63] Wojtas, J. *Application of Cavity Enhanced Absorption Spectroscopy to the Detection of Nitric Oxide, Carbonyl Sulphide, and Ethane — Breath Biomarkers of Serious Diseases*. **Sensors** 2015, *15*, 14356-14369.

[64] Simone Borri, Saverio Bartalini, Pablo Cancio, Iacopo Galli, Giovanni Giusfredi, Davide Mazzotti, andPaolo de Natale , *Quantum cascade lasers for high-resolution spectroscopy,* **Optical Engineering,** 2010, 49(11), 111-122. https://doi.org/10.1117/1.3498775.

Chapter 3

Infrared absorption spectroscopic techniques for trace gas sensing

3.1 Introduction

Infrared molecular absorption spectroscopy is an important tool for detection and monitoring of trace molecular species in the gas phase with high sensitivity and molecular selectivity. Nevertheless, molecular absorption spectroscopy refers to the field of interaction (i.e. absorption, emission, scattering) of electromagnetic (EM) radiation with molecules or atom. In quantum mechanical point of view, absorption is defined as a process, where atoms or molecules change their quantum states from lower energy level to a higher energy level by absorbing an incoming photon. The energy difference between the two energy levels associated with the transition is equal to the absorbed photon energy, which can be demonstrated by Planck's law:

$$\Delta E = E_{upper} - E_{lower} = h\nu \tag{3.1}$$

where ν is the corresponding Eigen frequency. In atomic spectroscopy, all the quantum transitions reflect in the variations of electrons configuration. However, in molecular spectroscopy, transitions of a molecule occur between energy states due to their internal motions including the nuclei vibrations, rotations and the orientation of nuclear spin. In consequence, molecular spectra becomes more complex in comparison to atomic spectra and also provides the information on the molecular structure, the strength, length of the bond, relative positions of

its constituent atom, transition dipole moment and the energies by employing quantum mechanical models of the distribution of discrete energy levels in a molecule. According to Born-Oppenheimer approximation, the quantized energy in a molecule can be assumed of being stowed in three distinct modes rotational, vibrational and electronic modes.

Table 3.1 *Nature of molecular transitions at different electromagnetic radiations*

Transition:	Spectral region	Limits:ν/cm^{-1}	Limits: λ/µm
Pure Rotational	Microwave	~0.3-300	~30000-30
Pure Vibrational/(Rotational+Vibrational)	Infrared	~300-13000	~30-0.8
Pure Electronic/(Electronic+Rotational+Vibrational)	Visible and UV	~13000-50000	~0.8-0.2

Therefore the energy can be expressed as the sum of electronic energy E_{el}, vibrational energy E_{vib} and rotational energy E_{rot} energy.

$$E = E_{el} + E_{vib} + E_{rot} \qquad \textbf{(3.2)}$$

However, in this approximation, the energy difference during the molecular transition due to excitation of electrons $\Delta E_{el} = h\nu_{el}$ is much larger than the energy difference due to molecular vibration $\Delta E_{vib} = h\nu_{vib}$ which is again larger than energy of molecular rotations $\Delta E_{rot} = h\nu_{rot}$, i.e $h\nu_{el} \gg h\nu_{vib} \gg h\nu_{rot}$. Table 3.1 depicts the different type of transitions at different wavelength region. The work presented in this thesis is focused on the development of mid infrared QCL-based spectroscopic techniques and their applications in quantitative trace gas monitoring for environmental science, breath research and in absolute spectroscopic parameters calculation. Therefore our aim of this chapter is to introduce fundamental principles of molecular spectroscopy to get a better

understanding of infrared spectroscopy (IR). We will also discuss the common spectroscopic detection methods for monitoring trace atmospheric constituents and trace species in human exhaled air.

3.2 Fundamental concept of infrared absorption spectroscopy

Infrared absorption frequencies are often utilised as a key to unlock the structure–spectral relationships of the associated molecular vibrations. The fundamental aspect for occurring absorption of infrared radiation by the molecule or the functional group under study is the net change in dipole moment. Most commonly, the vibrational absorption spectra comprise of numerous discrete closely spaced component (≤ 10 cm^{-1}), arising due to rotational transitions associated with each vibrational excitation. In the subsection, a brief overview of vibrational, rotational and ro-vibrational (combination of rotation and vibration) spectroscopy are discussed.

3.2.1 Vibrational Spectroscopy

A molecular vibration is defined as bond stretching or bending of the constituent atoms of a molecule due to their displacement relative to one another when exposed to EM radiation. This phenomenon leads to change in dipole moment and causes the transitions between the quantized vibrational energy levels. Therefore this type of vibration is considered as IR-active. It is noteworthy to mention that IR-active transition occurs only when "changes in the dipole moment" either along the line of the symmetry axis (parallel to it) or at the right angle to the line (perpendicular) condition is fulfilled rather molecules having their permanent dipole moment. Thus heteronuclear diatomic molecule (such as NaBr, HCL or OH) shows the differences in atomic polarizabilities leading to some non-zero permanent dipole moment of which magnitude will oscillate during bond stretching. However, homonuclear diatomic molecules such as H_2, N_2 is considered as "infrared" inactive as there is no possibility present in changing the dipole moment. For polyatomic molecules, the situations become more intricate as the motion of each atom can be resolved into components alongwith the three directions of a Cartesian coordinate system. Therefore, any molecule composed of n

atoms possesses 3N degrees of freedom of motion including vibrations, translations, and rotations. For a polyatomic linear molecule containing N atoms, the degrees of freedom can be expressed as 3N-5 (or 3N-6 for non-linear molecule), which is used to describe vibrational modes of the molecule. For example, acetylene (C_2H_2), having 4 atoms, comprises of degrees of freedom 3N-5 = 7 (being a linear molecule), which means it has 7 normal modes of vibration as depicted in figure 3.1 [1]. Each vibrational mode quantum number is specified in normal mode notation; v_1 and v_2 represent the symmetric C-H stretch and the symmetric C-C stretch respectively; whereas v_3 is described as antisymmetric C-H stretch. But v_4 (symmetric-trans) and v_5 (antisymmetric-cis) represent the doubly degenerate bending modes leading to 7 vibrational degrees of freedom in total from 5 vibrational modes. However, only v_3 and v_5 modes produce an oscillating change in zero dipole moment of the molecule leading to IR absorption.

Band Origin (cm^{-1})	Normal Mode	Description	IR Active
3373 (v_1)	H—C≡C—H	Symmetric CH stretching	NO
1973 (v_2)	H—C≡C—H	Symmetric CC stretching	NO
3281 (v_3)	H—C≡C—H	Anti-symmetric CH stretching	Yes
612.9 (v_4)	H—C≡C—H	'Symmetric' bending	NO
730.3 (v_5)	H—C≡C—H	'Anti-symmetric' bending	Yes
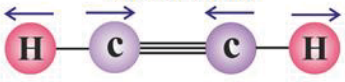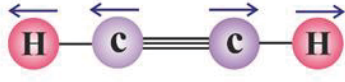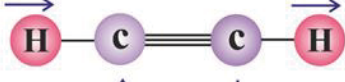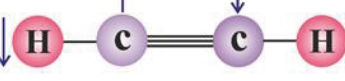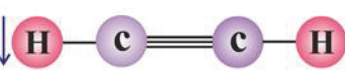
Figure 3.1 *Fundamental vibrational modes of acetylene.*

Each individual vibrational mode of molecules can be thought as a combination of atomic displacement and this vibrational motion can be assumed to act an independent simple harmonic oscillator (SHO). Therefore Schrödinger equation can be employed to evaluate the permitted energy levels, E_{vib} for each vibrational state of the molecule. So the Hamiltonian for a particular vibrational state can be written as,

$$\hat{H}_{vib}\Psi(r) = -\frac{\hbar^2}{2\mu}\frac{d^2\Psi(r)}{dr} + V(r)\Psi(r) = E_{vib}\Psi(r) \qquad (3.3)$$

Where $\Psi(r)$ is the analogous wave function corresponding to a particular vibrational state and E_{vib} is denoted here as the energy eigen value of that particular vibrational state. The potential energy function $V(r)$ is expressed here as a function of $(r - r_e)$ i.e separation between inter-nuclear and equilibrium separation of bond.

$$V(r) = \frac{1}{2}k(r - r_e)^2 \tag{3.4}$$

The energy eigen value can be calculated by solving Schrödinger equation and it is expressed as

$$E_{vib} = \left(v + \frac{1}{2}\right)h\nu_0 \tag{3.5}$$

Where v is vibrational quantum number which has the allowed values of $v=0, 1, 2, 3,....$ and ν_0 is the oscillation frequency (in Hz) of the molecule given by:

$$\nu = \frac{1}{2\pi}\sqrt{\frac{k}{\mu}} \tag{3.6}$$

where μ and k are the reduced mass of the molecule and bond force constant respectively. The reduced mass is expressed as

$$\mu = \frac{m_1 m_2}{m_1 + m_2} \tag{3.7}$$

However, in spectroscopy study, the vibrational energies typically are expressed in cm^{-1}, which can be represented as 'G' :

$$G(v) = \frac{E_{vib}}{hc} = (v + \frac{1}{2})\bar{\nu}_0 \ (\text{cm}^{-1}) \tag{3.8}$$

$$\text{with } \bar{\nu}_0 = \frac{1}{2\pi c}\sqrt{\frac{k}{\mu}} \ (\text{cm}^{-1})$$

Typically the vibrational selection rule for a simple harmonic oscillator is $v = \pm 1$ ($1\leftarrow 0$). However, in presence of anharmonicity, the selection rule becomes $\Delta v = \pm 2, \pm 3....$ leading to weak overtone transitions($2\leftarrow 0, 3\leftarrow 0 \ etc.$). The anharmonicity is originated because the motion of vibrating bonds is not purely harmonic. Therefore the restoring force is no longer proportional to the displacement of bond. The

anharmonic effect can be represented by the Morse potential function (see the figure 3.2)

$$V(r) = D_e[1 - e^{-a(r-r_e)}]^2 \qquad (3.9)$$

where D_e is the dissociation energy and a is a constant for a particular molecule.
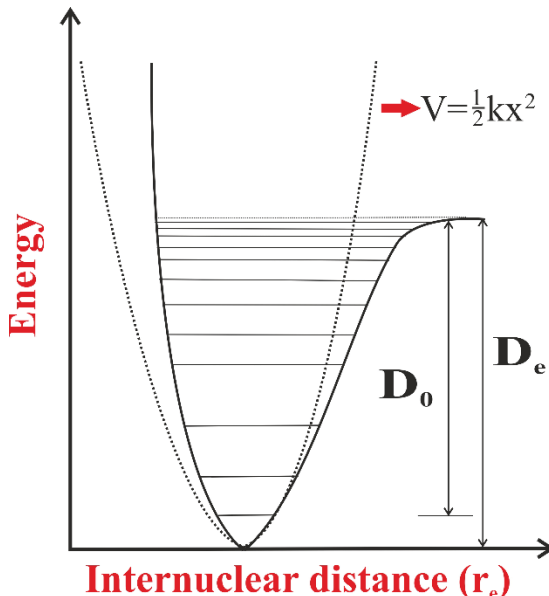
Figure 3.2 *Pictorial representation of Morse potential curve. Where $D_e=D_0+ZPE$; ZPE is the zero point energy.*

The permitted vibrational energy levels for Morse potential in presence of the anharmonicity are described in terms of wavenumber by the following equation:

$$G(v) = \left(v + \frac{1}{2}\right)\bar{v}_0 - \left(v + \frac{1}{2}\right)^2 x_e \bar{v}_0 \; ; \quad x_e = \frac{\bar{v}_0}{4D_e} \qquad (3.10)$$

When the constraint to the simple harmonic oscillator is unperturbed, the selection rule allows combination bands and overtone transitions. This combination band arises due to simultaneous excitation of two or more fundamental or overtones such v_4+v_5, $2v_1+v_2$ etc. This combination band frequencies can be assessed by summing the mode frequencies but anharmonic coupling diminishes the frequencies marginally [2].

3.2.2 Rotational Spectroscopy

Each vibrational energy level comprises more closely spaced rotational lines with a large number. The interaction of the dipole moment of the rotating molecule with the oscillating electric field of incident IR

light causes the stack of rotational lines. The key principle for the rotational transition is that molecule must have permanent electric dipole moment which will alter periodically when the molecule rotates around the centre of gravity of the molecule. The rotational spectroscopy affords the substantial information about the bond angle and bond length in a molecule, which can be retrieved by using pure rotational transitions stemming in the EM spectrum of the microwave region. For linear polyatomic molecule and the spherical rotors, the energy of the rotational energy levels without centrifugal distortion is given by

$$E_J = BJ(J + 1) \text{ , where } B = \frac{\hbar}{8\pi^2 IC} \qquad \textbf{(3.11)}$$

In equation 3.11 J(=0,1,2,3….) is the angular momentum quantum number, B is the rotational constant, which depends on the moment of inertia (I) with respect to a particular axis. The selection rule linked rotational transition is given by $\Delta J = \pm 1$, where $\Delta J = +1$ corresponds to the absorption of a photon and $\Delta J = -1$ corresponds to emission of a photon. Furthermore, the rotational lines are equispaced with respect to adjacent rotational level with 2BJ.

However, in a real scenario when the molecule starts to rotate in the exposure of EM radiation, the distance between atoms of the molecule is increased due to centrifugal force. Thereby the moment of inertia is increased, which in turn decreases the spacing between two adjacent rotational energy levels progressively as J increases. Therefore, the rotational energy in the presence of distortion is expressed with centrifugal energy term $D_j J(J + 1)^2$ (in equation 3.12), where D_j is the centrifugal distortion constant. However, the magnitude of D_j , depends on the strength of the bond inversely, is very less in comparison to the rotational constant B, which suggests that the distortion of the weak bond is quatitively large than the strong bond.

$$E_J = BJ(J + 1) - D_j J(J + 1)^2; \ D_j = \frac{4B^3}{\bar{v}^2} \qquad \textbf{(3.12)}$$

3.2.3 Ro-vibrational Spectroscopy

In ro-vibrational spectroscopy, the fine structure of the vibrational band has been analyzed. The fine structures of vibrational band arise due to rotational transitions associated with a vibrational excitation. In the real world, a molecule can vibrate many times during one period of rotation, because the vibrational frequency is higher than the rotational frequency (about one to two orders). According to the Born-Oppenheimar approximation, ro-vibration energy can be written as the sum of the individual energies of vibrational and rotational motion. Thereby it can be written as follows, ignoring centrifugal distortion and anharmonicity:

$$E_{total} = E_{rot} + E_{vib} \tag{3.13.1}$$

$$E_{total} = \left(v + \frac{1}{2}\right)\bar{\upsilon}_0 + BJ(J+1) \tag{3.13.2}$$

The selection rules for ro-vibrational transition are the same for individual component separately, i.e $\Delta J = \pm 1$ and $v = \pm 1$. Using the Born-oppenheimer approximation, the energy gap between a rotational level in the first vibrational state (v=1,J) and a rotational level in the ground vibrational state (v=0,J") can be described by the following equations:

$$\Delta E = E_{v=1,J}{}' - E_{v=0,J}{}'' \tag{3.14}$$

$$\Delta E = \bar{\upsilon}_0 + 2hB(J'' + 1), \text{ for } \Delta J = +1, \quad J' = J' + 1$$

$$\Delta E = \bar{\upsilon}_0 - 2hB(J'' + 1), \text{ for } \Delta J = -1, J'' = J' + 1$$

To express the ro-vibration spectra, above two equations are combined written as follows:

$$\Delta E = \bar{\upsilon}_0 + 2Bm \qquad \text{m=} \pm 1, \pm 2, \pm 3, \ldots \ldots$$

In the combined ro-vibrational spectrum, the lines to the high frequency side of $\bar{\upsilon}_0$ are denoted as R-branch ($\Delta J = +1$), whereas the lines to the low frequency side of $\bar{\upsilon}_0$ are signified as P-branch ($\Delta J = -1$). However, rovibrational transition with $\Delta J = 0$ are also allowed and this condition is met when angular momentum becomes perpendicular to the major axis

of rotational symmetry. Thereby, this condition gives rise to a Q-branch with energy gap $\Delta E = \bar{v}_0$.

However, the rotational constant B is no longer considered to be the constant different vibrational levels, if we incorporate the effect of anharmonicity. Therefore Born-Oppenheimer approximation regarding energy separation collapses. Hence, the rotational constant can be expressed as

$$B_v = B_e - \alpha\left(v + \frac{1}{2}\right) \qquad (3.15)$$

where B_e is the rotational constant for equilibrium bond length and α denotes the vibrational-rotation coupling constant, which has a positive value for most of the molecule. For this scenario described above, the energy of the transition can be described by:

$$\Delta E = \bar{v}_0 + (B_1 + B_0)m + (B_1 - B_0)m^2 \qquad (3.16)$$

where B_1 and B_0 indicate the upper and the lower rotational constant, respectively. The key point is that in absence of anharmonicity effect, the resultant spectra due to ro-vibrational transition would be symmetrical about the origin and the frequency spacing between two rotational lines of a particular vibrational transition is 2B.
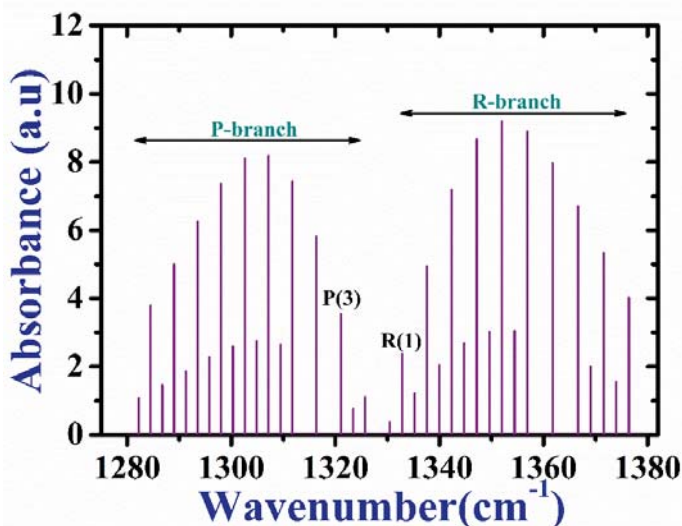
Figure 3.3 *Ro-vibrational spectrum of combinational $v_4 + v_5$ band of C_2H_2 in the region of 1280-1380 cm^{-1}. The spectrum data has been taken from HITRAN database* [3].

However, in the presence of anharmonicity, the asymmetrical spectra have been formed. The R-branch lines become closer with increasing m, whereas P-branch lines become more widely spaced with increasing m (negative).

The ro-vibrational spectrum of $(\nu_4+\nu_5)$ band of C_2H_2 has been depicted in figure 3.3 as a representative example of ro-vibrational spectra. This $(\nu_4+\nu_5)$ band belongs to the wavenumber region 1280-1380 cm^{-1}. The spectrum contains only P-branch and R-branch because the dipole moment $\perp$ to the major axis of rotational symmetry remained same leading to forbid the selection rule $\Delta J = 0$. Thus the spectra does not show any Q branch transition. The reason behind the concern of this particular band of C_2H_2 is that one of the research work presented in this thesis is based on spectroscopic studies of $\nu_4+\nu_5$ band of C_2H_2. This band is chosen for three reasons: (i) this spectral region has a great astrophysical interest [4].; (ii) it has sufficiently strong absorption cross section with interference free from other important trace molecules, as this region belongs to the mid-infrared region [5-6].; (iii) l-type resonance phenomena occur in this spectral region, which is very attractive for spectroscopy studies [7].

3.3 Line shape function

A spectral line emitted by the atom or molecule is not precisely sharp, which means the discrete absorption spectra are never strictly monochromatic. The knowledge about the energy levels and the neighbouring environment of the concerned molecule can be retrieved by measuring the spectral line width. However, the spectral line mainly arises due to the finite life time of molecule in an excited state before decaying to ground state. The line profile is described as a spectral distribution I(ν) of the absorbed intensity in the vicinity of the central frequency and the linewidth of the spectral line is described as the frequency interval $\delta\nu = |\nu_1 - \nu_2|$ between two frequency ν_1 and ν_2 for which the spectral intensity has its half value.
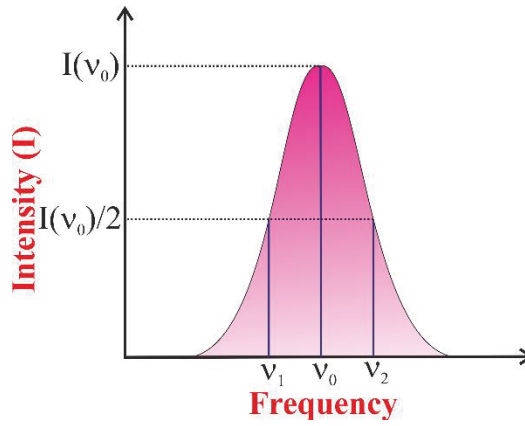
Figure 3.4 *Ro-vibrational spectrum of combinational $v_4 + v_5$ band of C_2H_2 in the region of 1280-1380 cm^{-1}. The spectrum data has been taken from HITRAN database.*

Usually, Lorentzian profile is utilzed to describe the natural line-profile, but other broadening effects like Doppler broadening and collisional broadening actually dominate the broadening mechanisms. However, these two broadening mechanisms is essential for gas-phase measurements.

The Doppler broadening is considered to be main broadenings of spectral lines, which causes due to the apparent frequency shifts of each emitter or absorber arising from the thermal movement of atoms or molecule. The multiple molecules possess different velocities, which causes many different small shifts leading to make a summation of absorption/emission signals in a broad line. The Doppler shifts can be expressed for a Gaussian profile with a FWHM (see equation 3.17) [8]:

$$\delta v = \frac{2v}{c} \left(\frac{2kT}{m} \ln 2\right)^{\frac{1}{2}} \qquad\qquad \textbf{(3.17)}$$

where v is the transition frequency, m is the mass of the molecule, T is the temperature, k is the Boltzmann constant and c is the speed of the light. This width is calculated using Maxwell-Boltzmann distribution of velocity and from the equation 3.17 it can be found that width is proportional to temperature because in higher temperature molecules have a wide distribution of velocity causing broadened spectral line.

However, in absence of Doppler broadening, the spectral line would have a still finite width due to lifetime broadening. This broadening is occurred

due to quantum mechanical phenomena, named as "uncertainty broadening", which is related to the Heisenberg uncertainty principle. This principle states that if a molecule exists in a particular state for a limited lifetime τ, then the energy of the state will be uncertain to an amount of δE:

$$\delta E \approx \frac{\hbar}{\tau} \tag{3.18}$$

$$\text{or } \delta \bar{\upsilon} = \frac{1}{2\pi c \tau}$$

However, the broadening will always occur to some level as no excited state has no infinite lifetime.

For the gas sample, the surrounding environment can also impact on the lifetime of a state. When gas molecules randomly collide with each other, the energy levels are perturbed due to their mutual interaction. Generally, at high pressure (50 Torr~100 Torr), the collisional deactivation shortens the lifetime of the excited state causing to the broadening of spectral lines. Therefore, this collisional-induced line broadening is called the pressure broadening. The collisional line width (δE_{col}) can be written in terms of collisional lifetime τ_{col}:

$$\delta E_{col} \approx \frac{\hbar}{\tau_{col}} \tag{3.19}$$

where $\tau_{col} = \frac{1}{z}$ and z is collisional frequency, which is proportional to surrounding pressure p according to the kinetic theory of gases. Therefore, we can write

$$\delta E_{col} \propto p \tag{3.20}$$

Generally, pressure broadening effect gives rise to the line shapes with Lorentzian profiles. The pressure broadening coefficients are utilized eventually to determine the degree to which spectral features are broadened. The coefficients are usually obtained from the linear relationship between the width of broadened spectra and pressure of the bath gas. However, it is important to mention that the spectral line should

be fitted with a Voigt profile when Doppler and pressure broadening both influence the particular experiment.

3.4 Line strength

The sensitivity of the trace gas sensing by laser optics–based spectroscopic tool is obtained principally by measuring the strength of the absorption. Typically Beer-Lambert law equation (see equation 3.21) provides the information regarding the several depending factors of the strength of absorption, which is given by

$$I = I_0 \exp(-\sigma_\lambda NL) \qquad (3.21)$$

$$\text{Or } \alpha(v) = -\ln\left(\frac{I}{I_0}\right) = \phi_v L$$

where σ_λ is the line integrated absorption cross-section, I_0 and I are incident and transmitted light intensities respectively, N is the sample concentration, L is the sample length, $\alpha(v)$ is the spectral absorbance and ϕ_v is the spectral absorption coefficient. However, this spectral absorbance can be determined from the integrated line strength $S(T)$ (cm/mol) of the transition at a temperature T, which is given by

$$\alpha(v) = S(T).g(T,P).N.L \qquad (3.22)$$

where $g(T,P)$ is the line shape function.

The line strength $S(T)$ can be expressed as a line strength $S(T_0)$ at some reference temperature T_0 and lower state energy E (cm^{-1}), which given by;

$$S(T) = S(T_0)\frac{Z(T_0)}{Z(T)}\left(\frac{T_0}{T}\right)\exp\left(-\frac{hcE}{k_B}\left(\frac{1}{T}-\frac{1}{T_0}\right)\right)[1-\exp\left(-\frac{hcv_0}{k_BT}\right)]/[1-\exp\left(-\frac{hcv_0}{k_BT_0}\right)] \quad (3.23)$$

where h is Planck's constant equal to $6.6260755 \times 10^{-27}$ erg s (1 erg $=10^{-7}$ J); c is vacuum speed of light equal to $2.99792458 \times 10^{10}$ cm s^{-1}; Z (T) is the partition function at temperature T of the absorbing molecule; k is Boltzmann's constant equal to 1.380658×10^{16} erg K^{-1} and v_0 is the line centre frequency of the spectral transition.

It is clear from the equation 3.22 is that absorbance depends on firstly concentration of absorbing species and secondly path length of the molecular interaction with light. However, the other two factors like

population level from which transitions occur and transition probability also governs spectral line intensity. The relative population of two different energy states (lower energy level and upper energy level) can be expressed using Boltzmann distribution.

$$\frac{N_{upper}}{N_{lower}} = \frac{g_u}{g_l}\exp(-\frac{\Delta E}{kT}) \tag{3.24}$$

In 3.24, ΔE $(\Delta E = E_{uper} - E_{lower})$ is the energy gap between upper and lower state, T is the temperature and k is the Boltzmann constant. g_u and g_l are the degeneracies of the upper and lower state respectively. However, molecules, possess the transition from lower state to upper state, should have transition dipole moment μ and the intensity of the transition is proportional to the square of the dipole moment, which can be expressed as;

$$\int \sigma_v dv = \frac{4\pi^2 v}{2\varepsilon_0 hc}|\mu|^2 \tag{3.25}$$

In (equation 3.25), ε_0 denotes the permittivity of the system.

3.5 Spectroscopic techniques for trace gas analysis

In recent years, laser –based trace gas sensing has gathered enormous attention from an extensive variety of areas including chemical analysis in industrial process control [9-10], ecological and pollution monitoring[11-12], exhaled breath monitoring for medical diagnostics[13-14], industrial and urban emission measurement [15-16] and homeland security [17]. The conventional spectroscopic technique for quantitative trace gas monitoring by analysing characteristic spectra of molecules is known as tunable diode laser absorption spectroscopy (TDLAS). The salient features of laser gas analyser like fast response time, long life cycle, high sensitivity and selectivity make the tool suitable for insitu, real time detection.

Direct absorption spectroscopy (DAS) is one of the simplest examples of the gas detection optical tool due to its simple optical configuration and signal processing. However, it suffers from low sensitivity (absorbance~10^{-3}) due to laser intensity fluctuations and interference of

1/f noise in the detection system. Therefore, the noise reduction in the signal and enhancement of the absorption are the two best ways to increase the sensitivity of the instrument. The modulation techniques e.g., wavelength modulation spectroscopy (WMS) and frequency modulation spectroscopy (FMS) are generally incorporated to remove 1/f noise in detection of the signal to gain the typical sensitivity of absorbance ~ 10^{-5}. However, to increase the absorption, maximum interaction of light with molecules is required, which is possible if we incorporate the multiple-pass or long-path absorption cell and cavity enhanced absorption spectroscopy (CEAS) spectroscopy technique. Nevertheless, reducing noise and enhancement of interaction of light with target molecule both can be possible in cavity enhanced wavelength modulation spectrometry (CE-WMS) and noise-immune cavity-enhanced optical heterodyne molecular spectroscopy (NICE-OHMS). A brief overview of the aforementioned gas detection techniques is elaborated in this section.

3.5.1 Modulation spectroscopy: WMS and FMS

Modulation spectroscopy becomes more popular as a trace gas detection tool due to its achievement of a quite high signal to noise ratio (SNR) [18-19]. The detection sensitivity for modulation technique can be achieved without the variation of sample path length. However, incorporating a multipass cell can improve the detection limit further. In this technique, the laser frequency is slowly scanned through the target molecule transition, which is modulated at a high frequency and subsequently demodulated at a higher frequency. This typical detection strategy was adopted to remove i) low frequency drifts in lase intensity and ii) excess laser noise (varies as 1/f). Thus laser intensity does not hamper the molecule absorption measurement leading to enhance the SNR. The modulation technique has been characterised as frequency modulation and wavelength modulation depending on the frequency in which the laser is modulated. When the modulation frequency is lower than the absorption line-width of target molecule it is said to be WMS. However, FMS occurs when the modulation frequency is greater than the absorption line width [20-21].

Uehara *et.al.* reported about the measurement of two important trace gases i.e. methane isotopes and N_2O isotopes utilising WMS technique [22]. Chaux and Lavorel recently reported $^{13}CO_2/^{12}CO_2$ isotope ratio measurement using WMS strategy coupled with tuneable diode laser operating at 1.6 μm [23]. Reid et. al. reported the detection of NO_2 at the 100 ppt level using a tunable diode laser and 1-m multi-pass cell using the wavelength modulation technique [24]. Inspite of being more complicated and complex than WMS technique, people have also used FMS technique for trace gas measurement. The FMS technique coupled with tunable diode laser was demonstrated for measurements of CO_2, CH_4, N_2O, and CO in air samples [25].

3.5.2 Cavity enhanced absorption spectroscopy (CEAS): CRDS and ICOS

Over the past two decades, cavity-enhanced absorption spectroscopy marked a revolution in the field of trace gas detection with high sensitivity. In CEAS technique, the gas cell comprises of two ultra-low-loss mirrors making cavity high-finesse and traps photons inside the cavity for finite periods of time. In 1988, O'Keefe and Deacon first introduced a CEAS technique, which is known as a pulsed absorption cavity ring-down spectroscopy (CRDS) technique [26]. In CRDS technique, the decay time of radiation trapped in an optical resonator with a high quality factor is measured. The decay event was occurred due to rapidly turning off the injected laser power after active locking of the laser frequency with the cavity mode. The presence of two high reflectivity mirrors (~99.99%), aligned parallel to each other, offer several kilometre path lengths inside the ring-down cavity (RDC), which exceeds the best performance of multi-pass cell spectroscopy. Generally, absorption of the intracavity medium has been characterized by monitoring the exponential decay of light leaking out from the CRDS cell and the absorption spectrum of target analyte inside the RDC cell has been obtained from the difference between total cavity losses and empty cavity losses. Next, the unknown concentration of target gas can be determined easily using absorption cross-section and line shape parameter without any secondary calibration further [27]. A compact CRDS system can

achieve detectable absorption limit~10^{-10}. Later in 1998, Anthony O'Keefe introduced a new variation of CRDS technique known as integrated cavity output spectroscopy (ICOS) **[28]**. In this CEAS technique, absorption spectra are obtained through direct attenuation methods. However, it provides a detection sensitivity comparable to CRDS technique. In the ICOS technique approach, an absorption spectrum was obtained by simply integrating the transmitted output of the high-finesse optical resonant cavity during scanning the wavelength through the absorption feature of the target molecule **[29-30]**. The system simplicity of optical alignment, the capability to use wide-ranging spectral bandwidth light sources, low cost are some salient advantages for this technique for analysis trace gases.

In a study by the B.L. Fawcett *et.al,* continuous wave cavity ring-down spectroscopy at 1.65 µm has been demonstrated for methane measurement with minimum detection limit around 52 ppb **[31]**. High-resolution cavity ring-down spectrometer coupled with Near-infrared cw-Diode Laser was described in Y.B. He *et.al* for Nitrous Oxide and Chloroform measurement **[32]**. D.S. Baer demonstrated the ICOS technique for sensitive measurement of important trace molecules CO, CH_4, C_2H_2 and NH_3 in 1.5-1.65 µm wavelength region **[33]**. M.R. McCurdy et.al utilized QCL–based ICOS for real time monitoring exhaled breath nitric oxide (NO) concentration **[30]**.

3.5.3 Cavity enhanced absorption spectroscopy coupled with modulation strategy: NICE-OHMS and CE-WMS

Noise-immune cavity-enhanced optical heterodyne molecular spectroscopy (NICE-OHMS) is laser-based highly sensitive spectroscopic gas detection system **[34-35]**. This technique offers a unique combination of cavity enhancement strategy along with frequency modulation. The cavity enhance method increases the molecular interaction path length inside the cavity, whereas frequency modulation diminishes the 1/f noises simultaneously leading to achieve high SNR. This exclusive detection strategy was first demonstrated by Ye in 1998. Incorporating a high finesse optical cavity along with widely tuneable lasers, detection limit can be achieved up to 10^{-12} cm^{-1} for the NICE-OHMS **[34]**. In a study

by F. M. Schmidt et.al. a minimum detection level for C_2H_2 concentration measurement up to ppt has been achieved using the NICE-OHMS technique **[36]**. C. Ishibashi has recorded hyperfine spectra of methyl iodine (CH_3I) using NICE-OHMS technique coupled with the near infrared laser operating at 1.65 μm **[37]**.

However, to avoid the sophisticated technical requirements of the NICE-OHMS (like complex laser/cavity locking and high mechanical stability of the cavity), which is inappropriate for in-situ trace gas monitoring, off-axis alignment of integrated cavity output spectroscopy (OA-ICOS) in conjunction with wavelength modulation technique has been implemented. The advantage of using CE-WMS technique is that $1/f$ laser excess noise along with base line slope has been totally supressed by use of the second harmonic ($2f$) detection technique of WM **[38]**. Such derivative detection strategy enhances the SNR to several order in comparison to conventional OA-ICOS technique. Recently, Bakhirkin et.al. developed WMOA-ICOS setup coupled with a mid-infrared quantum cascade laser operating at 5μm and detected biogenic NO at sub-ppbv levels **[39]**. They have found that noise equivalent detection sensitivity improved five times by the use of WMOA-ICOS in comparison with conventional OA-ICOS approaches. Kasyutich et. al. reported WM-OA-ICOS with $2f$ detection strategy for oxygen measurements at 687.1 nm **[40]**. They have found that detection sensitivity increased 7 times better than OA-ICOS.

3.6 Significance of isotopic trace gas monitoring

The concentration analysis of stable isotopes composition of greenhouse gas has become very important as this provides important information about the gas sources and sinks **[41-43]**. The physical, chemical and biological processes cause the variation of natural abundances of minor isotopes in atmospheric trace gases and each process leaves the isotopic signature in their sources and sinks. Researcher generally used to do the quantitative water isotope measurement from ice core and isotopic measurements on the sediment of carbonates to get unique information regarding past climate change. However, carbon isotopes have been utilized to separate oceanic and

terrestrial biospheric exchanges of carbon with the environment [44-45]. ^{14}C, ^{13}C and ^2H signatures of methane (CH_4) have also been monitored to identify the several kinds of natural sources [46-48]. The stable isotopes monitoring of N_2O ($\delta^{15}N$ and $\delta^{18}O$) in the dissolved aquatic system has been observed to monitor how N_2O production and emission from aquatic ecosystems influence the atmosphere [49]. In recent years in the field of environmental application, researcher frequently used water molecules, having an isotopic composition of hydrogen and oxygen molecule to find out the precipitation of water sources and post-precipitation process during groundwater recharge [50]. Although, isotope study has also immense importance in atmospheric chemistry to get an in-depth real understanding of isotopic fractionation (mass-dependent or mass-independent) process in molecular level happening in real environment [51].

In recent years, monitoring stable isotopes in human exhaled breath has become a promising field for clinical disease diagnostic. Most of the breath isotope tests are based on ingestion of ^{13}C atoms labelled substrate [52]. In 1973, Lacroix M et.al. used naturally occurring ^{13}C substrate (^{13}C-glucose) for a metabolic study in human subjects for the first time [53]. Those ingested ^{13}C compounds are eventually metabolised and oxidised subsequently in the physiological processes like digestion and absorption to yield $^{12}CO_2$, $^{13}CO_2$ and H_2O and any enrichment or depletion of carbon isotopes in exhaled breath with respect to time indirectly provides the knowledge of intestinal metabolism of the substrate. Later, in 1987, Graham et. al. first introduced the first ^{13}C-urea breath test (^{13}C-UBT) to detect the presence of human gastric pathogen *H. pylori.* In this isotopic breath test, the pharmacokinetics of $\delta^{13}C$ in exhaled breath in response to urease enzyme activity has been utilised to distinguish the *H. pylori* infected from normal subjects [54]. However, people have also keen interest on analysis of stable hydrogen and oxygen isotopes for measurement of total energy expenditure, quantification of total body water, measurement of body insulin resistance of human subjects [55].

3.7 Spectroscopic database and transition lines selection

The selection of the transition line for a target molecule is crucial for trace gas detection with high sensitivity and selectivity. It is noteworthy to mention that the spectroscopic database has paramount importance to identify such absorption line, which has strong absorption cross-section along with interference free from other important gases. Several databases containing spectroscopic information are present nowadays (see table 3.2).

Table 3.2 *Different spectroscopy database*

Name of Spectroscopic database	Reference
HITRAN (*High Resolution Transmission*) Molecular Absorption Database	[56]
HITEMP (*High Temperature Molecular Spectroscopic Database*)	[57]
GEISA (*Gestion et Etude des Informations Spectroscopiques Atmospheriques*) Spectroscopic Database	[58]
PNNL (*Pacific Northwest National Laboratory*) Vapor Phase Infrared Spectral Library	[59]
ATMOS (*Atmospheric Trace Molecule Spectroscopy*) Database	[60]
NIST (*National Institute of Standards and Technology*) Infrared Spectroscopy Database	[61]
BT2 (*A high accuracy computed water line list*) Spectroscopic list	[62]
CDSD (*Carbon Dioxide Spectroscopic Databank*)	[63]

This database software is not a modelling code for transmission or radiance, however, it connects a bridge between molecular absorption input and modelling codes. All these codes, which have been applied rapidly to Lambert-Beer law to get simulated absorption spectra, belong to certain atmospheric model and methods. To get all the necessary molecular parameters from HITRAN, which are universally accepted, the user has to supply the temperature profiles, molecular constituent profiles, and geometric limits to these codes. In recent years, the advancement of the HITRAN makes a user eligible for characterising exsosolar planetary and planetary atmosphere. However, the accuracy of the parameter, got from HITRAN, must need to be improved still. In the

present-day HITRAN contains over millions of transition lines for so many molecules from almost zero wavenumbers to UV-visible wavenumber after its invention about 50 years back **[64]**. In a nutshell, HITRAN provides useful resources to scientists from trace gas detection to sophisticated radiative transfer calculations.

3.8 Reference

[1] J.I. Steinfeld, *Molecules and Radiation: An introduction to Modern molecular spectroscopy* (Dover Reprint Edition, 2005)

[2] J.M. Hollas, *Modern Spectroscopy* (John Wiley and Sons Ltd; England, 1996)

[3]https://hitran.org/lbl/5?output_format_id=1&iso_ids_list=76%2C77%2C105&vib_bands=&numin=1280&numax=1380

[4] M.Matsuura, P. R.Wood, G.C.Sloan, & AA. Zijlstra, Spitzer observations of acetylene bands in carbon-rich asymptotic giant branch stars in the Large Magellanic Cloud, **Mon. Not. R. Astron. Soc.**, 2006, 371, 415.

[5] R. Zander, C.P. Rinsland, D.H. Ehhalt, J. Rudolph, Ph. Demoulin, *Vertical column abundances and seasonal cycle of acetylene, C_2H_2, above the Jungfraujoch station, derived from IR solar observations*, **J.Atmos. Chem.** ,1991, 13, 359–372.

[6] J. Rudolph, A. Khedin, B. Bonsang, *Self-broadening coefficients and absolute line intensities in the v_4+ v_5 band of acetylene,* **J. Geophys. Res.**, 1992, 97 6181–6188.

[7] J. Vander Auwera, *Absolute intensities measurements in the v_4+v_5 band of $^{12}C_2H_2$: analysis of Herman–Wallis effects and forbidden transitions,* **J. Mol. Spectrosc.**, 2000,201 143–150.

[8] P.W. Atkins, *Physical chemistry* (Oxford University Press, 2002.)

[9] M. Lackner, *Tunable diode laser absorption spectroscopy (TDLAS) in the process industries – A review*. **Rev. Chem. Eng.** 2007, 23, 65–147.

[10] J. Haas, B.Mizaikoff, *Advances in Mid-Infrared Spectroscopy for Chemical Analysis.* **Annu. Rev. Anal. Chem.** 2016, 9, 45–68.

[11] M. Lassen, L. Lamard, D. Balslev-Harder, A. Peremans, J.C. Petersen, *Mid-infrared photoacoustic spectroscopy for atmospheric NO2 measurements.* **In Proceedings of the SPIE OPTO, San Francisco, CA, USA, 30 January–1 February**, 2018; p. 7.

[12] H. Huszár, A.Pogány, Z. Bozóki, Á. Mohácsi, L. Horváth, G.Szabó, *Ammonia monitoring at ppb level using photoacoustic spectroscopy for environmental application.* **Sens. Actuator B-Chem.** 2008, 134, 1027–1033.
[13] R. Ghorbani, F.M. Schmidt, *Real-time breath gas analysis of CO and CO2 using an EC-QCL.* **Appl. Phys. B-Lasers Opt.**, 2017, 123.

[14] L. Liu, B.Xiong,; Y.Yan, J. Li,; Z. Du, *Hollow Waveguide-Enhanced Mid-Infrared Sensor for Real-Time Exhaled Methane Detection*. **IEEE Photonics Technol. Lett.,** 2016, 28, 1613–1616.

[15] H. Jane, P.T. Ralph, *Optical gas sensing: A review.* **Meas. Sci. Technol.,** 2013, 24.

[16] D.J. Miller, K. Sun, L.Tao,; M.A. Khan, M.A. Zondlo, *Open-path, quantum cascade-laser-based sensor for high-resolution atmospheric ammonia measurements*. **Atmos. Meas. Tech.** 2014, 7, 81–93.

[17] C.Bauer,; A.K.Sharma,; U. Willer,; J.Burgmeier,; B. Braunschweig,; W. Schade,; S. Blaser,; L. Hvozdara,; A. Müller,; G.Holl, *Potentials and limits of mid-infrared laser spectroscopy for the detection of explosives*. **Appl. Phys. B-Lasers Opt.** 2008, 92, 327–333.

[18] D. Rojas, P. Ljung, O. Axner, *An investigation of the 2f-wavelength modulation technique for detection of atoms under optically thin as well as thick conditions.* **Spectrochim. Acta**, Part B 1997, 52, 1663–1686.

[19] H.D. Wizemann, *Application of the 2f-wavelength modulation technique for the measurement of large lithium isotope ratios by diode laser graphite furnace atomic absorption spectroscopy*. **Spectrochim. Acta,** Part B 1999, 54, 1267–1278.

[20] J. Reid and D. Labrie, *Second-harmonic detection with tunable diode lasers – comparison of experiment and theory*, **Appl. Phys. B** 26, 203–210 (1981).

[21] G. N. Rao, C. Gudipaty, and D. Martin, *Higher harmonic detection employing wavelength modulation spectroscopy and near infra-red diode lasers: an undergraduate experiment*, **Am. J. Phys.** 77, 821–825 (2009).

[22] Uehara, K. *Dependence of harmonic signals on sample-gas parameters in wavelength-modulation spectroscopy for precise absorption measurements*. **Applied Physics B**, 1998, 67, 517–523.

[23] R. Chaux, B. Lavorel, *Relative line intensity measurement in absorption spectra using a tunable diode laser at 1.6 mm: application to the determination of $^{13}CO_2/^{12}CO_2$ isotope ratio*. **Applied PhysicsB**, 2001, 72, 237–240.

[24] J.Reid, M. El-Sherbiny, B.K. Garside, E.A. Ballik, *Sensitivity limits of a tunable diode laser spectrometer, with application to the detection of NO_2 at the 100-ppt level*. **Appl. Opt.** 1980, 19, 3349.

[25] T. Gulluk, H.E.Wagner, F. Slemr, *A high-frequency modulated tunable diode laser absorption spectrometer for measures of CO_2, CH_4, N_2O, and CO in air samples of a few cm^3.*, **Rev. Sci. Instrum.** 1997, 68, 230.

[26] A. O'Keefe and D. A. G. Deacon, *Cavity ring-down optical spectrometer for absorption measurements using pulsed laser sources*, ***Rev. Sci. Instrum.*** 1988, **59**, 2544-51.

[27] M. Mazurenka, A.J. Orr-Ewing, R. Peverall and G. A. D. Ritchie Cavity ring-down and cavity enhanced spectroscopy using diode lasers *Annu. Rep. Prog. Chem. Sect.*, *2005* **101**, 100-42.

[28] O'Keefe *A Integrated cavity output analysis of ultra-weak absorption*, **Chem. Phys. Lett.** 1998, **293**, 331-6.

[29] M. R.McCurdy, Y. Bakhirkin, G. Wysocki, F. K. Tittel, *Performance of an exhaled nitric oxide and carbon dioxide sensor using quantum cascade laser-based integrated cavity output spectroscopy*. **Journal of Biomedical Optics**, 2007, 12.

[30] Y. A. Bakhirkin, A. A.Kosterev, C. Roller, , R. F.Curl, F. K. Tittel,. *Midinfrared quantum cascade laser based off-axis integrated cavity output spectroscopy for biogenic nitric oxide detection*. **Applied Optics**, 2004, 43, 11, 2257–2266.

[31] B. L. Fawcett, *Trace detection of methane using continuous wave cavity ring-down spectroscopy at 1.65 μm,* **Phys. Chem. Chem. Phys.**, 2002, **4**, 5960-5965.

[32] Y.B. He, M. Hippler, M. Quack, *High-resolution Cavity Ring-down Absorption Spectroscopy of Nitrous Oxide and Chloroform using a Near-infrared cw Diode Laser*, **Chem. Phys. Lett.**,1998, 289(5-6), 527–534.

[33] D.S. Baer, J.B. Paul, J.B. Gupta, A. O'Keefe, *Sensitive Absorption Measurements in the Near-infrared Region using Off-axis Integrated-cavity-output Spectroscopy*, **Appl. Phys. B-Lasers Opt.**, 2002, 75(2-3), 261–265.

[34] J. Ye, L. S. Ma, and J. L. Hall, *Ultrasensitive detections in atomic and molecular physics: demonstration in molecular overtone spectroscopy*, **J. Opt. Soc. Am. B**, 1998, **15**(1), 6–15.

[35] A. Foltynowicz, F. M. Schmidt, W. Ma, and O. Axner, *Noise-immune cavity-enhanced optical heterodyne molecular spectroscopy: Current status and future potential*, **Appl. Phys. B**, 2008, **92**(3), 313–326 (2008).

[36] F. M. Schmidt, A. Foltynowicz, W. Ma, and O. Axner, *Fiber-laser based noise-immune cavity-enhanced optical heterodyne molecular spectrometry for Doppler-broadened detection of C_2H_2 in the parts per trillion range*, **J.Opt. Soc. Am.**, (2007), **24**(6), 1392–1405.

[37] C. Ishibashi, and H. Sasada, *Near-infrared laser spectrometer with sub-Doppler resolution, high sensitivity, and wide tunability: A case study in the 1.65-μm region of CH3I spectrum*, **J. Mol. Spectrosc.** 2000, 200(1), 147–149.

[38] V.L. Kasyutich, C.E. Canosa-mas, S. Pfrang, S. Vaughan, R.P. Wayne, *Off-axis continuous-wave cavity-enhanced absorption spectroscopy of narrow-band and broadband absorbers using red diode lasers*, **Appl. Phys. B**, 2002, **75**, 755.

[39] Y.A. Bakhirkin, A.A. Kosterev, C. Roller, R.F. Curl, F.K. Tittel, *Mid-infrared quantum cascade laser based off-axis integrated cavity output spectroscopy for biogenic nitric oxide detection*, **Appl. Opt.,** 2004, 43, 2257.

[40] V.L. Kasyutich, C.E. Canosa-mas, S. Pfrang, S. Vaughan, R.P. Wayne, *Off-axis continuous-wave cavity-enhanced absorption spectroscopy of narrow-band and broadband absorbers using red diode lasers*, **Appl. Phys. B**, 2002,75, 755.

[41] J.A. Kaye, *Mechanism and observations for isotopic fractionations of molecular species in planetary atmosphere*, **Rev. Geophys.** 1987, 28, 1609-1658.

[42] P. Ciais, P.P. Tans, J.W.C. White, M. Trolier, R.J. Francey, J.A. Berry, D.R. Randall, P.J. Sellers, J.G. Collatz and D.S. Schimel, *Partitioning of ocean and land uptake of CO_2 as inferred by $\delta^{13}C$ measurements from the NOAA Climate Monitoring and Diagnostics Laboratory Global Air Sampling Network*, **J. Geophys.** *Res.* 1995, D100, 5051-5070.

[43] D.C. Lowe, C.A.M. Brenninkmeijer, G.W. Brailsford, K.R. Lassey, A.J. Gomez and E.G. Nesbit, *Concentration and ^{13}C records of atmospheric methane in New Zealand and Antarctica: Evidence for changes in methane sources*, **J. Geophys. Res.** 1994, *99*, 16913-16925.

[44] P. Ciais, P. Tans, J. W. White, R. Francey, M. Trolier, J. Berry, D. Randall, P. Sellers, J. Collatz, D. Schimmel,. *The global carbon budget inferred from a new worldwide data set of ^{13}C measurements in atmospheric CO_2.* **J. Geophys. Res**, 1995, 100 D3, 5051–5070.

[45] R. J. Francey, , P. Tans, C.E. Allison, I.G. Enting, J.W.C. White, M.Trollier, *Changes in oceanic and terrestrial carbon uptake since*, **Nature**, 1995, 373, 326–330,.

[46] P. Bergamaschi, , C.A.M. Brenninkmeijer, P.J. Crutzen, N.F. Elansky, I.B. Belikov, N.B.A. Trivett, D.E.J. Worthy, *Isotopic analysis based source identification for atmospheric CH4 and CO sampled across Russia using the Trans-Siberian railroad*, **J. Geophys. Res.**, 1998, 103, 8227-8235.

[47] J.M.Conny, L.A. Currie, *The isotopic characterization of methane, non-methane hydrocarbons and formaldehyde in the troposphere*, **Atmos. Environ.** 1996, 30, 621–638.

[48] D. C. Lowe, , M.R. Manning, G.W. Brailsford, A.M. Bromley, *The 1991–1992 atmospheric methane anomaly: Southern hemisphere 13C decrease and growth rate fluctuations*, **Geophys. Res. Lett.** 1997, 24, 857–860.

[49] S. J. Thuss, J. J. Venkiteswaran, S. L. Schiff, *Proper Interpretation of Dissolved Nitrous Oxide Isotopes, Production Pathways, and Emissions Requires a Modelling Approach.* **PLoS ONE**, (2014), 9(3): e90641. doi:10.1371/journal.pone.0090641.

[50] K. Gupta and R. D. Deshpande, *Groundwater isotopic investigations in India:What has been learned?* **Current Science**, 2005, 89, 825-835.

[51] C. A. M. Brenninkmeijer, C. Janssen, J. Kaiser, T. Röckmann, T. S. Rhee, S. S. Assonov, *Isotope Effects in the Chemistry of Atmospheric Trace Compounds*, **Chem. Rev**.2003, 103, 12, 5125-5162.

[52] LT. Weaver, *Stable isotope breath tests*. **Nutrition**, 1998, **14**, 826–9.

[53] M. Lacroix, F. Mosora, M. Pontus, P. Lefebvre, A. Luyckz and G. Lopez-Habib, *Glucose naturally labelled with carbon-13: use for metabolic studies in man*, **Science**, 1973, 181, 445–6.

[54] D. Graham, D. Jr. Evans, L. Alpert, P. Klein, D. Evans, A. Opekun and T. Boutton, *Campylobacter pylori detected non-invasively by the (13)C-urea breath*, **Lancet**, 1987, 1, 1174–7.

[55] E. S. Berman, S. L. Fortson, S. P. Snaith, et al. *Direct analysis of $\delta^2 H$ and $\delta^{18}O$ in natural and enriched human urine using laser-based, off-axis integrated cavity output spectroscopy.* **Anal. Chem.**, 2012, 84(22), 9768–9773. doi:10.1021/ac3016642.

[56] I. E. Gordon, L. S. Rothman, C. Hill, R. V. Kochanov, Y. Tan, P. F. Bernath, et al. *The HITRAN 2016 molecular spectroscopic database*. **Journal of Quantitative Spectroscopy and Radiative Transfer.** 2017, 203, 3-69. DOI: 10.1016/j.jqsrt.2017.06.038.

[57] L. S. Rothman, I. E. Gordon, R. J. Barber, H. Dothe, R. R. Gamache, A. Goldman, et al. *HITEMP, the high temperature molecular spectroscopic database*. **Journal of Quantitative Spectroscopy and Radiative Transfer**. 2010, 111, 2139-2150. DOI: 10.1016/j. jqsrt.2010.05.001.

[58] N. Jacquinet-Husson, R. Armante, N. A. Scott, A. Chedin, L. Crepeau, C. Boutammine, et al. *The 2015 edition of the GEISA spectroscopic database*, **Journal of Molecular Spectroscopy**. 2016, 327, 31-72. DOI: 10.1016/j. jms.2016.06.007.

[59] S. W. Sharpe, T. J. Johnson, R. L. Sams, P. M. Chu, G. C. Rhoderick, P. A. Johnson. *Gas-phase databases for quantitative Infrared Spectroscopy - Principles, Advances, and Applications infrared spectroscopy*. **Applied Spectroscopy.** 2004, 58(12), 1452-1461. DOI: 10.1366/0003702042641281.

[60] L. R. Brown, M. R. Gunson, R. A. Toth, F. W .Irion, C. P. Rinsland, A. Goldman , *atmospheric trace molecule spectroscopy (ATMOS) linelist.*, **Applied Optics,** 1996, 35(16), 2828-2848. DOI: 10.1364/AO.35.002828.

[61] P. M. Chu, F. R. Guenther, G. C. Rhoderick, W. J. Lafferty. *The NIST quantitative infrared database.* **Journal of Research of the National Institute of Standards and Technology**., 1999, 104(1), 59-81. DOI: 10.6028/jres.104.004.

[62] R. J. Barber, J. Tennyson, G. J. Harris, R. N. Tolchenov. *A high-accuracy computed water line list.* **Monthly Notices of the Royal Astronomical Society.,** 2006, 368(3), 1087-1094. DOI: 10.1111/j.1365-2966.2006.10184.

[63] S. A. Tashkun, V. I. Perevalov. *CDSD-4000: High-resolution, hightemperature carbon dioxide spectroscopic databank.* **Journal of Quantitative Spectroscopy and Radiative Transfer.** 2011, 112(9), 1403-1410. DOI: 10.1016/j.jqsrt.2011.03.005.

[64] Laurence S.Rothman, *The evolution and impact of the HITRAN molecular spectroscopic database*, **Journal of Quantitative Spectroscopy and Radiative Transfer,** 111(11), 2010, 1565-1567.

Chapter 4

Development of *Cw*-EC-quantum cascade laser (QCL) coupled cavity ring down spectrometer and its validation

4.1 Introduction

Recently, cavity ring down spectroscopy (CRDS) has become one of the attractive laser spectroscopy techniques for sensitive trace gas detection. The principle of CRDS technique is based on a combination of direct absorption spectroscopy (DAS) coupled with a high finesse optical cavity. In a conventional DAS method, the number density of target particles have been obtained by monitoring intensity attenuation of the light through the sample and this intensity attenuation is caused due to frequency dependent absorption of the molecules. However, in the presence of weak absorber, intensity attenuation due to absorption has been dominated by inherent laser intensity fluctuation, which limits the sensitivity. But in CRDS, this limitation can be overcome easily, as the decay rate of the light intensity inside the high finesse cavity is measured to calculate the concentration of the unknown sample. Thus the measurement becomes insensitive to shot-to-shot laser intensity fluctuations leading to the achievement of ultra-high sensitivity of 10^{-9}-10^{-11} cm^{-1}, corresponding to measurement capability of trace molecular species as low as parts-per-trillion (ppt) levels. In 1988, O'Keefe and Deacon first introduced the CRDS technique by monitoring the O_2 overtone spectra using a pulsed laser [1]. Since then this spectroscopic technique has become more promising gas sensing tool for ultra-high sensitive and quantitative trace gas measurement in a laboratory environment as well as in-situ measurement also. Later Le Grand and Le

Floch first demonstrated continuous wave light source coupled cavity ring down spectrometer to measure the optical parameter of a high finesse cavity [2]. Several excellent reviews and publications are existing on this spectroscopic technique [3-8], which are very useful to gather the knowledge regarding its application in a different field [9-18]. However, this technique has proven its important role in atmospheric chemistry.

The recent invention of QCL enhances the importance of the CRDS technique enormously for selective detection of trace gases with ultra-high sensitivity [19-22]. The salient features of QCL such as room temperature operation, very narrow line width, and unparalleled access to the mid-IR make the CRDS system a highly sensitive and field deployable trace gas sensor for real-time monitoring of atmospheric constituents and exhaled air traces for medical diagnostic. In this research work, we have selected the working wavelength of QCL in between 7.5 μm to 8 μm, because many important atmospheric trace molecules, pollutants and breath biomarkers have strong fundamental absorption characteristics in this wavelength region (see the figure 4.1). In this chapter, we will briefly discuss the principles of operation of the CRDS technique, sensitivity measurement and its practical design.
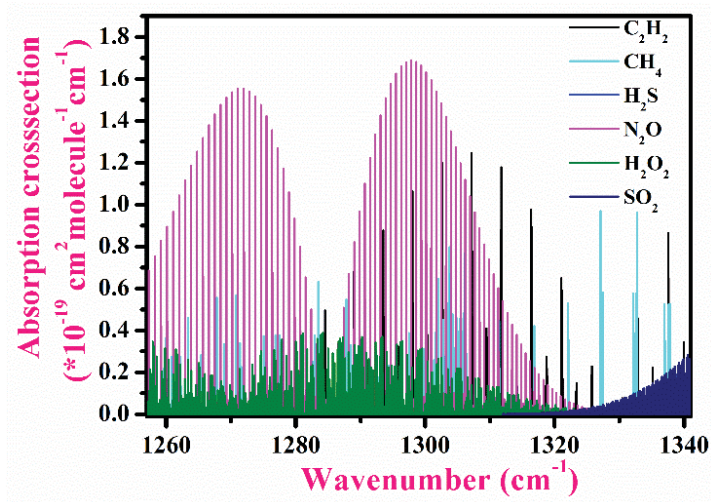
Figure 4.1 *HITRAN simulation of important trace molecules within the wavenumber region of our deployed QCL tuning range.*

4.2 Principle of CRDS technique

The basic principle of cavity ring-down spectrometer is depicted in figure 4.2. In CRDS technique, an optical cavity is comprised of two ultra-high reflectivity (~0.9999), dielectric-coated, concave mirrors leading to form an optical resonator into which laser light is injected. When the small fraction of the laser light is coupled with the high finesse optical cavity through the optical axis, it starts to make back and forth motion inside the cavity and with each reflection, a small amount of light leaks from the cavity due to the slight imperfection of the mirrors.
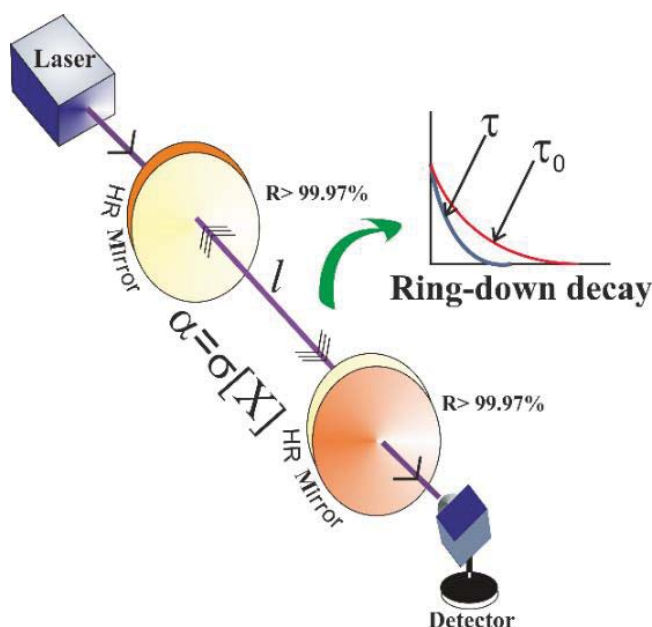
Figure 4.2 *Schematic representation of the principle of the CRDS technique.*

The temporal evolution of leaking light from one of the mirrors is detected through a photosensitive detector and shows an exponential nature of decaying optical intensity. In absence of the absorber or presence of loss mechanism inside the cavity, the time dependence of exponential decay light intensity from an optical cavity can be expressed as

$$I(t) = I(t = 0)e^{-\frac{t}{\tau_0}} \qquad \qquad 4.1.1$$

$$\text{where } \tau_0 = \frac{L}{c|lnR|} = \frac{L}{c(1-R)} \text{ for R~1} \qquad 4.1.2$$

τ_0 is the empty cavity ring-down time, which depends on mirror reflectivity R and cavity length L and c is the speed of the light. For

example, mirrors, having R=0.9999 and cavity length L= 50 cm, $\tau_0 =$ 16.7 μs can be obtained associated with distance travelled by trapped light inside the cavity around 5 km. Now in the presence of absorber inside the cavity, the ring down time becomes dependant on both mirror reflectivity and absorbance of the sample, which can be expressed as [23];

$$I(t) = I(t = 0)e^{-\frac{t}{\tau}} \qquad \textbf{4.2.1}$$

$$\text{where } \tau = \frac{L}{c[(1-R)+\alpha L]} \qquad \textbf{4.2.2}$$

α is the sample absorption coefficient and L is the sample path length, equivalent to cavity length because the sample fills the whole cavity. Now to get absorption spectra like shown in the figure 4.8, the $\tau(v)$ and $\tau_0(v)$ need to be recorded experimentally.

$$\alpha(v) = \frac{\Delta k(v)}{c} \qquad \textbf{4.3.1}$$

$$\text{where } \Delta k = \frac{1}{\tau(v)} - \frac{1}{\tau_0(v)} \qquad \textbf{4.3.2}$$

In equation 4.3.2, k denotes the decay rate and Δk signifies the change of decay rate of the cavity in the presence and absence of sample respectively. $\alpha(v)$ is considered as the absorption coefficient, which is defined as the product of the frequency dependant absorption cross-section, σ(v), and the molecular concentration, [X].

$$\alpha(v) = \sigma(v)[X] \qquad \textbf{4.4}$$

So the unknown concentration of the target molecule can be obtained from the equation 4.4 with prior knowledge of absorption cross-section. Likewise, frequency dependent absorption cross-section can also be calculated from equation 4.4 with known concentration value.

4.3 Sensitivity

The minimum value of the absorption coefficient is defined as limiting sensitivity of the spectrometer, which can be determined from the equation (4.5.2);

$$\alpha = \frac{\Delta k(\nu)}{c} = \frac{\frac{1}{\tau} - \frac{1}{\tau_0}}{c} = \frac{\tau - \tau_0}{c\tau\tau_0} \qquad \textbf{4.5.1}$$

$$\text{or } \alpha_{min} = \frac{\Delta\tau}{c\tau_0^2} = \frac{1-R}{L}\frac{\Delta\tau}{\tau_0} \qquad \textbf{4.5.2}$$

when $\tau \to \tau_0$ (in low absorption regime)

$\frac{\Delta\tau}{\tau_0}$ is obtained from the relative error of experimentally measured empty cavity ring-down. The reduction of $\frac{\Delta\tau}{\tau_0}$ value can be possible by ensuring low electrical noise and good mechanical stability of the cavity. However, the sensitivity can also be expressed as a minimum measurable concentration by dividing the α_{min} with wavelength dependent peak absorption cross-section, which is sometimes called as detection limit of the spectrometer.

$$[X]_{min} = \frac{\alpha_{min}}{\sigma(\nu)} \qquad \textbf{4.6}$$

The detection limit is sometimes also expressed in terms of a mixing ratio expressed in ppmv (parts per million by volume i.e 1 part in 10^6), ppbv (parts per billion by volume i.e 1 part in 10^9) and pptv (parts per trillion by volume i.e 1 part in 10^{12}).

Noise equivalent absorption (NEA) coefficient is an alternative approach to define the sensitivity (see the equation 4.7) [24], which is expressed typically in units of cm^{-1}Hz$^{-1/2}$.

$$NEA = \sqrt{\frac{2}{f_{rep}}}\,\alpha_{min} \qquad \textbf{4.7}$$

where f_{rep} is the data accumulation rate.

It is clear from equation 4.7 that the NEA value can be improved by increasing the data accumulation rate highly. Generally, CRD based spectrometer can achieve NEA value upto 10^{-8} to 10^{-10} cm^{-1}Hz$^{-1/2}$.

4.4 Cavity stability and cavity mode matching

In CRD spectrometer, the presence of two high reflectivity mirrors forms a Fabry-Pérot etalon, where specific longitudinal modes can be

sustained. Thus, the optical stability of the cavity should be maintained to trap the light inside the cavity. However, in case of unstable cavities, light leaves the optical cavity after a few roundtrips due to the increase of wide transverse angle. Thus a cavity g-parameter, which is a function of cavity length (L) and radius of curvature (r) (see equation 4.8), has been defined as a stability factor [25].

$$g = 1 - \frac{L}{r} \qquad \textbf{4.8}$$

The stability condition of a cavity has been calculated to avoid the diffraction losses from mirrors edges and which is found to be:

$$0 \le g_1 g_2 \le 1 \qquad \textbf{4.9}$$

For our CRDS setup, we have chosen two mirrors with ROC 1m and cavity length 0.5 m, which gives a product of $g_1 g_2 = 0.25$, leading to form a symmetric cavity. Actually, a stable cavity offers longer optical pathlength, which subsequently enhances the capability of ultra-sensitive measurement.

As we know a stable CRD cavity behaves as a good Fabry-Pérot etalon, the condition required for standing waves formation inside the cavity is that accumulated phase change for a complete round trip should be an integral multiple of 2π. The frequency spacing of such longitudinal modes is defined as the free spectral range (FSR). The FSR for symmetry cavity can be expressed as;

$$\Delta v = \frac{c}{2L} \qquad \textbf{4.10}$$

For our developed setup, the FSR is found to be 300 MHz (0.01 cm^{-1}) for 50 cm cavity length.

However, to understand the mode structure of the cavity, the finesse of the cavity is required to be defined. Actually, the finesse of the cavity is the measurement of the sharpness of the mode or width of the cavity mode. Equation 4.11.1 gives the form of the finesse (F) and full width half maximum (FWHM) of cavity mode can be calculated from F (see the equation 4.11.2)

$$F = \frac{\pi\sqrt{R}}{1-R} \qquad\qquad \textbf{4.11.1}$$

$$\Delta v_{1/2} = \frac{\Delta v_{FSR}}{F} \qquad\qquad \textbf{4.11.2}$$

Therefore, sharp cavity modes can be obtained by increasing cavity finesse. For our CRDS system, F is obtained with value 26000 for mirror reflectivity 0.9998 and cavity length around 50 cm, and cavity width is calculated ($\Delta v_{1/2}$ =11.26 kHz) using equation 4.11.2.

The mode matching event for the cw-CRDS system is quite tricky, because laser light, which is coupled with a cavity, has very narrow line-width (~2 MHz). As the line width is very small in comparison with FSR of the cavity, extra effort has been put to ensure overlap of the laser and cavity mode frequency.
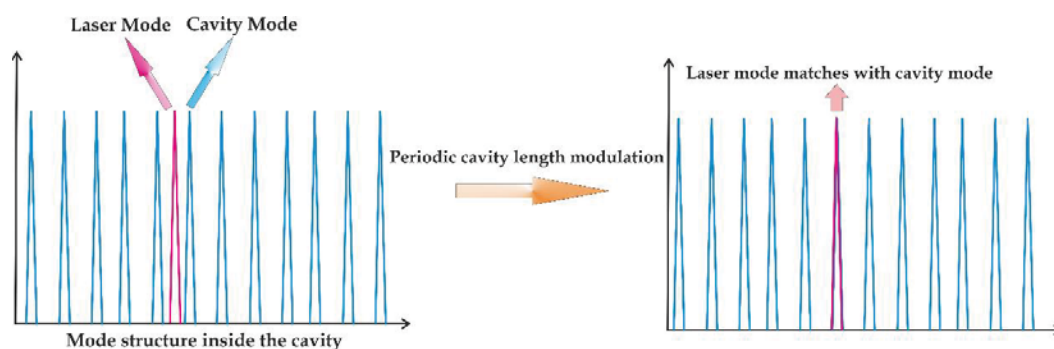
Figure 4.3 *Schematic representation of mode structure inside the cavity and mode matching of laser mode and cavity mode during cavity length modulation.*

In our set-up, we actually followed the cavity length modulation technique to make resonance between laser frequency and cavity frequency. This has been done by applying ramp voltage to the one of the cavity mirror mounts containing a piezo-electric transducer. At a particular voltage, the cavity length is modulated to such a way that laser frequency comes to resonance with cavity mode frequency and an intracavity light is built up (as shown in the figure 4.4).

Figure 4.4 *Screen shot of National instrument scope in the desktop of data acquisition PC during the experiment. The red coloured triangular voltage periodically modulates the cavity length and the subsequently green coloured spike is appeared due to generating intracavity light for mode matching inside the cavity.*

4.5 Ring down event for cw-CRDS

After successfully coupling of cw laser source into cavity, intracavity light has to be switched off to allow the ring down event. Practically, the switch off of the laser has been initiated using a fast optical switch such as acoustic optical modulator (AOM).
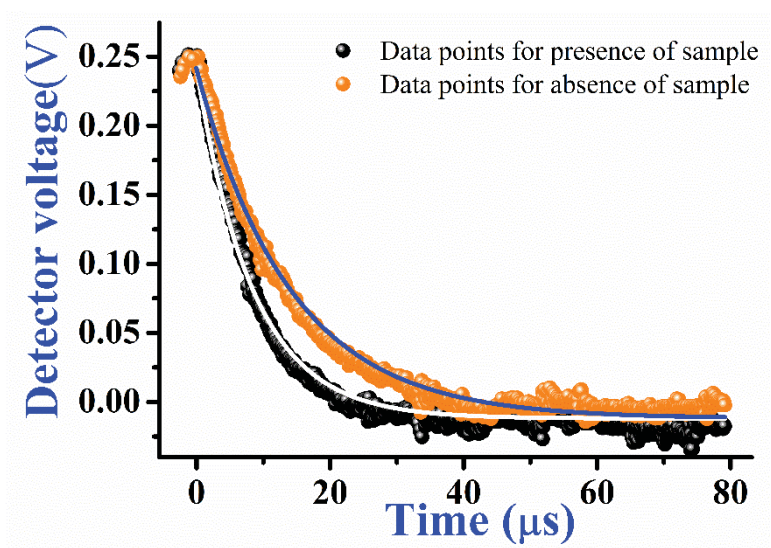
Figure 4.5 *An experimental cw CRD trace in presence and absence of gas sample in the side cavity. The blue and white lines are the 1st order best fit of exponential decay to the acquired data points.*

58

The AOM usually extinguished cavity input of the laser when the detector signal reached to a preselected threshold value and an external trigger circuit sends a signal to AOM for allowing exponential decay of intracavity light. Figure 4.5 demonstrates the ring-down event, where orange-line is a first order exponential to the data set. The switching off of the laser has been done to ensure that no accidental mode matching contaminates the single exponential decay.

4.6 Allan variance

In many spectroscopic methods, monitoring system stability has been observed by doing Allan variance analysis to improve the detection limit. The Allan-variance, named after David W. Allan, provides the method which summarises variability of temporal data as a function of the time integration period [26]. However, this variance analysis also calculates the optimum integration time of the system to get the maximum signal to noise ratio. For our lab made cw-CRDS set-up, we have used Allan variance as a tool to check the overall system stability. Equation 4.12 is actually used to calculate the Allan variance

$$\sigma_A^2 = \frac{1}{2}(A_2 - A_1) \qquad\qquad \textbf{4.12}$$

where A_1 and A_2 are the averages of adjacent time series data. Figure 4.6 demonstrated the Allan variance curve for our CRDS system, where σ_A^2 value of empty cavity ring-down time has been plotted against integration time in logarithmic scale.
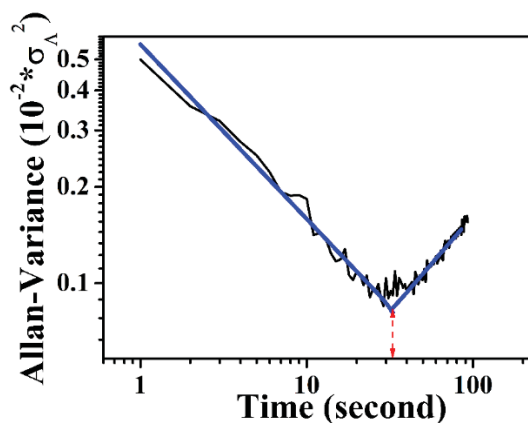
Figure 4.6 *A graph of Allan variance σ_A^2 against integration time. The blue straight lines denote the linear best fits to the dataset.*

It is clear from the figure that as integration time increases, the Allan variance decreases due to increasing data averaging leading to increase the SNR. However long term instabilities such as drift in alignment, mechanical vibration initiate to decrease SNR, then Allan variance starts to increase. So we investigated the stability of the cw-CRD spectrometer by means of Allan variance analysis to determine the optimum integration time to get the maximum signal to noise ratio and thereby improving the limiting sensitivity of the current method. We found an optimum integration time of 33 seconds which corresponds to 3300 ring-down decay signals for 100 Hz data acquisition rate and a noise-equivalent absorption coefficient (NEA) of 1.86×10^{-9} cm^{-1}Hz$^{-1/2}$.

4.7 Experimental setup

Figure 4.7 demonstrates a schematic diagram of a typical cw-CRD spectrometer coupled with a mid-IR EC-QCL. In a brief description, water cooled continuous wave external cavity quantum cascade laser (MHF-41078; Daylight Solutions, USA), having very narrow line width (<0.0003 cm^{-1}), with mode-hop-free tuning range (1341 cm^{-1}–1257 cm^{-1}) was deployed here like a laser source.
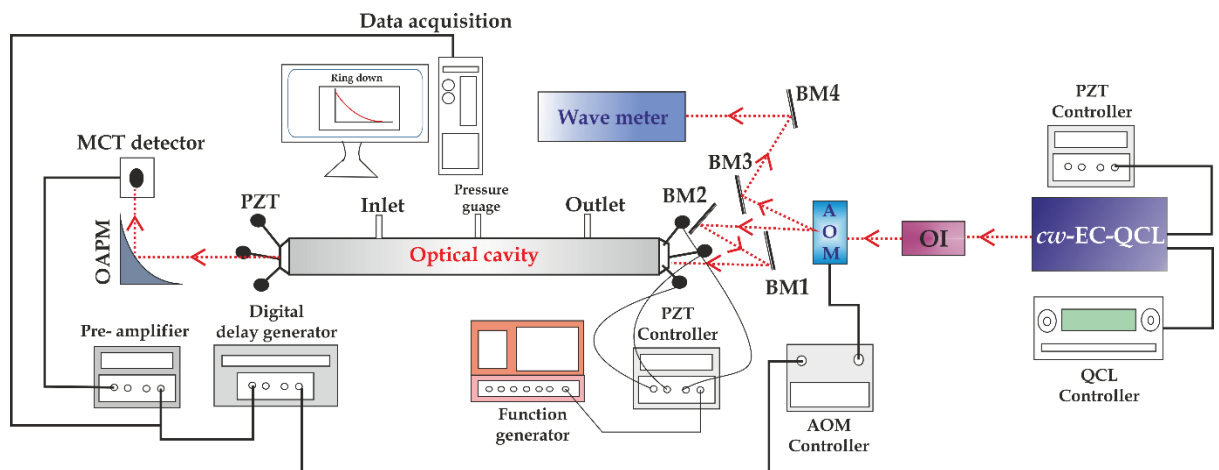
**Figure 4.7:** *Schematic representation of our developed cw-EC-QCL coupled CRD spectrometer at 7.5 μm wavelength region.*

The laser was then coupled with help of gold coated bending mirrors (BM1 and BM2) to quartz coated stainless steel high-finesse optical cavity of 50 cm length, comprising with two high-reflective super mirror (CRD Optics Inc.; USA) with reflectivity R > 99.98% at 7.35 μm. Before entering

into the cavity, the laser beam was passed through an optical isolator (FIO-5-7.8; Innovation Photonics) and Acousto-optic modulator (AOM) (AOM; AGM406B11M; IntraAction Corp; USA). AOM helped to diffract the beam in two directions, one of the beams went to wave-meter (621B-MIR; Bristol Instruments) for monitoring the high-resolution wavenumber and other beam went to the central axis of cavity ring down cell for fulfilling the mode matching criterion. Now to achieve mode matching phenomena between fundamental transverse modes inside the CRD cell and laser beam, one mirror of the gas cell, mounted on a piezo-electric transducer (PZT, Thorlabs PE4), was modulated with 50 Hz frequency for sweeping the cavity mode frequency over one free spectral range. Then the AOM was used for quickly and efficiently termination of laser beam with help of pulse-delay generator (DG645; Stanford Research Systems) to achieve concentration dependant decay event of intra-cavity light, which was focused on mid-infrared detector (PVI-4TE-8-1X1; Vigo System S.A.) by gold-coated 90^0 off-axis parabolic mirror (50338 AU; Newport Corporation). The detector signal was sent to the personal computer to calculate ring-down time with the help of lab made LabVIEW program. The ring-down time in empty cavity gas cell was achieved to be 14.1 μs corresponding to an optical path length around 4.2 km inside the cavity. Now to scan the target absorption line, the piezo of the external cavity of QCL was utilised to tune the laser finely. However, to record another absorption spectra, the grating position of the EC-QCL was adjusted to achieve another frequency of QCL. The gas cell is also equipped with a pressure gauge, which can measure the pressure inside the cavity upto 760 Torr with 2% accuracy.

The cw-CRDS absorption spectrum of H_2S is being depicted in figure 4.8. The spectrum was recorded by injecting a certified gas mixture of (5±0.1) ppm of H_2S by probing transition at 1335.8573 cm^{-1}, which is originated due to fundamental bending vibrations (v_2). In CRDS absorption spectra, change of decay rate against wavenumber has been plotted.
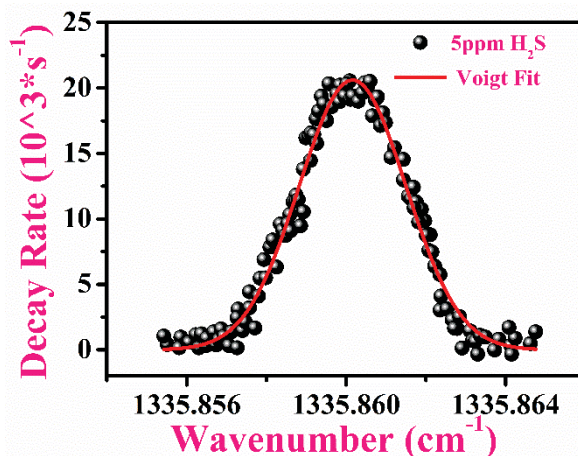
Figure 4.8 *cw-CRDS absorption spectrum of hydrogen sulphide (H₂S) transition line at 1335.8573 cm⁻¹. The circular data point was obtained from the analysis of exponential decay during the ring-down event at different laser wavenumber.*

The pressure inside the cavity was kept 15 Torr during spectrum accumulation. The area under the peak is utilized to calculate the concentration in the cavity of the target molecule with the prior knowledge of integrated absorption cross section value from the HITRAN database. So we obtained the concentration of H₂S of 2.43×10^{12} molecule cm⁻³ inside the cavity with known absorption cross section value of the probed line σ_{H_2S} = 9.50×10^{-22} cm²molecule⁻¹cm⁻¹ from HITRAN database.

4.8 Conclusion

In this chapter, development and implementation of a high-resolution *cw*-CRDS spectrometer coupled with a widely-tunable EC-QCL with MHF wavelength tuning capability working in the mid-IR spectral region of 7.5 μm for high resolution molecular spectroscopy has been demonstrated. We tested the system for quantitative estimation of $H_2^{32}S$ without any sample pre-concentration unit. The minimum detection sensitivity for H₂S has been obtained around 2.3 ppb for 1 atm cavity pressure. This CRDS spectrometer can easily be utilized for monitoring several other important trace species with mid-IR fundamental absorption bands such as CH_4, SO_2, HNO_3, C_2H_2, H_2O_2 etc. with anticipated detection limits in the pptv range.

4.9 Reference

[1] A. O'Keefe and D. A. G. Deacon, *Cavity ring-down optical spectrometer for absorption measurements using pulsed laser sources*, **Rev. Sci. Instrum.** 1988, 59, 2544-51.

[2] Y. Le Grand, et al., *Sensitive Diffraction-Loss Measurements of Transverse Modes of Optical Cavities by the Decay-Time Method*, **Journal of the Optical Society of America B: Optical Physics**, 1990, 7, 1251-1253.

[3] J. J. Scherer, J. B. Paul, A. O'Keefe, Saykally, *Cavity ringdown laser absorption spectroscopy: history, development, and application to pulsed molecular beams*, **R. J. Chem.Rev.** 1997, 97, 25.

[4] M. D. Wheeler, S. M. Newman, A. J. Orr-Ewing and M. N. R. Ashfold, *Cavity ring-down spectroscopy*, ***J. Chem. Soc., Faraday Trans.,*** **1998**, *94*, 337.

[5] K. W.Busch, M. A. Busch, *Cavity ring-down spectroscopy: an ultratrace-absorption measurement technique*, **American Chemical Society: Washington, DC**, 1999.

[6] G. Berden, R. Peeters, G. Meijer, *Cavity ring-down spectroscopy: experimental schemes and applications*. **Int. Rev. Phys. Chem.,** 2000, 19, 565.

[7] D. B. Atkinson, *Solving chemical problems of environmental importance using cavity ring-down spectroscopy*, **Analyst**, 2003, 128, 117.

[8] S. S. Brown, , *Absorption spectroscopy in high-finesse cavities for atmospheric studies*, **Chem. Rev.,**2003**, 103, 5219.

[9] A. J.Hallock, E. S. F.Berman, R. N. Zare, *Direct monitoring of absorption in solution by cavity ring-down spectroscopy*, **Anal. Chem.**, 2002, 74, 1741.

[10] S. Xu, G.Sha, J. Xie, *Cavity ring-down spectroscopy in the liquid phase*, **Rev. Sci. Instrum.,** 2002, 73, 255.

[11] K. L. Snyder, R. N. Zare, *Cavity ring-down spectroscopy as a detector for liquid chromatography*, **Anal. Chem.** 2003, 75, 3086.

[12] R. Engeln, G. von Helden, A. J. A.van Roij, G. Meijer, *Cavity ring down spectroscopy on solid C60*, ***J. Chem. Phys.,*** 1999, 110, 2732.

[13] D.Kleine, J. Lauterbach, K. Kleinermanns, P. Hering, *Cavity ring-down spectroscopy of molecularly thin iodine layers,* **Appl.Phys. B,** 2001, 72, 249.

[14] S. Logunov, *Cavity ringdown detection of losses in thin films in the telecommunication wavelength window*, **Appl. Opt.**, 2001, 40, 1570.

[15] G. A. Marcus, H. A. Schwettman, *Cavity ringdown spectroscopy of thin films in the mid-infrared,* **Appl. Opt.,** 2002, 41, 5167.

[16] A. D. Sappey, E. S.Hill, T. Settersten, M. A.Linne, *Fixed-frequency cavity ringdown diagnostic for atmospheric particulate matter*, **Opt. Lett.,** 1998, 23, 954.

[17] J. E. Thompson, B. W. Smith, J. D. Winefordner, *Monitoring atmospheric particulate matter through cavity ring-down spectroscopy*, **Anal. Chem.**, 2002, 74, 1962.

[18] R. L. Vander Wal, T. M. Ticich, *Cavity ringdown and laser-induced incandescence measurements of soot*, **Appl. Opt.**,1999, 38, 1444.

[19] G. Dutta Banik, S. Som, A. Maity, M. Pal, S. Maithani, S. Mandal, M. Pradhan. *An EC-QCL based N_2O sensor at 5.2 µm using cavity ring-down spectroscopy for environmental applications:* **Analytical Methods,** 2017, DOI: 10.1039/C7AY00482F.

[20] A. De, G. Banik, A. Maity, M. Pal, M. Pradhan, *A cw external-cavity quantum cascade laser-based high-resolution cavity ring-down spectrometer for ultrasensitive trace gas detection*: **Optics Letters**, 2016**,** 41(9), 1949**.**

[21] S. Maithani, S. Mandal, A. Maity, M. Pal, M. Pradhan, *High-resolution spectral analysis of ammonia near 6.2 µm using a cw EC-QCL coupled with cavity ring-down spectroscopy*, **Analyst**, 2018, 143 (9), 2109-2114.

[22] G.D. Banik, A. Maity, S. Som, M. Pal, M. Pradhan *An external-cavity quantum cascade laser operating near 5.2 µm combined with cavity ring-down spectroscopy for multi-component chemical sensing*, **Laser Physics**, 2017, 28 (4), 045701.

[23] P. Zalicki, R. N. Zare, *Cavity ring-down spectroscopy for quantitative absorption measurements*, **J. Chem. Phys.**, 1995, 102, 2708.

[24] R.D. vanZee, J.T. Hodges, J.P. Looney, *Pulsed, single-mode cavity ringdown spectroscopy,* **Appl. Opt.,** 1999, 38 , 3951-3960.

[25] H. Kogelnik and T. Li, *Laser Beams and Resonators*, **Applied Optics**, 1966, 5, 1550-1567.

[26] P.Werle, R.Mücke, & F. Slemr, *The limits of signal averaging in atmospheric trace-gas monitoring by tunable diode-laser absorption spectroscopy (TDLAS)*,**Appl.   Phys.   B**,1993,   57,   131. https://doi.org/10.1007/BF00425997

Chapter 5

Simultaneous monitoring of ^{32}S, ^{33}S and ^{34}S isotopes of H$_2$S using cavity ring-down spectroscopy with an external-cavity quantum cascade laser at 7.5 μm

5.1 Introduction

Three stable isotopologues of hydrogen sulphide (H$_2$S), i.e. H$_2{}^{32}$S, H$_2{}^{33}$S, and H$_2{}^{34}$S, are worthwhile to study sulphur isotope geochemistry in nature owing to their relatively large percentage mass differences and comparatively high natural abundances (i.e. 94.98%, 0.75%, and 4.21%, respectively) [1,2]. The sulphur isotopes of H$_2$S are the tracers of sulphur flux in the atmosphere, rivers, lake water, and ground water, and consequently the analysis of sulphur isotopic composition of H$_2$S is particularly important to identify and evaluate the impact of natural and anthropogenic sources of sulphur compounds on the environment. Moreover, monitoring of the sulphur isotopes provides valuable information about biological sulphur cycle, marine sedimentary cycle, nature and origin of fossil fuels, and effect of volcanic eruptions [1]. Nevertheless, exposure to even a trace level of H$_2$S (less than 150 ppb) has an immense impact on human health and safety [3]. Furthermore, the change in H$_2$S concentration in human breath has been potentially linked with cardiovascular diseases as well as several gastrointestinal disorders [3, 4]. Therefore, there is considerable research interest for selective and sensitive detection of trace H$_2$S levels along with its isotopes in ambient air.

The mid-infrared (mid-IR) spectral region (i.e. 3-8 μm) is of particular interest for studying isotopes of a molecule due to the presence of molecular fundamental fingerprint vibrational bands in this region. H_2S has two fundamental vibrational bands around 3.8 μm and 7.5 μm originated from anti-symmetric stretching and bending modes of vibration, respectively [2]. However, the transitional line-intensity at 7.5 μm region is almost one order of magnitude higher compared to the region of 3.8 μm, and the region is free from significant overlapping absorption features from the transition lines of water vapour (H_2O) and carbon dioxide (CO_2). Moreover, the spectral region of 7.5 μm provides inherent advantages for isotope-specific detection of H_2S. It is noteworthy to mention that the isotopic fractionations occurring between H_2S and sulphur dioxide (SO_2) is an important parameter to explore sulphur isotope geochemistry [1], and SO_2 has also the strongest fundamental vibrational band in this region [2], thus providing a unique opportunity for precise monitoring of sulphur isotopic fractionations. Furthermore, a very few transitions of S^{34} isotope of H_2S at 7.5 μm region has been enlisted in the HITRAN database [2], which offers a future scope to explore new transition lines of that isotope in this region. In contrast, simultaneous monitoring of H_2S along with nitrous oxide (N_2O) and methane (CH_4) has the immense importance in atmospheric science as well as in biomedical science, and the spectral region of 7.5 μm is the perfect region to exploit the possibility of such measurement. However, the recent innovation of external-cavity quantum cascade laser (EC-QCL) technology and the availability of mid-IR optics open up a new frontier facilitating access to the entire mid-IR region. The salient features of EC-QCL, i.e. extremely narrow linewidth (< 5MHz), mode-hop-free (MHF) tunability, high optical power, and room-temperature operation, make it an ideal choice of light source for probing the fundamental vibrational bands in the mid-IR spectral region [5,6].

To our knowledge, there is currently no report of monitoring the sulphur isotopes of H_2S in ambient air. However, there are few studies in the literature which mainly focused on the trace detection of H_2S exploiting the transition line within 7-8 μm spectral region. Moser *et al.* [7]

reported a minimum detection limit of 1.5 ppm (parts per million; 10^{-6}) for H_2S utilizing a ring-cavity surface-emitting quantum-cascade laser (RCSE-QCL) coupled to 100 metre (m) Herriot cell. In contrast, Nikodem *et al.* [8] employed a distributed feedback (DFB) QCL operating at 7.2 μm to achieve a detection limit of 140 ppb (parts per billion;10^{-9}) for H_2S in a 76 m Herriot cell. Furthermore, Siciliani de Cumis *et al.* [9] demonstrated quartz-enhanced photoacoustic spectroscopy (QEPAS) to attain a minimum detection of 450 ppb of H_2S using a tuneable EC-QCL between 7.6 and 8.3 μm. In another study [10], Helman and co-workers reported a detection limit of 492 ppb of H_2S using QEPAS method. On the other hand, Moser *et al.* [11] achieved a limit of detection of 150 ppb H_2S employing wavelength modulation spectroscopy (WMS) with a DFB-QCL at 8 μm. However, the detection limit of H_2S is required to be further improved for an optical sensor to be eventually applied for field applications. The high-sensitive optical cavity-enhanced absorption techniques such as cavity ring-down spectroscopy (CRDS), which provides an optical pathlength of several kilometres, [5,6] along with an EC-QCL operating around 7.5 μm will be a perfect combination to further improve the detection limit of H_2S. The CRDS technique provides high-temporal and spatial resolution, and subsequently allows direct quantitative absorption measurements in a high-finesse optical cavity without a secondary calibration standard [12-16].

In the present study, we report for the first time, the simultaneous monitoring of three stable sulphur isotopes, i.e. S^{32}, S^{33} and S^{34} of H_2S within a single scanning range of 0.4 cm^{-1} utilizing ultra-sensitive CRDS technique coupled to a continuous-wave (cw) EC-QCL operating around 7.5 μm. We next explored the interference-free 7 transition lines of $H_2{}^{32}S$ isotope and 2 transition lines of $H_2{}^{33}S$ isotope within the MHF tuning range of the cw EC-QCL. The high-resolution CRDS spectra will be useful for trace sensing of different H_2S isotopes in different environments with high sensitivity and molecular specificity. Finally, we utilized the EC-QCL based CRDS technique for simultaneous monitoring of three important hazardous gases N_2O, CH_4, and H_2S within a small tuning range probing the respective fundamental vibrational transitions.

5.2 Experimental arrangement

In the present study, we have utilized our developed cavity ring-down (CRD) spectrometer coupled with an external-cavity quantum cascade laser (EC-QCL) operating around 7.5 μm. The experimental setup of the CRD spectrometer has been demonstrated elsewhere in detail [5]. Briefly, the widely tuneable, room-temperature, continuous wave (*cw*) EC-QCL (TLS-41053, Daylight Solutions, USA) with MHF tuning range between 1257 cm^{-1} and 1340 cm^{-1} was coupled to a high-finesse optical cavity comprising of two high reflectivity (HR) mirrors (R≥99.90%) at the two ends of a 50 cm long quartz-coated cylindrical gas cell. The high-finesse cavity was further connected to a vacuum pump and Mass flow controllers (MKS units) to accurately regulate the sample pressure inside the cavity. The sample pressure inside the cavity is monitored utilizing a pressure gauge attached to it. Furthermore, an acoustic optic modulator (AOM) (AGM-406B11M, IntraActionCorp.) was employed as an optical switch to achieve ring-down signal. The optical signal was acquired using a thermoelectrically cooled photovoltaic MCT detector (VIGO PVI-4TE-8), whereas a high precision wavemeter (621B, Bristol Instruments, USA) was utilized to monitor the laser wavelengths in real-time with an accuracy of ±0.001 cm^{-1}. The ring-down signal was eventually analyzed using a custom-written LabVIEW programme and a high speed data acquisition card (PCI 5122, National Instruments).

5.3 Results & Discussions

5.3.1 CRDS set-up assessment

We achieved an empty cavity ring-down time of τ_0= 14.05 μs with a standard deviation (1σ) of 0.56 % for an averaging of 5 successive ring-down events in the current cw EC-QCL based CRDS system. The empty cavity ring-down time (τ_0) implies an effective optical path length of ~4.2 km between two HR mirrors, which eventually enhances the sensitivity of the system. A limiting sensitivity of α_{min}=1.33 x 10^{-8} cm^{-1} was estimated for this system, which corresponds to the noise equivalent absorption (NEA) coefficient of 1.88 x 10^{-9} cm^{-1} Hz$^{-1/2}$ for the data acquisition rate of 100 Hz. We also calculated the reflectivity of the HR cavity mirrors to be

~99.98 % from the experimental empty cavity ring-down time and subsequently the finesse of the optical cavity was determined to be 26000. All these parameters ensure the potential of the present EC-QCL based CRDS technique for studying high-resolution and high-sensitive spectral features of molecular absorptions.
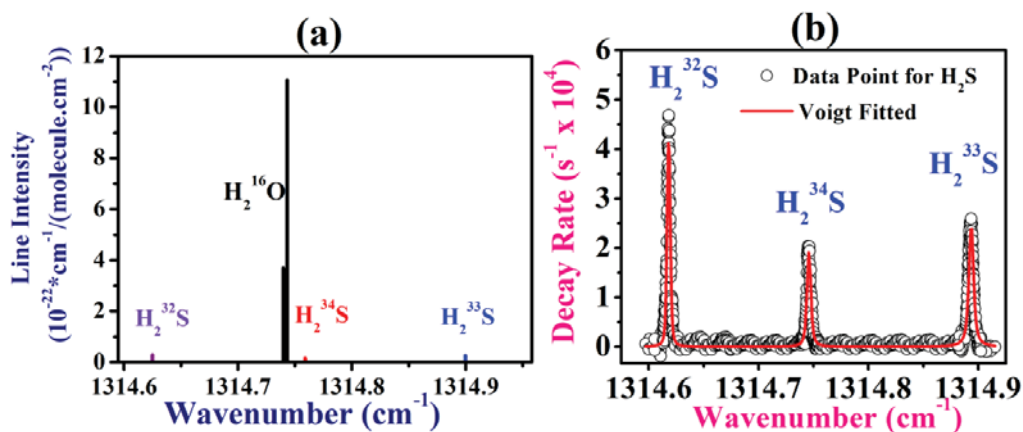
Figure 5.1 (a) *A HITRAN simulation illustrating the line-intensity (normalized with isotopic abundances) of different isotopic species present within the spectral range of 1314.6-1315.0 cm^{-1}.* **(b)** *The experimental ring-down spectra of S^{32}, S^{33}, and S^{34} isotopes of H$_2$S exploiting the natural abundances of the individual species present in the calibration standard fitted with the Voigt function. The decay rate represents the baseline (empty-cavity decay rate) subtracted change of decay rate in presence of sample against the scanning wavenumber.*

5.3.2 Absorption line selections and system validation by using standard calibration gas mixture

We next performed a spectroscopic simulation of H$_2$S absorption lines within the MHF tuning range (1260 cm^{-1}-1340 cm^{-1}) of the present EC-QCL using HITRAN-PC 4.2 and subsequently identified the appropriate spectral region to simultaneously probe the H$_2{}^{32}$S, H$_2{}^{33}$S and H$_2{}^{34}$S isotopes within a single scanning range of 0.40 cm^{-1} (Fig.5.1a). The simulation was executed under the experimental conditions of 4.2 km pathlength with 20 Torr pressure, and at 25°C temperature. The selected transitions were originated from the fundamental bending vibrations (v_2) of the respective isotope of H$_2$S. We, thereafter, tuned the laser frequency across the selected range to acquire the experimental ring-down spectra of the three isotopes in a single laser scan using a standard calibration gas

mixture of 327.6±0.5 ppm of H_2S in N_2 (MATHESON) (Fig. 5.1b). We exploited the natural abundances of the respective isotopes of H_2S in the calibration gas mixture to acquire simultaneously the ring-down spectra of $H_2^{32}S$, $H_2^{33}S$, and $H_2^{34}S$ isotopes. The experimental spectra was achieved by plotting decay rate (s^{-1}) (i.e. inverse of ring-down time) against the scanning wavenumber (cm^{-1}). We subsequently calculated the natural abundance of each sulphur isotope in the calibration gas mixture with the prior knowledge of line-integrated absorption cross-section of each isotope from the HITRAN database. We found the natural abundances of $H_2^{32}S$, $H_2^{33}S$ and $H_2^{34}S$ isotopes to be 94.29±0.16%, 0.805±0.002%, and 4.89±0.01%, respectively in the calibration mixture. We, thereafter, confirmed the natural abundance of each sulphur isotope of H_2S measuring the ion currents of all the isotopes at their respective mass number of 34, 35, and 36 utilizing our in-house mass-spectrometry system [17].

5.3.3 Validation of the measurements in real environment

However, the selected spectral region of 1314.532 - 1314.922 cm^{-1} to simultaneously monitor all three stables isotopes of H_2S was required for the validation of the measurements in real environment due to the presence of absorption lines of H_2O vapour (Fig. 5.1a).
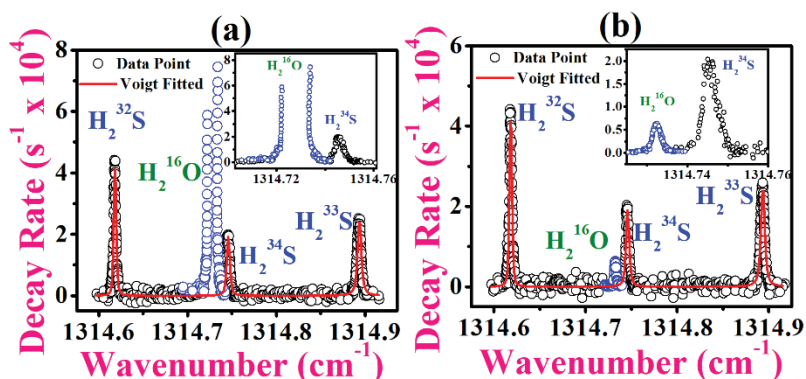
Figure 5.2 *The experimental CRDS spectra of calibration standard demonstrating the change of decay rate with the wavenumber for $H_2^{32}S$, $H_2^{33}S$, and $H_2^{34}S$ isotopes in presence of water vapour (a) without pre-treatment, and (b) after pre-treatment using a nafion dryer.*

Therefore, we prepared a real sample mixing the calibration standard with the ambient air (of 0.4% water vapour) and subsequently measured this sample without any sample pre-treatment. We found that the ring-down signal was getting saturated as the laser frequency crosses the H_2O absorption line, as depicted in Fig. 5.2a.

However, the absorption spectra of the sulphur isotopes were unaffected in the presence of atmospheric concentration of water vapour at the sample pressure of 20 Torr inside the cavity. Nevertheless, the saturation spectrum of the water vapour was eventually removed from the acquired signal with the incorporation of a nafion dryer (Brunswick Instrumentation Ltd., MD-050-72S-2) prior to the sample injection (Fig. 5.2b).

5.3.4 Allan variance analysis for system precision measurement

We, thereafter, performed the Allan-variance test of the measured concentrations of each isotope to check the system stability and measurement precision. We found that the present system can measure $H_2^{32}S$, $H_2^{33}S$, and $H_2^{34}S$ isotopes with a precision of 1190 ppb, 13 ppb and 124 ppb, respectively for the respective integration times of 264 sec, 261 sec, and 247 sec (Fig. 5.3 a, b and c). Thus, the selected spectral region coupled to the QCL combined with CRDS technique has enormous potential to be applied for field applications.
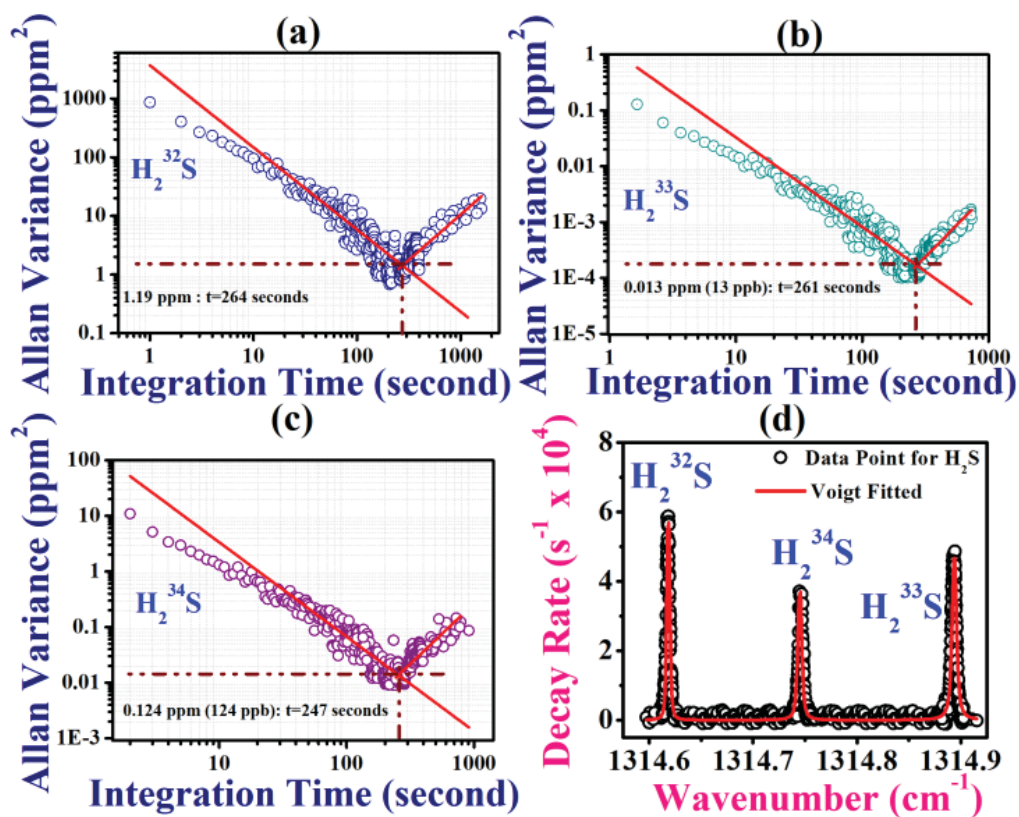
Figure 5.3 *The Allan variance analysis for the measurement precision of the individual isotope of (a) $H_2{}^{32}S$, (b) $H_2{}^{33}S$ and (c) $H_2{}^{34}S$. (d) The experimental CRDS spectra exhibiting the abundances of the three stable sulphur isotopes present in the chemical compound of Na_2S.*

5.3.5 Real-time application of CRDS in sulphur isotopic fractionation chemistry

We thereafter exploited the spectral range along with the present system to map the abundances of sulphur isotopes of a chemical compound, sodium sulfide (Na_2S). To investigate the sulphur isotopes of Na_2S, we performed an in-vitro chemical reaction between Na_2S and hydrochloric acid (HCl) inside an enclosed flask under inert environment (N_2), and subsequently measured H_2S levels derived from the reaction to evaluate the abundances of sulphur isotopes present in Na_2S (Merck India). The typical ring-down spectra of the sulphur isotopes of H_2S is illustrated in fig. 5.3d which was acquired using the present CRDS system at the sample pressure of 6 Torr inside the optical cavity. The abundances of sulphur isotopes of Na_2S were determined to be 91.78±0.18%, 1.05±0.002% and 7.16±0.018% for S^{32}, S^{33}, and S^{34}

isotopes, respectively. The results indicate an isotopic enrichment of heavier isotopes of sulphur present in the chemical compound of Na_2S, and thus it may provide the valuable information about the sulphur isotopic fractionation chemistry.

5.3.6 Exploitation of full tuning range of EC-QCL for H₂S isotopes detection

Next, to exploit the full potential of the broad MHF tuning range (80 cm^{-1}) of the EC-QCL, we independently probed 7 transition lines of $H_2{}^{32}S$ isotope and 2 transition lines of $H_2{}^{33}S$ isotope within the entire MHF tuning range of the laser, which are specifically interference-free absorption lines from other molecular species and thus have enormous potential to be applied for trace sensing of H₂S isotopes. The experimental ring-down spectra of 7 transition lines of $H_2{}^{32}S$ isotope were acquired at sample pressure of 6 Torr using a calibration mixture of 26.5±0.5 ppm, whereas the spectra of $H_2{}^{33}S$ isotope were obtained at pressure of 20 Torr for 242.0±0.5 ppm calibration gas mixture of H₂S. Figure 5.4 depicted the experimental ring-down spectra of all the 9 transitions fitted with the Voigt line-shape function.
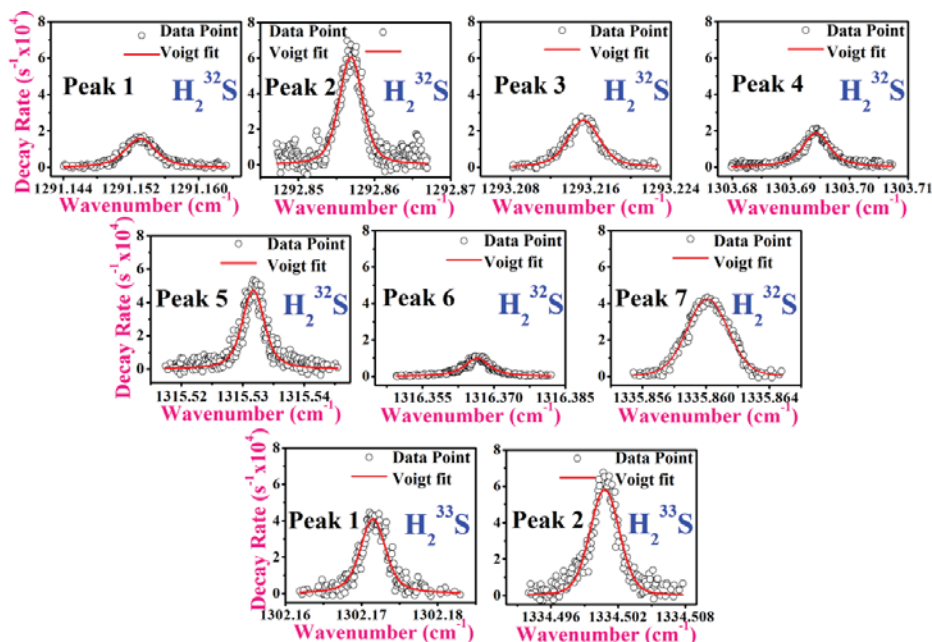
Figure 5.4 *The high-resolution experimental ring-down spectra of the selected interference-free transition lines of $H_2{}^{32}S$ and $H_2{}^{33}S$ isotopes around 7.5 µm. The decay rate represents the baseline (empty-cavity decay rate) subtracted change of decay rate in presence of sample against the scanning wavenumber.*

The comparison between the experimental and HITRAN values [2] of the line-positions of all the selected transition lines of $H_2^{32}S$, $H_2^{33}S$ and $H_2^{34}S$ isotopes along with their band assignments was shown in Table 5.1.

Table 5.1 *Comparison of experimental and HITRAN line-positions of different transitions of H_2S isotopes. The parenthesis digit of the experimental line-centre indicates the non-significant digit.*

Peak No.	Isotope Of H_2S	HITRAN Line-centre (cm^{-1})	Experimental Line-centre (cm^{-1})	Band Assignment ν_2 (000→010) Line Assignment (J, K_a, K_c)		Line Intensity (cm^{-1} mol^{-1})
				Lower-state local quanta	Upper-state local quanta	
1		1291.1611	1291.152(9)	4 4 0	5 5 1	5.900E-22
2		1292.8630	1292.856(9)	4 4 1	5 5 0	1.810E-21
3		1293.2192	1293.215(2)	4 3 2	5 4 1	8.100E-22
4		1303.7023	1303.694(2)	5 4 1	6 5 2	9.520E-22
5		1314.6249	1314.618(0)	14 1 13	14 2 13	2.790E-23
6		1315.5388	1315.531(8)	5 5 0	6 6 1	1.730E-21
7	$H_2^{32}S$	1316.3710	1316.366(5)	5 5 1	6 6 0	5.850E-22
8		1335.8574	1335.860(1)	6 5 2	7 6 1	9.500E-22
9		1302.1796	1302.171(5)	5 4 1	6 5 2	4.09E-23
10	$H_2^{33}S$	1314.8996	1314.893(0)	5 5 1	6 6 0	2.530E-23
11		1334.5080	1334.500(7)	6 5 2	7 6 1	4.130E-23
12	$H_2^{34}S$	1314.7590	1314.745(5)	5 5 0	6 6 1	1.440 E-23

Now, it is noteworthy to mention here that only 4 transition lines of $H_2^{34}S$ isotope in total are currently enlisted in HITRAN database within the entire MHF tuning range of the present EC-QCL [2], which opens up a

possibility to explore new transition lines of $H_2^{34}S$ isotope within this range. However, exploration of new transition lines of $H_2^{34}S$ isotope requires isotope specific calibration standard in absence of any standard database, and hence still remains open for future study.

We subsequently evaluated the efficacy of the present high-resolution CRDS system employing EC-QCL for trace sensing of H_2S levels in ambient air utilizing the transition line of $H_2^{32}S$ centred at ~1292.857 cm^{-1} (Table 5.1).

Table 5.2 *Comparison of detection limit of H_2S reported by different groups in mid-IR region.*

Reference	Transition Line (cm⁻¹)	Measuring Technique	Detection Limit (ppb)	Isotope Measurement
H. Moser *et al.* [7]	1247.2	2*f*-WMS along with multi-pass cell	150	Not studied
M. Helman *et al.* [10]	1234.58	QEPAS	492	Not studied
M. Nikodem *et al.* [8]	1389.3	2*f*-WMS along with multi-pass cell	140	Not studied
M. Siciliani de Cumis *et al.* [9]	1266.933	2*f*-QEPAS	450	Not studied
H. Moser *et al.* [11]	1234.5767	RCSE QCL along with multi-pass cell	1500	Not studied
Present Study	**1292.856**	**CRDS**	**20**	**$H_2^{32}S$, $H_2^{33}S$, and $H_2^{34}S$**

It is important to mention that the HITRAN database provides line-integrated absorption cross-section normalized by the natural abundance of each isotope and hence any isotopic transition line of H_2S can be exploited to obtain the total H_2S concentration of the measured sample. The limit of detection (1σ) of trace concentration of H_2S was estimated to be 20 ppb by targeting the transition of (4, 4, 1)→(5, 5, 0) centred at ~1292.857 cm^{-1} and keeping sample pressure of 30 Torr inside the optical

cavity along with an integration time of 250 seconds. In this study, the higher sample pressure has not been utilized so as to avoid any possible pressure-induced broadening of spectral feature of H_2S. Thereafter, we compared the detection sensitivity of H_2S in the present study with the earlier studies, as shown in Table 5.2. It is quite evident from Table 5.2 that the CRDS technique coupled with an EC-QCL operating at 7.5 μm significantly improves the detection limit of trace monitoring of H_2S.

5.3.7 Evaluation of EC-QCL coupled CRDS system for multicomponent sensing

Finally, we assessed the possibility of the multicomponent chemical sensing within a single laser scan utilizing the present mid-IR CRDS system operating at 7.5 μm. It has already been reported that CH_4 and N_2O both have strong fundamental vibrational bands around 7.5 μm, and both the molecular species have significant importance in environmental sensing [5]. Hence, we experimentally explored a small spectral region of 0.05 cm^{-1} to be probed in a single laser scan for simultaneous monitoring of CH_4, N_2O, and H_2S ($H_2^{32}S$). The high-resolution absorption spectrum of all three molecular species in a single laser scan has been illustrated in fig. 5.5. The experimental CRDS spectrum was acquired by using a calibration mixture of 7±0.05 ppm of CH_4, 0.2±0.01 ppm of N_2O, and 327.6 ±0.5 ppm of H_2S at a sample of pressure of 6 Torr inside the optical cavity. However, the simultaneous monitoring of CH_4, N_2O, and H_2S in a gas matrix with high sensitivity and molecular specificity by employing EC-QCL with CRDS methodology may lead to several potential applications in a wide range of fields such as industrial processing, environmental monitoring and biomedical diagnostics.
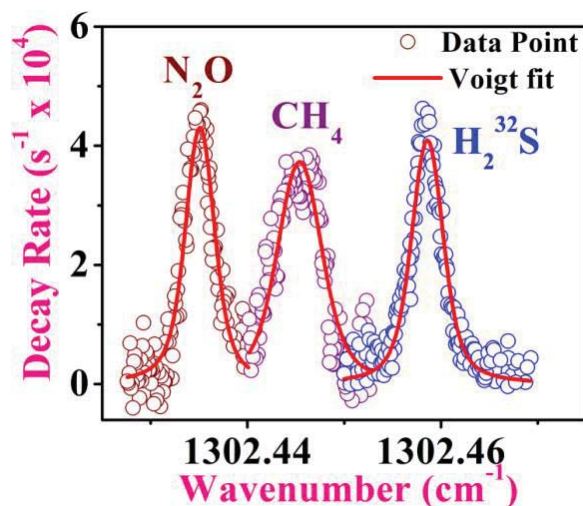
Figure 5.5 *The high-resolution experimental CRDS spectra of a gas matrix comprising of standard calibration mixtures of N_2O, CH_4 and $H_2{}^{32}S$ at the sample of pressure of 6 Torr inside the optical cavity.*

5.4 Conclusion

In the present study, we have demonstrated for the first time, the simultaneous monitoring of three stable sulphur isotopes, i.e. S^{32}, S^{33}, and S^{34} of H_2S within a single laser scan utilizing an optical high-sensitive CRDS technique coupled with a cw EC-QCL operating at 7.5 μm. We subsequently validated the system for the possibility of real-world application of tracking sulphur isotopic signatures in chemical compounds. We further explored the interference-free 9 transition lines of $H_2{}^{32}S$ and $H_2{}^{33}S$ isotopes independently within the MHF tuning range of the present EC-QCL for trace monitoring of individual isotopes of H_2S. We reported a minimum detection limit of 20 ppb at the pressure of 30 Torr for the integration time of 255 seconds. We thereafter utilized the high-resolution EC-QCL based CRDS system for simultaneous detection of multiple trace species such as CH_4, N_2O, and H_2S in a single laser scan with high sensitivity and molecular selectivity within a very narrow spectral range of 0.05 cm^{-1}. Hence, the present study provides a new approach of combining the unique spectral features of 7.5 μm, the high sensitivity of CRDS technique, and high-resolution as well as broad MHF tunability of EC-QCL for the development of a new-generation optical sensor to study isotopic species and multicomponent trace gas sensing.

5.5 References

[1] H.R. Krouse, and V.A. Grinenko, Stable Isotopes in the Assessment of Natural and Anthropogenic Sulphur in the Environment (John Wiley & Sons Ltd, 1991).

[2] I.E. Gordon, L.S.Rothman, C.Hill, R.V.Kochanov, Y.Tan, P.F.Bernath, M.Birk, V. Boudon, A.Campargue, K.V.Chance, B.J.Drouin, J.-M.Flaud, R.R.Gamache, J.T.Hodges, D.Jacquemart, V.I.Perevalov, A.Perrin, K.P.Shine, M.-A.H.Smith, J. Tennyson, G.C.Toon, H.Tran, V.G.Tyuterev, A.Barbe, A.G.Császár, V.M.Devi, T.Furtenbacher, J.J.Harrison, J.-M.Hartmann, A.Jolly, T.J.Johnson, T.Karman, I. Kleiner, A.A.Kyuberis, J.Loos, O.M.Lyulin, S.T.Massie, S.N.Mikhailenko, N. Moazzen-Ahmadi, H.S.P.Müller, O.V.Naumenko, A.V.Nikitin, O.L.Polyansky, M. Rey, M.Rotger, S.W.Sharpe, K.Sung, E.Starikova, S.A.Tashkun, J. VanderAuwera, G.Wagner, J.Wilzewski, P.Wcisło, S.Yu, and E.J.Zak, The HITRAN2016molecularspectroscopicdatabase. *Journal of Quantitative Spectroscopy & Radiative Transfer* **203** 3−69 (2017).

[3] L. Ciaffoni, R. Peverall, and G.A.D. Ritchie. Laser spectroscopy on volatile sulfur compounds: possibilities for breath analysis. *J. Breath Res.* **5**, 024002 (2011).

[4] G.D. Banik, A. De, S. Som, S. Jana, S.B. Daschakraborty, S. Chaudhuri, and M. Pradhan. Hydrogen sulphide in exhaled breath: a potential biomarker for small intestinal bacterial overgrowth in IBS. *Journal of breath research* **10 (2)**, 026010 (2016).

[5] A. Maity, M. Pal, G. Datta Banik, S. Maithani, and M. Pradhan. Cavity ring-down spectroscopy using an EC-QCL operating at 7.5 μm for direct monitoring of methane isotopes in air. *Laser Physics Letters* **14(11)**, 115701(2017).

[6] S. Maithani, S. Mandal, A. Maity, M. Pal, and M. Pradhan. High-resolution spectral analysis of ammonia near 6.2 μm using a cw EC-QCL coupled with cavity ring-down spectroscopy. *Analyst* **143(9)**, 2109 (2018).

[7] H. Moser, W. Pölz, J. P. Waclawek, J. Ofner, and B. Lendl. Implementation of a quantum cascade laser-based gas sensor prototype

for sub-ppmv H2S measurements in a petrochemical process gas stream. *Anal Bioanal Chem* **409**, 729–739 (2017).

[8] M. Nikodem, K. Krzempek, D. Stachowiak, and G. Wysocki. Quantum cascade laser-based analyzer for hydrogen sulphide detection at sub-parts-per-million levels. *Opt. Eng.* **57(1)**, 011019 (2017).

[9] M. Siciliani de Cumis, S. Viciani, S. Borri, P. Patimisco, A. Sampaolo, G. Scamarcio, P. De Natale, F. D'Amato, and V. Spagnolo. Widely-tunable mid-infrared fiber-coupled quartz-enhanced photoacoustic sensor for environmental monitoring. *Optics Express* **22(23)**, 28222 (2014).

[10] M. Helman, H. Moser, A. Dudkowiak, and B. Lendl. Off‑beam quartz‑enhanced photoacoustic spectroscopy‑based sensor for hydrogen sulfide trace gas detection using a mode‑hop‑free external cavity quantum cascade laser. *Appl. Phys. B* **123**, 141(2017).

[11] H. Moser, A. Genner, J. Ofner, C. Schwarzer, G. Strasser, and B. Lendl. Application of a ring cavity surface emitting quantum cascade laser (RCSE-QCL) on the measurement of H2S in a CH4 matrix for process analytics. *Optics Express* **24(6)**, 6572 (2016).

[12] R. N. Zare, D. S. Kuramoto, C. Haase, S. M. Tan, E. R. Crosson, and N. M. R. Saad. High-precision optical measurements of 13C/12C isotope ratios in organic compounds at natural abundance. *PNAS* **106 (27)**, 10928 (2009).

[13] E. R. Crosson, K. N. Ricci, B. A. Richman, F. C. Chilese, T. G. Owano, R. A. Provencal, M. W. Todd, J. Glasser, A. A. Kachanov, B. A. Paldus , T. G. Spence , and R. N. Zare. Stable Isotope Ratios Using Cavity Ring-Down Spectroscopy: Determination of 13C/12C for Carbon Dioxide in Human Breath. *Anal. Chem.* **74 (9)**, 2003 (2002).

[14] R. Grilli, G. Mejean, S. Kassi, I. Ventrillard, C. Abd-Alrahman, and D. Romanini Frequency Comb Based Spectrometer for in Situ and Real Time Measurements of IO, BrO, NO2, and H2CO at pptv and ppqv Levels *Environ. Sci. Technol.* **46**, 10704 (2012).

[15] W. Chen, K. Roslund, C. L. Fogarty, P. J. Pussinen, L. Halonen, Per-Henrik Groop, M. Metsälä, and M. Lehto. Detection of hydrogen cyanide from oral anaerobes by cavity ring down spectroscopy. *Scientific Reports* **6**, 22577 (2016).

[16] J. Karhu, J. Nauta, M. Vainio, M. Metsälä, S. Hoekstra, and L. Halonen. Double resonant absorption measurement of acetylene symmetric vibrational states probed with cavity ring down spectroscopy. *The Journal of Chemical Physics* **144**, 244201 (2016).

[17] S. Das, A. Maity, M. Pradhan, and S. Jana. Assessing Atmospheric CO_2 Entrapped in Clay Nanotubes using Residual Gas Analyzer. *Anal. Chem.* **88 (4)**, 2205 (2016).

Chapter 6

Trace detection of nitrous oxide (N_2O) in gastric environment by QCL based CRDS technique

6.1 Introduction

Human exhaled breath contains quite high concentration of N_2O (typically 0.1-1.6 ppm) and tracking breath N_2O excretions is of medical significance [1-3]. However, the associated metabolic pathways of N_2O in human body are still largely unknown. It is noteworthy that the microbial denitrification which has been identified as the prime source of N_2O in atmosphere, is not usually considered relevant process in human-associated microbial inhabitants [4]. This is because microbial denitrification process is recognized to be occurred in an anaerobic condition in contrast to the aerobic environment of the gastrointestinal tract of human. However, Schreiber *et al.* [5] recently showed the possibility of the occurrence of microbial denitrification in the dental plaque of human under aerobic conditions. In microbial denitrification process, nitrate ion (NO_3^-) is reduced to gaseous N_2O via nitrite ion (NO_2^-) mediated by periplasmic and membrane-bound enzymes specific for each step. Studies in the past decade also revealed that NO_3^- is inherently synthesized in human body [6,7]. In addition, different kinds of denitrifying bacteria have already been identified and isolated from the gastrointestinal tract of human [3,4,8]. However, the aerobic denitrification by these denitrifying bacteria involving the generation of N_2O in the gastric environment has not yet been extensively studied. Therefore, an immense gap still remains to unveil the potential pathways leading to the formation of N_2O in human body. Very little information exists regarding microbial nitrification/denitrification in the aerobic

gastric environment which is important for understanding human physiology and health.

N_2O is also plausibly produced endogenously in human body from the reduction of L-arginine derived nitric oxide (NO) [9-11]. It has been previously reported that NO from the amino acid L-arginine is upregulated in response to gastric inflammation caused by the gastric pathogen *Helicobacter pylori* (*H. pylori*) infection [12-14]. Hence, exhaled breath N_2O may be a potential indicator of *H. pylori* induced inflammation in the gastric environment. Moreover, it is well-known that ammonium ion (NH_4^+) is generated from hydrolysis of urea due to the urease activity of *H. pylori* in the gastric environment. The NH_4^+ ion can possibly be nitrified in presence of nitrifying bacteria in gastric environment which eventually leads to the further generation of NO_2^- [1]. Therefore, it would be interesting to explore any potential nitrification of NH_4^+ generated in response to the urease activity of *H. pylori* infection in gastric environment. The study will further lead to the potential relation between exhaled N_2O and urease activity of *H. pylori* infection, which is still unclear.

In the present study, we, for the first time, simultaneously measured the dissolved N_2O concentration in gastric environment and exhaled breath N_2O exploiting an external cavity quantum cascade laser (EC-QCL) based cavity ring-down spectroscopy (CRDS) technique and subsequently we determined the NO_2^- concentration utilizing UV-Vis spectroscopy to provide better insight into the aerobic denitrification process in gastric environment. Thereafter, we elucidated the nitrification of NH_4^+ ion to form NO_2^- ion and subsequent denitrification of NO_2^- ion to produce N_2O in *in-vitro* chemical reaction between urea and urease in the gastric juice which has never been explored. Furthermore, we evaluated the *H. pylori* infected individuals to explore possible link between exhaled breath N_2O and the gastric pathogen. Finally, we investigated exhaled N_2O excretion dynamics in response to the urease activity of *H. pylori* infection to provide a new non-invasive and indirect assessment of the infection in human stomach.

Previous Knowledge	Key Hypothesis	Explored in the study	Conclusion
• Nitrification and denitrification are irrelevant processes in aerobic gastric environment. • The NO_2^- ion is the precursor of N_2O in the denitrification process. • NH_4^+ ion is produced in response to the urease activity of *H. pylori* infection in human stomach.	• Aerobic nitrification and denitrification are possible sources of N_2O in human body. • Nitrification of NH_4^+ ion in gastric juice is probably linked to exhaled N_2O.	• Measured the concentration of dissolved NO_2^- ion and N_2O in gastric juice, along with exhaled N_2O using spectroscopy techniques. • Investigated the nitrification of NH_4^+ ion and denitrification of NO_2^- in gastric juice. • Monitored the exhaled breath N_2O excretion dynamics for *H. pylori* infected patients.	• Our study provides the direct evidences of aerobic denitrification of NO_2^- ion in gastric juice. • NH_4^+ ion is nitrified to produce NO_2^- ion in the aerobic human gastrointestinal tract. • The potential link between urease activity of *H. pylori* infection and N_2O concentration in exhaled breath has been established.

Figure 6.1 *A brief outline of the present study.*

The present investigation deepens our understanding of the microbial nitrification and denitrification processes in gastric environment which were believed to be insignificant phenomena over the past decades. In a nutshell, a pictorial description of the present study has been illustrated in the figure (Fig. 6.1).

6.2 Materials and Methods

6.2.1 EC-QCL coupled cavity ring-down spectroscopy (CRDS)

A lab-based CRDS spectrometer combined with an EC-QCL was employed in the present study to determine N_2O concentration and it is shown schematically in figure 6.2(a). The technical details of the CRDS method have been described elaborately in our previous work [16]. In brief, a room-temperature external cavity quantum cascade laser (EC-QCL) with mode-hop-free (MHF) tuning range of 1257-1341 cm^{-1} was utilized as an optical source. Two high reflective (R≥99.98% at 7.8 μm) plano-concave mirrors with radius of curvature 1 metre were precisely

aligned at the two ends of a 50 cm quartz-coated gas cell to form a stable high-finesse optical cavity. Three piezo-electric-transducers (PZT) were attached to one of the mirror-mounts to modulate the length of the cavity for mode-matching between cavity-mode and laser-mode which eventually trapped the laser light inside the cavity. The optical signal was ultimately detected using a four-stage thermoelectrically cooled photovoltaic mercury-cadmium-telluride (MCT) detector. An acoustic-optic modulator (AOM) was further employed to cut-off the laser light after the pre-selected threshold value, thus allowing ring-down events to occur. The typical ring-down traces for our set-up at presence and absence of a gas sample were shown in figure 6.2(b). The real-time monitoring of laser wavelength was achieved using a wavemeter whereas a 14-bit, high speed digitizer (100 MS s^{-1}) was utilized to acquire data to be finally analyzed by a custom build lab-view programme. The absorption spectra of a sample which was obtained by plotting ring-down decay rate (k) against wavenumber (cm^{-1}) was fitted with the Voigt function and the area of the fitted spectra was utilized to determine the sample concentration.

6.2.2 Selection of absorption line

To measure N_2O concentration, we probed the rotational R(27) line of N_2O centred at 1306.929 cm^{-1} arising from the ro-vibrational transition, (0000)-(1000). There were two main reasons for selecting this transition i.e.: (i) this selected line belongs to the fundamental vibrational band of N_2O at 7.65 μm with a large absorption cross-section of 1.04 x 10^{-19} cm^{-1} molecule^{-1} cm^2 [20], and (ii) the probed line is free from interferences of different abundant molecular species such as CO_2, H_2O and CH_4 (Fig. 6.2(c)). Hence, the selected absorption feature of N_2O inherently facilitates the high sensitivity and molecular selectivity in the measurements. The figure 6.2(d) depicts the absorption spectra of N_2O with three different standard concentrations.
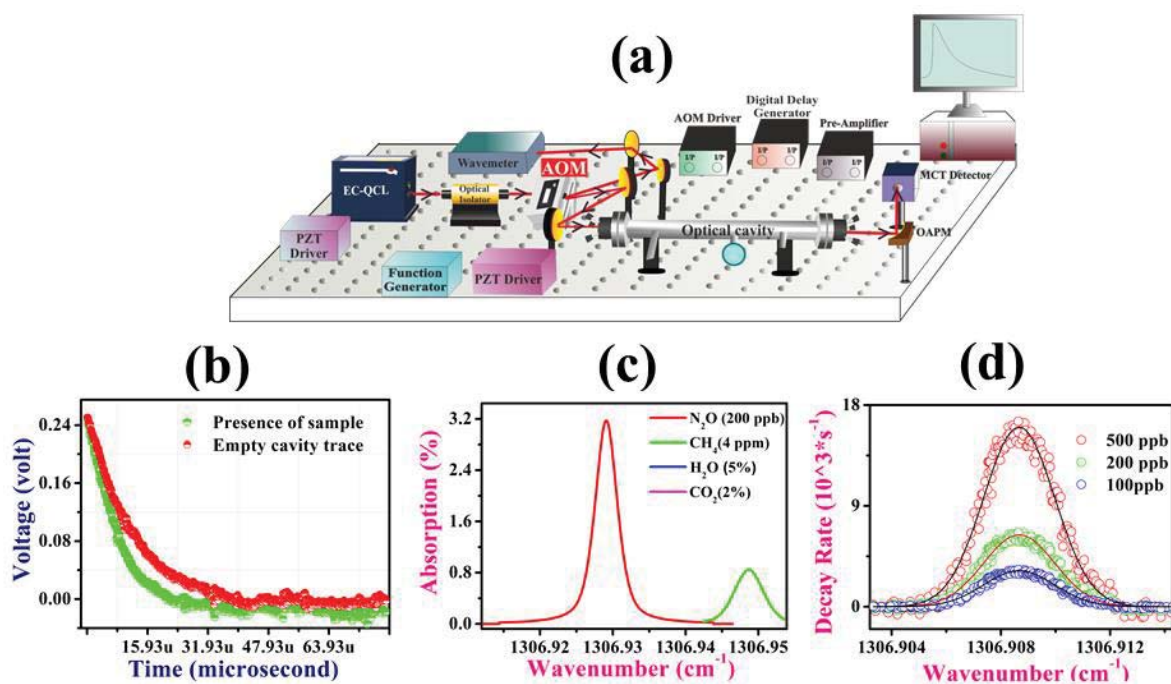
Fig. 6.2 *Performance characteristics of the cw-EC-QCL coupled CRDS spectroscopy technique developed in lab. (a) A schematic diagram of the cw EC-QCL based CRDS set-up. (b) A typical ring-down trace with and without sample inside the optical cavity. (c) HITRAN simulation for absorption spectra of N_2O (200 ppb) centred at ~1306.929 cm^{-1} demonstrating interference-free feature from three major abundant molecular species of H_2O (5%), CO_2 (2%), and CH_4 (4 ppm) at the experimental conditions of ~4 km pathlength, 8 Torr pressure and 296K temperature. (d) A ring-down spectra for the different concentrations of N_2O centred at ~1306.929 cm^{-1} representing the variation of decay-rate (s^{-1}) with the change of wavenumber (cm^{-1}).*

6.2.3 Subject selection criterion

After the initial routine check-up, one hundred nine individuals (average age of 36±14 years) with different gastrointestinal disorders like gastritis, non-ulcer dyspepsia, and peptic ulcer were enrolled in our study. We made two groups of enrolled individuals by categorizing them as *H. pylori* positive (n = 60) and *H. pylori* negative (n = 49) based on the reports of both "gold-standard" tests i.e. endoscopy, biopsy-based rapid urease test (RUT) and ^{13}C-urea breath test (^{13}C-UBT). In ^{13}C-UBT, individuals were diagnosed as *H. pylori* positive if δ_{DOB}[13]C (‰) ≥ 3 ‰ at 30 min [21-23]. Patients, who were undergoing antibiotics treatment, receiving proton-pump inhibitors or H_2 receptor antagonists four weeks

prior to the study, were excluded from the study. The Ethics Committee Review Board of AMRI Hospital, Salt Lake, Kolkata, India, approved the protocol of the current study (Study no.: AMRI/ETHICS/2013/1). The administration of S. N. Bose Centre, Kolkata, India, also provided permission for the current study (Ref. no.: SNB/PER-2-6001/13-14/1769). The written consent was taken from each individual prior to the study.

6.2.4 Collection of gastric juice

Gastric juice from each subject was aspirated through the suction channel of the endoscope and kept in airtight mucus extractor [23]. Next, the gastric juice was immediately kept under −20°C to maintain the stability of the protein. Thereafter, gastric juice samples were centrifuged at 10,000 rpm for eliminating the mucus before analysis in CRDS and UV-Vis spectroscopy.

6.2.5 Breath sample collection

An empty stomach breath sample was collected in a breath bag (QUINTRON, USA, SL No.QT00892) from individual patient prior to endoscopic procedure. Thereafter, patients were prescribed for ^{13}C-UBT in the next day of the endoscopic procedure. Before the breath test, all patients were instructed to wash their mouth repeatedly to avoid any kind of contribution from oral cavity bacteria. In standard ^{13}C-UBT protocol, a baseline breath sample was collected after 10 min following ingestion of 4 g citric acid dissolved in 200 mL of water. Next, a test meal containing 75 mg ^{13}C-labeled urea (CLM-311-GMP, Cambridge Isotopic Laboratories, Inc., USA) dissolved in 50 mL of water was administered to the patient and subsequently, breath samples were taken from the patients up to 45 minutes at 15 minutes interval. We also collected breath samples prior to the citric acid ingestion from the patients for our experiment purposes. The N_2O concentration of all the breath samples was measured by EC-QCL based CRDS technique developed in our laboratory.

6.2.6 Preparations of chemical solutions

The jack bean urease was purchased from Sigma Aldrich (Sigma Aldrich; EC 3.5.1.5). The 5 μM urease solution was prepared in deionized (DI) water. The DI water was utilized to remove the potential effect of impurity ions in the chemical reaction. Similarly, we prepared the standard urea solution of 20 mM in DI water. Urea was purchased from Sisco Research Laboratories Pvt. Ltd (SRL) with highest purity. The ^{13}C-enriched urea ($\geq$99% ^{13}C) for ^{13}C-urea breath test was purchased from Cambridge Isotope Laboratories, Inc. We purchased Griess Reagent Kit (G-7921) from ThermoFisher to measure the NO_2^- concentration in solution. This kit contains N-(1-naphthyl) ethylenediamine, Sulfanilic acid and standard Nitrite solution. We prepared all the solutions as per the ThermoFisher scientific instruction guide to measure the NO_2^- ion concentration. The pH measurements of different samples were made utilizing a standard pH meter (ecphtutor-ds).

6.2.7 Measurement of dissolved N$_2$O in gastric juice by CRDS

To measure the dissolved N_2O concentration in gastric juice, we utilized headspace extraction technique [15] where certain amount of gastric juice was injected into a pre-vacuumed sealed container. The dissolved N_2O came out into the blank headspace, which was collected and subsequently measured by the CRDS method. We employed the same methodology to monitor the N_2O concentration in gastric juice in response to the externally added urease-urea.

6.2.8 Estimation of nitrite (NO$_2^-$) ion in gastric juice

Griess reagent is generally used for determination of nitrite ion (NO_2^-) concentration in a solution. It consists of Sulfanilic acid and *N*-(1-naphthyl) ethylenediamine. The Sulfanilic acid is converted to a diazonium salt in reaction with the NO_2^- ion in solution. The diazonium salt is subsequently coupled to *N*-(1-naphthyl) ethylenediamine to form an azo dye that can be spectrophotometrically quantified based on its absorbance at 548 nm. The protocol consisted of 300μL of the gastric juice placed in 1 cm spectrometric cell containing 100μL of Griess reagent to measure the absolute concentration of NO_2^- ion. In contrast, an amount of

2.6 mL urea-urease standard solution in deionized water was added into the mixture of 300µL gastric juice and 100µL Griess reagent to monitor the kinetics of the formation of NO_2^- ion in response to the urea-urease reaction. The absorbance was measured by a UV-Vis spectrophotometer (Shimadzu UV-2600 Spectrophotometer).

6.3 Results and Discussion

6.3.1 Measurement of dissolved N_2O and NO_2^- concentration in gastric juice

We first evaluated the dissolved N_2O concentration in gastric juice collected through endoscopic suction channel from patients (n=109) with various gastrointestinal disorders utilizing headspace extraction technique [15]. Subsequently, we measured its concentration by the EC-QCL coupled with cavity ring-down spectroscopy (CRDS) [16]. We also simultaneously monitored the empty stomach exhaled breath concentration of N_2O exploiting the same CRDS technique.
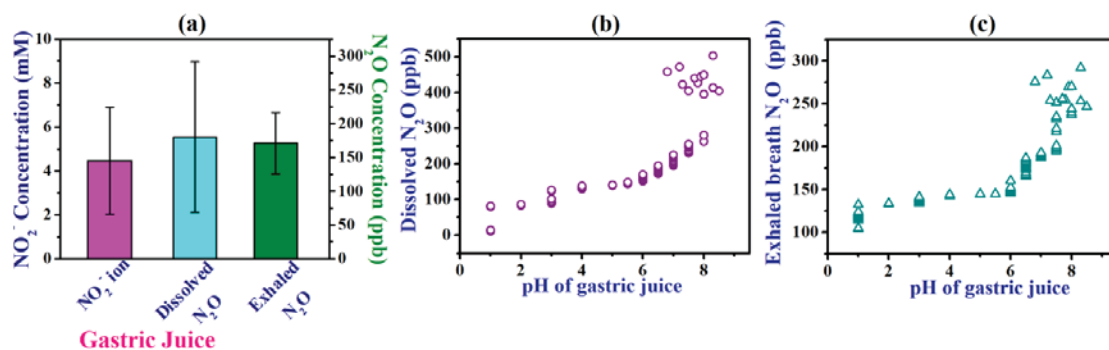
Fig. 6.3 *Spectroscopic studies of human gastric juice. (a) Quantitative estimation of dissolved concentrations of NO_2^- ion (4.46 ± 2.43 mM) and N_2O molecule (180.03 ± 111.48 ppb) in human gastric juice in comparison to the exhaled N_2O concentrations (171.04 ± 45.44 ppb). (b) and (c) Variations of dissolved N_2O concentration in gastric juice and exhaled N_2O concentration, respectively with the pH of gastric juice. Error bars denote the standard deviation (1sd).*

We employed the UV-Vis spectroscopy to measure NO_2^- ion concentration in the gastric juice monitoring the formation of azo dye in the Griess reaction [17]. It is evident from the figure 6.3(a) that N_2O

concentration both in gastric environment and exhaled breath are almost identical. In contrast, the NO_2^- ion concentration in gastric juice was measured to be 4.46 ± 2.43 mM. It is noteworthy to mention that we did not find any measureable NO_2^- ion concentration in gastric juice for about 81% individuals. Furthermore, we did not observe any direct correlation between pH of the gastric juice and N_2O concentrations in both gastric juice and exhaled breath. But, we specifically noticed that dissolved N_2O concentration in gastric juice and N_2O concentration in exhaled breath were quiet high for the individuals with high gastric pH (Fig. 6.3(b) and 6.3(c)). However, it is well established that high pH environment is more favourable to the denitrifying bacteria [3]. Taken together, these findings suggest that NO_2^- ion, in presence of denitrifying bacteria, is preferably converted into N_2O in gastric environment which in turn is transported through blood stream and finally it is excreted in exhaled breath.
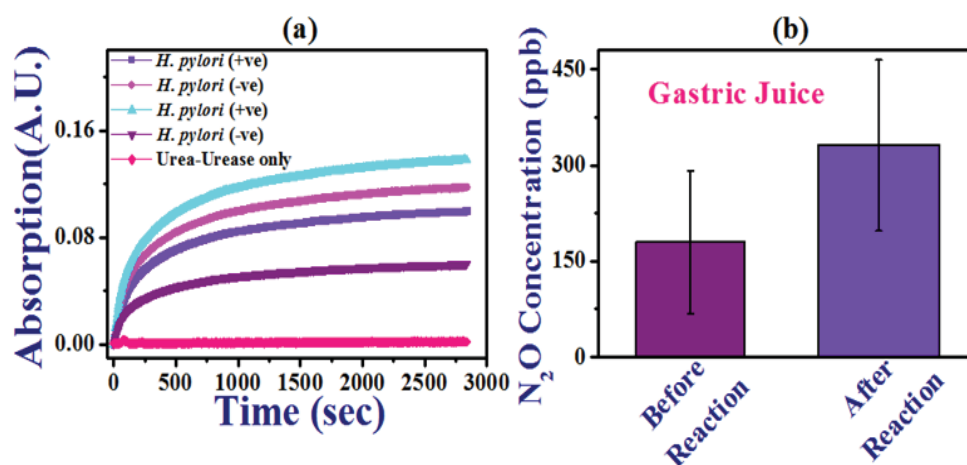
Fig. 6.4 *Spectroscopic investigations of in-vitro chemical reactions in human gastric juice. (a) Illustration of time dynamics of NO_2^- ion formation in gastric juice in presence of external urease (5 μM) and urea (20 mM) exploiting Griess reaction for two (2) H. pylori positive and H. pylori negative individuals. The result was compared to the Griess reaction performed in absence of the gastric juice medium. (b) The dissolved N_2O concentrations before (180.03 ±111.48 ppb) and after (331.38 ± 133.6ppb) the reaction of urease (5 μM) and urea (20 mM) in the gastric juice medium. Error bars denote the standard deviation (1sd). Arbitrary Unit is abbreviated as A.U.*

Hence, the absence of NO_2^- ion in gastric juice of most individuals can potentially be linked to the generation of N_2O dissolved in individual's gastric juice and thus unveiling the missing link between NO_2^- ion in gastric environment and N_2O concentration in exhaled breath of individuals.

6.3.2 Exhaled breath N_2O concentration measurement using CRDS

Next, we explored the potential aerobic nitrification of NH_4^+ ion in gastric environment. It is well known that NH_4^+ ion is produced in urease-urea reaction. Therefore, to confirm the possibility of aerobic nitrification of NH_4^+ ion in the gastric environment we monitored the *in-vitro* chemical reaction of urease-urea in gastric juice. We studied the kinetics of NO_2^- ion formation in the reaction medium utilizing the Griess reaction and the results have been depicted in Fig. 6.4a and 6.4b. In this experiment, we observed an increase of absorption at 548 nm (Fig. 6.4(a)) which eventually indicates the formation of NO_2^- ion in the gastric juice medium, whereas no such change in absorption was found for urease-urea reaction without gastric juice. Subsequently, we measured the dissolved N_2O concentration in the medium of gastric juice in response to the urease-urea reaction employing the high precision CRDS technique. We noticed an increase of N_2O concentration from the initial dissolved concentration of N_2O in response to the urease-urea reaction in the gastric fluid medium (Fig. 6.4(b)). In view of these, our study confirmed the possibility of nitrification of NH_4^+ ion to produce NO_2^- ion followed by denitrification of NO_2^- ion leading to the formation of N_2O in the gastric environment. Consequently, we have provided the experimental evidences of nitrification and denitrification processes along with a new pathway of N_2O generation in human body which have significant relevance to human health.

It is well known that *H. pylori* infection that causes inflammation and ulcer in human stomach also produces NH_4^+ ion owing to its urease activity. Therefore, in our study we categorized all the enrolled individuals into two groups i.e. *H. pylori* infected and *H. pylori* non-

infected controls to gain better insight into the relationship between *H. pylori* infection and N_2O production. We found that dissolved N_2O concentration in gastric juice was significantly higher (p<0.001) for *H. pylori* infected individuals in comparison to the *H. pylori* negative individuals (Fig. 6.5(a)). This result may possibly be attributed to the fact that the generation of additional NH_4^+ ion in presence of *H. pylori* infection causes the production of greater amount of N_2O dissolved in the gastric juice. However, we did not observe any significant difference (p>0.05) of empty stomach breath N_2O concentration between *H. pylori* infected and *H. pylori* negative individuals (Fig. 6.5(a)). This observation indicates that there might be some other factors which eventually control the transportation of N_2O from gastric environment to the exhaled breath, and the importance of this observation demands further studies to explore those factors.
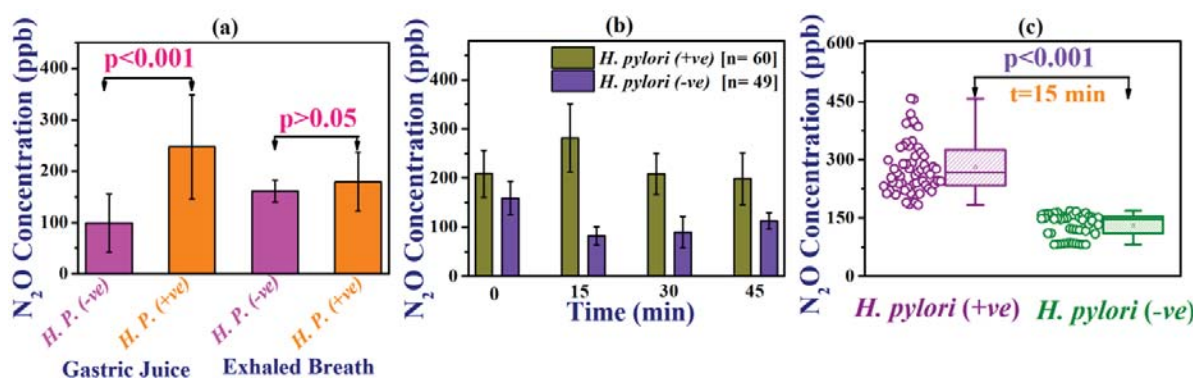
Fig. 6.5 *Variation of N_2O concentrations in human gastrointestinal tract in presence of human pathogen H. pylori.* *(a) A statistically significant (p<0.001) difference of dissolved N_2O concentration in gastric juice was observed between H. pylori positive (246.96 ±101.35 ppb) and H. pylori negative (99.46 ±56.21 ppb) individuals. In contrast, empty stomach exhaled N_2O concentration was found to be statistically insignificant (p>0.05) between H. pylori positive (179.24 ±57.16 ppb) and H. pylori negative (161 ±21.05 ppb) individuals. (b) The excretion kinetics of exhaled N_2O concentration in response to the ^{13}C-urea breath test (^{13}C-UBT) was depicted for H. pylori positive and H. pylori negative individuals. (c) A Box-Whisker plot demonstrating a significant difference (p<0.001) in the statistical distribution of exhaled N_2O concentration at 15 minutes for H. pylori positive (281.57 ± 69.10 ppb) and H. pylori negative*

(131.26 ± 30.03ppb) individuals during ^{13}C-UBT. Error bars denote the standard deviation (1sd).

Next, we monitored the time dynamics of N_2O concentration in exhaled breath for *H. pylori* infected and *H. pylori* negative individuals in response to the external urea which was administered during the urea breath test (UBT) (Fig. 6.5(b)). The aim was to counter verify whether the aerobic nitrification of NH_4^+ ion followed by denitrification of NO_2^- ion is ultimately producing N_2O under *in-vivo* physiological conditions. However, since *H. pylori* infection produces NH_4^+ ion in response to the external urea, the NH_4^+ ion would be first nitrified to generate NO_2^- and subsequently denitrified to produce N_2O which is in turn transported to the lungs where it is excreted in exhaled breath. We found (Fig. 6.5(b)) that in case of *H. pylori* infected individuals exhaled N_2O concentration gradually increased up to 30 minutes and then slowly decreased to its initial value in response to the administered urea. The observation is likely to be the effect of the generation of higher amount of NH_4^+ in the initial stage of urea hydrolysis which prompts the larger production of N_2O. This is eventually reflected in the increase of exhaled N_2O concentration in the initial phase of the excretion dynamics. In contrast, we did not observe any significant change of exhaled N_2O concentration for *H. pylori* negative individuals. The most significant difference ($p<0.001$) of exhaled N_2O concentration between *H. pylori* infected and *H. pylori* negative individuals was found to be at 15 minutes in response to the administered urea (Fig. 6.5(c)). Hence, *in vivo* physiological processes followed the *in vitro* experimental results quite well and thus the findings are opening another novel non-invasive strategy for the diagnosis of *H. pylori* infection in human stomach. It is noteworthy to mention that several studies in the past reported exhaled NO as a possible non-invasive marker for *H. pylori* infection. But, the concentration of NO in exhaled breath is highly affected due to the exhalation flow-rate and presence of asthma condition [18]. Taken together, our findings suggest that tracking exhaled N_2O would be more robust and better alternative to NO monitoring and thus might be considered as a potential marker for non-invasive diagnosis of *H. pylori* infection.
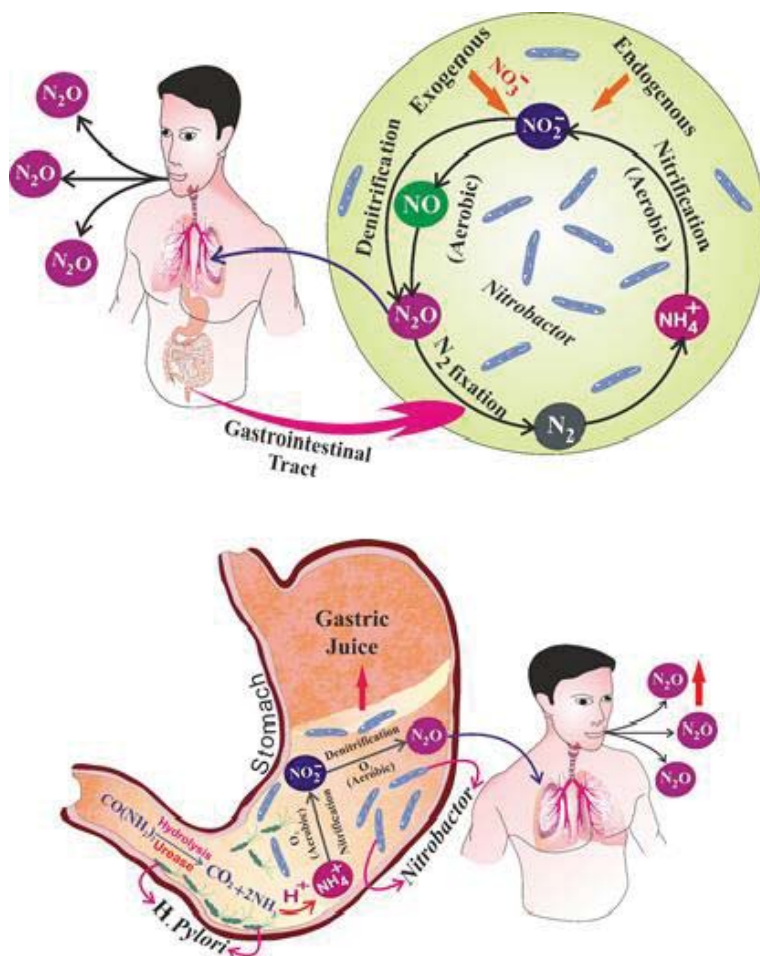
Fig. 6.6 *Potential metabolic pathways of N_2O formation in human gastrointestinal tract. The aerobic denitrification of NO_2^- ion contributes to the N_2O cycle existing in the human gastrointestinal tract. In addition, NH_4^+ ion is also found to produce NO_2^- ion through aerobic nitrification process, and subsequently links to the cycle of N_2O formation. For the specific condition of H. pylori infection, the formation of NH_4^+ ion is enhanced to facilitate the acid resistance in presence of external urea under the acidic condition of stomach, which in turn enhances the exhaled N_2O concentration of the infected individuals.*

6.3.3 Exploration of possible pathway

Finally, in the view of our experimental results we elucidated the potential metabolic pathways of N_2O formation in human gastrointestinal tract (Fig. 6.6). The endogenous NO_2^- ion, along with the exogenous contributions involving vegetables and drinking water [2], is denitrified to produce N_2O through the process of bacterial metabolism under

aerobic conditions in the human gastrointestinal tract. Thereafter a part of the bacterial metabolite N_2O remains dissolved into the gastrointestinal fluid, whereas the remaining part is transported through blood stream and finally excreted in exhaled breath. In addition to the direct denitrification of NO_2^- ion present in the gastrointestinal tract, the aerobic nitrification of NH_4^+ ion has further been revealed to contribute to the formation of NO_2^- ion which is subsequently denitrified to produce N_2O in the human gastrointestinal tract. Furthermore, the metabolic processes of nitrification of NH_4^+ ion to form NO_2^- ion and subsequent denitrification of NO_2^- ion to form N_2O in the human-associated microbial community residing at the aerobic gastrointestinal tract have been confirmed under the *in-vivo* physiological conditions exploiting the acid-acclimation process [19] of gastric pathogen *H. pylori* in the presence of external urea. In the acidic environment of human stomach, *H. pylori* secretes urease enzyme to facilitate acid resistance producing NH_4^+ ion in the process of hydrolysis of external urea, and thus in turn it eventually enhances the exhaled N_2O concentration of the infected individuals. In other words, this process contributes to the existing sequence of nitrification and denitrification processes leading to the generation of N_2O in the human gastrointestinal tract.

6.4 Conclusions

In conclusion, our findings explored the potential pathways of exhaled N_2O in human body providing the direct experimental evidence of aerobic denitrification of NO_2^- ion which is the precursor of N_2O, in gastric environment. We have also taken a step towards unravelling the underlying mechanism of nitrification of NH_4^+ ion followed by denitrification of NO_2^- ion in the aerobic gastric environment. Furthermore, our findings also revealed a fundamental mechanism under *in-vivo* physiological conditions exploiting the urease activity of *H. pylori* infection, which in turn also indicates the potential link between *H. pylori* infection and N_2O concentration in exhaled breath. Thus the present study may open a new perspective for better understanding of the different mechanisms of N_2O involving human body along with the potential medical significance of monitoring exhaled breath N_2O.

Although some imperative gaps may remain in our current understanding, however, the present findings are fostering exploration of microbial nitrification and denitrification phenomena in human-associated microbial community with physiological and pathological relevance.

6.5 References

[1] Lundberg J O., Weitzberg E., Cole J. A., and Benjamin N. Nitrate, bacteria and human health *Nature Rev. Microbiol.* 2004;2:593-602.

[2] Forman D., Al-Dabbagh S., and Doll R. Nitrates, nitrites and gastric cancer in Great Britain." *Nature* 1985;313:620-5.

[3] Mitsui T., Kato N., Shimaoka K., and Miyamura M. Effect of aging on the concentrations of nitrous oxide in exhaled air *Sci Total Environ.* 1997;208:133-7.

[4] Tiso M., Schechter A. N. Nitrate Reduction to Nitrite, Nitric Oxide and Ammonia by Gut Bacteria under Physiological Conditions *PLoS ONE* 2015;10(3):e0119712. doi:10.1371/journal.pone.0119712.

[5] Schreiber F., Peter Stief P., Gieseke A., Heisterkamp I. M., Verstraete W., Beer D. de, and Stoodley P. (2010) Denitrification in human dental plaque. *BMC Biology* 2010;8:24.

[6] Green L. C., Tannenbaum S. R., and Goldman P. Nitrate synthesis in the germfree and conventional rat. *Science* 1981;212:56-8.

[7] Witter J. P., Gatley S. J., and Balish E. Evaluation of nitrate synthesis by intestinal microorganisms in vivo *Science* 1981;213:449-50.

[8] Gomez R. F., Tannenbaum S. R., Savoca J., Ralt D., and Rockowitz N. Heterotrophic nitrification by intestinal microorganisms *Cancer* 1980; 45:1066-7.

[9] Palmer R. M. J., Ferrige A. G., and Moncoda S Nitric oxide release accounts for the biological activity of endothelium-derived relaxing factor. *Nature* 1987;327:524-6.

[10] Ignarro L. J., Fukuto J. M., Griscavage J. M., Rogers N. E., and Byrns R. E Oxidation of nitric oxide in aqueous solution to nitrite but not nitrate: Comparison with enzymatically formed nitric oxide from L-arginine. *Proc. Natl. Acad. Sci. USA* 1993;90:8103-7.

[11] Bryan N. S., and Grisham M. B Methods to Detect Nitric Oxide and its Metabolites in Biological Samples. *Free Radic Biol Med.* 2007;43(5): 645-57.

[12] Antos D., Enders G., Rieder G., Stolte M., Bayerdörffer E., and Hatz R. A. Inducible nitric oxide synthase expression before and after eradication of Helicobacter pylori in different forms of gastritis. *FEMS Immunol. Med. Microbiol.* 2001;30:127-31.

[13] Wilson K. T., Ramanujam K. S., Mobley H. L., Musselman R. F., James S. P., and Meltzer S. J. *Helicobacter pylori* stimulates inducible nitric oxide synthase expression and activity in a murine macrophage cell line. *Gastroenterology* 1996;111:1524-33.

[14] Som S., Dutta Banik G., Maity A., Chaudhuri S., and Pradhan M. Exhaled nitric oxide as a potential marker for detecting non-ulcer dyspepsia and peptic ulcer disease. *J. Breath Res.* 2018;12:026005. doi. https://doi.org/10.1088/1752-7163/aa8efb

[15] Hinshaw S. E., and Dahlgren R. A. Dissolved Nitrous Oxide Concentrations and Fluxes from the Eutrophic San Joaquin River, California. *Environ. Sci. Technol.* 2013;47:1313-22.

[16] Maity A., Pal M., Datta Banik G., Maithani S., and Pradhan M. Cavity ring-down spectroscopy using an EC-QCL operating at 7.5 µm for direct monitoring of methane isotopes in air. *Laser Physics Letters* 2017;14(11):115701. doi: https://doi.org/10.1088/1612-202X/aa8584.

[17] Sun J., Zhang X., Broderick M., and Fein H. Review: Measurement of Nitric Oxide Production in Biological Systems by Using Griess Reaction Assay. *Sensors* 2003; 3:276-84.

[18] Dweik R. A., Boggs P. B., Erzurum S. C., Irvin C. G., Leigh M. W., Lundberg J. O., Olin A. C., Plummer A. L., and Taylor D. R. An official ATS clinical practice guideline: interpretation of exhaled nitric oxide levels (FENO) for clinical applications. *Am. J. Respir. Crit. Care Med.* 2011;184:602-15.

[19] Sachs G., Weeks D. L., Wen Y., Marcus E. A., Scott D. R., and Melchers K. Acid acclimation by *Helicobacter pylori*. *Physiology* 2005;20:429-38.

[20] Rothman L., Gordon I., Babikov Y., Barbe A., Benner D. Chris, Bernath P., Birk M., Bizzocchi L., Boudon V., Browni L. R., Campargue A., Chance K., Cohen E. A., Coudert L. H., Devi V. M., Drouin B. J., Fayt A., Flaud J. M., Tyuterev G., and Wagner G. The HITRAN 2012 molecular spectroscopic database. *J Quant Spectrosc Radiat Transf*. 2013;130:4.

[21] Gisbert J. P., and Pajares J. M. Review article: 13C-urea breath test in the diagnosis of *Helicobacter pylori* infection-a critical review. *Aliment Pharmacol Ther*. 2004;20:1001-17.

[22] Maity A., Banik G. D., Ghosh C., Som S., Chaudhuri S., Daschakraborty S. B., *et al.* Residual gas analyzer mass spectrometry for human breath analysis: a new tool for the non-invasive diagnosis of Helicobacter pylori infection. *J Breath Res*. 2014;8(1):016005. doi: 10.1088/1752-7155/8/1/016005.

[23] Maity A., Pal M., Som S., Maithani S., Chaudhuri S., and Pradhan M. Natural ^{18}O and ^{13}C-urea in gastric juice: a new route for non-invasive detection of ulcers. *Anal Bioanal Chem*. 2017;409(1):193-200. doi: 10.1007/s00216-016-9985-y.

Chapter 7

Cavity ring-down spectroscopic investigation of allowed $(\nu_4+\nu_5)^0$ and forbidden $(\nu_4+\nu_5)^2$ bands of Acetylene near 7.5 μm using Quantum Cascade Laser

7.1 Introduction

Acetylene (C_2H_2) is considered to be the simplest example of prototype carbon-carbon triple bond hydrocarbon in the alkyne homologous series [1]. This non-methane volatile organic compound (VOC) is a trace constituent of both terrestrial troposphere and urban atmosphere due to its almost exclusive anthropogenic sources [2-3]. Acetylene has also an immense importance in astrophysical society because this molecule has been detected in the atmospheres of Saturn, Titan and Jupiter [4-6]. It has been also observed in many carbon-rich stars and interstellar medium in the spectral region around 1300 cm^{-1} [7]. However, the spectral features of C_2H_2 has been the subject of considerable spectroscopic investigation because it exhibits numerous ro-vibrational bands throughout the IR spectrum and vibrational levels are grouped into clusters or polyads with a regular spacing of about 700 cm^{-1} from mid-IR to the visible region. Acetylene is a linear tetra atomic hydrocarbon which is characterized by five normal modes of vibration (ν_1, ν_2, ν_3, ν_4, ν_5) in which ν_1, ν_2 and ν_3 represent the symmetric stretching of CH bond (Σ_g^+, ν_1 = 3372.8 cm^{-1}), CC bond (Σ_g^+, ν_2 = 1974.3 cm^{-1}) and antisymmetric stretching of CH bond (Σ_u^+, ν_3 = 3294.8 cm^{-1}), whereas ν_4

and ν_5 signify the doubly degenerate *trans*-Π_g ($\nu_4 = 612.87$ cm^{-1}) and *cis*-Π_u ($\nu_5 = 730.33$ cm^{-1}) bending vibrations, respectively. Over the past decades numerous theoretical and experimental spectroscopic studies on C_2H_2 have extensively been carried out in order to obtain line positions and line intensities of several vibrational bands in various spectral regions [8-13]. However, high-resolution and high-precision spectroscopic measurements of C_2H_2 near 7.5 μm in the mid-IR region are still limited and remained largely unexplored. The 7.5 μm spectral region under study is of great interest because this region consists of $(\nu_4+\nu_5)^0$ combination band involving the simultaneous excitation of the *trans*-ν_4 and *cis*-ν_5 bending modes of C_2H_2 and this allowed band corresponds to the transitions from the ground vibrational level. This combination band has a large impact in astrophysics because C_2H_2 was detected at 7.5 μm region in the spectrum of the circumstellar envelopes of carbon-rich stars by means of Infrared Spectrograph (IRS) [7]. Therefore the measurements of the absolute line intensities and line positions in $(\nu_4+\nu_5)^0$ of C_2H_2 near 7.5 μm are the subject of great interest for high-resolution spectroscopy studies. But, high-precision spectroscopic measurement of this allowed combination band at 7.5 μm is extremely challenging because it suffers from the several "hot bands" contamination. The measurements are further hindered by the presence of the overlapping $(\nu_4 + \nu_5)^2$ "forbidden" band in this spectral region. Moreover, this forbidden transition can affect the intensity of parallel type $(\nu_4+\nu_5)^0$ band through *l*-type resonances by borrowing intensity from this allowed transition. This *l*-type resonance arises due to Coriolis interaction between doubly degenerated bending modes in a linear molecule like C_2H_2 and causes a significant modification of *J*-dependencies of the line intensities leading to so-called Herman-Wallis effects [9]. In addition, the effects of pressure of bath gases like N_2, O_2 *etc.* on the spectral features are very much essential for atmospheric and astrophysical applications and such important investigations on both $(\nu_4+\nu_5)^0$ and $(\nu_4+\nu_5)^2$ bands in the spectral region near 7.5 μm remain largely unexplored. Therefore a comprehensive understanding of the spectral parameters such as individual line intensities, pressure broadening coefficients, transition dipole moments along with Herman-

Wallis coefficients would help to retrieve C_2H_2 concentration from the spectra of astrophysical objects or atmospheric spectra. Moreover, the detailed quantitative analysis of the spectral parameters in two bands of C_2H_2 around 7.5 μm will be useful to improve the global theoretical model developed in recent times for C_2H_2 [9-10,14].

However, early studies employed several spectroscopic techniques such as Fourier transform spectroscopy (FTS), Dual comb spectroscopy (DCS), Differential absorption spectroscopy (DAS) and Cavity-rind down spectroscopy (CRDS) with near-IR diode lasers for spectroscopic measurements of C_2H_2 at various spectral regions [14-16]. But the exploitation of a *cw* mode-hop-free (MHF) external-cavity quantum cascade laser (EC-QCL) coupled with highly-sensitive optical cavity-enhanced absorption techniques such as CRDS has not yet been reported for the high-resolution (~0.0003cm^{-1}) and high-precision ro-vibrational measurements of both $(\nu_4+\nu_5)^0$ and $(\nu_4+\nu_5)^2$ combination bands of C_2H_2 near 7.5 μm region. The findings utilizing EC-QCL based CRDS technique presented here are combined with the results of earlier FTS studies as well as HITRAN database [9, 14, 17]. The new data will be useful for better fundamental understanding of the allowed and forbidden combination bands of linear tetra atomic molecules.

In this study, we have recorded the high-resolution CRDS spectra of selected individual rotational lines in both P-branch and R-branches of C_2H_2 belonging to transition of $(\nu_4+\nu_5)^0$ and $(\nu_4+\nu_5)^2$ that are located in the 7.5 μm region. We measured the absolute line intensities of 16 lines from P-branch and 4 lines from R-branch of $(\nu_4+\nu_5)^0$ band. The line intensities (i.e., line-integrated absorption cross-section) have been derived by acquiring high-resolution CRDS spectra of known partial pressures of C_2H_2 under the conditions of low overall pressure in a high-finesse optical cavity. For the pressure broadening study, CRDS spectra of C_2H_2 have been recorded at various air pressures up to 110 Torr and the spectra exhibited substantial pressure broadening effects. Subsequently, we demonstrated rotational level-dependant pressure broadening coefficients. We also measured the absolute positions and line intensities of few lines of P-branch of the $(\nu_4+\nu_5)^2$ forbidden band. Line-broadening

parameters were also determined for this transition by using N_2 as a broadening gas. The vibrational transition dipole moments and empirical Herman-Wallis coefficients were also studied quantitatively in the present study.

7.2 Experimental section

The external-cavity QCL based continuous wave cavity ring-down spectrometer has been used in this study for recording all acetylene spectra at 7.5 μm. The details of the spectrometer was described elaborately elsewhere [18]. The spectrometer was devoted early in line-strength measurement of methane isotopes [18], monitoring of natural abundances of sulphur isotopes of H_2S [19] and Nitrous oxide measurement for biological application [20]. In a brief description, a water cooled continuous wave external cavity quantum cascade laser (MHF-41078; Daylight Solutions, USA), having very narrow line width (<0.0003 cm^{-1}), with mode-hop-free tuning range (1341 cm^{-1}–1257 cm^{-1}) was deployed here as a laser source. The laser was then coupled with help of gold coated bending mirrors to quartz coated stainless steel high-finesse optical cavity of 50 cm length, comprising with two high-reflective super mirror (CRD Optics Inc.;USA) with reflectivity R > 99.98% at 7.35 μm. Before entering into the cavity, laser beam was passed through optical isolator (FIO-5-7.8; Innovation Photonics) and Acousto-optic modulator (AOM) (AOM; AGM406B11M; IntraAction Corp; USA). AOM helped to diffract the beam in two direction, one of the beam went to wave-meter (621B-MIR; Bristol Instruments) for monitoring the high-resolution wavenumber and other beam went to the central axis of cavity ring down cell for full-filling the mode matching criterion. Now to achieve mode matching phenomena between fundamental transverse modes inside the CRD cell and laser beam, one mirror of the gas cell, mounted on a piezo-electric transducer (PZT, Thorlabs PE4), was modulated with 50 Hz frequency for sweeping the cavity mode frequency over one free spectral range. Then the AOM was used for quick and efficient termination of laser beam with help of pulse-delay generator (DG645; Stanford Research Systems) to achieve concentration dependant decay event of intra-cavity light, which was focused on mid-infrared detector (PVI-4TE-8-1X1; Vigo

System S.A.) by gold-coated 90^0 off-axis parabolic mirror (50338 AU; Newport Corporation). The detector signal was sent to personal computer to calculate ring-down time with the help of lab made LabVIEW program. The ring-down time in empty cavity gas cell was achieved to be 14 μs corresponding to an optical path length around 4.2 km inside the cavity. Now to scan the target absorption line, the piezo of external cavity of QCL was utilized to tune the laser finely. However to record another C_2H_2 spectra, the grating position of the EC-QCL was adjusted to achieve another frequency of QCL. During the spectral characteristics measurement, the temperature of the cavity was kept to be at room temperature (298 K) along with maintaining the temperature stability upto 1k. The gas cell is also equipped with a pressure gauge, which can measure the pressure inside the cavity upto 760 Torr with 0.2% accuracy.

7.3 Results and discussion

We utilized the cw-CRDS system to record all absorption spectra of both allowed transition $v_4+v_5(\Sigma_u^+)$-$0(\Sigma_g^+)$ and the forbidden transition $v_4+v_5(\Delta_u)$-$0(\Sigma_g^+)$ of C_2H_2 with help of EC-QCL with the resolution of 0.001 cm^{-1}. Initially, 16 rotational lines in the P branch and the 4 lines of the R branch of $v_4+v_5(\Sigma_u^+)$-$0(\Sigma_g^+)$ were recorded by injecting a certified calibration gas mixture of 2±0.1 ppm of C_2H_2 in N_2 (Air Liquid, UK, 99.99%) inside the cavity with the different cavity pressure depending on the line strength to avoid the saturation effect of ring-down absorption spectra. To acquire absorption spectra of a particular probed line of C_2H_2, we monitored the wavenumber (cm^{-1}) dependant change of decay-rate (Δk in s^{-1}) of the ring-down signal across the selected molecular transitions. However, to obtain line intensity of the particular transition, we have plotted the area under the curve (AUC) of CRDS spectra against the known concentrations of C_2H_2 inside the cavity. The spectra was then fitted with Voigt line-shape profile with FWHM obtained from expected Doppler broadening at the measured wavelength. Finally, the line-integrated absorption cross-section or line-intensity was calculated from slope of straight line fitted to the AUC vs. concentration curve divided by the speed of the light. Figure 7.1 demonstrates CRDS spectra of the P(9)

line at three different mixing ratios of C_2H_2 and the inset shows the linear variation of AUC with concentration of C_2H_2 molecules inside the cavity.
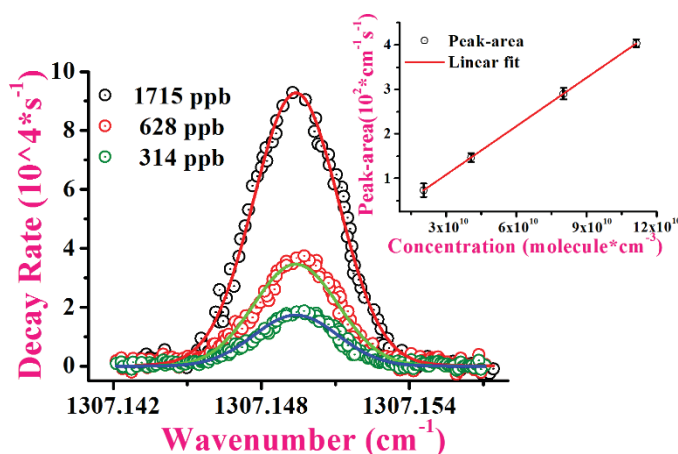
Fig. 7.1 *CRD spectra of P(9) rotational line of allowed $\nu_4+\nu_5(\Sigma_u^+)-0(\Sigma_g^+)$ band of C_2H_2 obtained at different mixing ratio of C_2H_2 at cavity pressure 2 Torr. The solid lines are Voigt fits to the line profile. The inset shows a linear regression plot between the area under ring-down spectra and molecular concentration of C_2H_2, from the gradient of which line-integrated absorption cross-section was determined.*

All the values of line strengths of numerous rotational lines of P and Q branch of the allowed $(\nu_4+\nu_5)^0$ are summarized in the Table 7.1. We obtained the line-intensity measurement uncertainty from 0.5% up to 1.7% for different rotational lines.
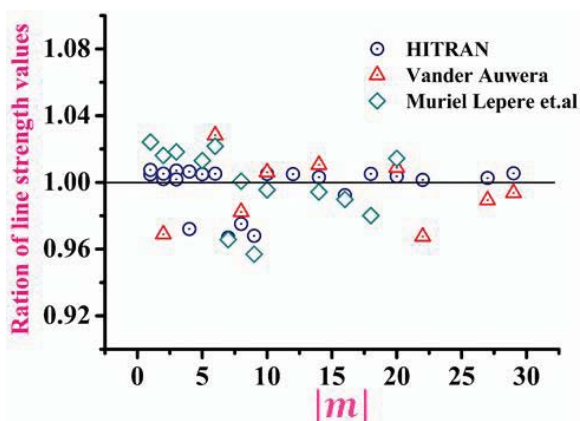
Figure 7.2 *Comparative study of line strength values of C_2H_2 of allowed $\nu_4+\nu_5(\Sigma_u^+)-0(\Sigma_g^+)$ transition with other works against different m values*

Table 7.1 *Comparison of line positions with the HITRAN database and line strength values of P and R branch of (v_4+v_5) band of C_2H_2 obtained from our CRDS setup*

| Line assignment	Centre wavenumber (HITRAN database) cm^{-1} (T)	Centre wavenumber (Experimental) cm^{-1} (E)	Absorption cross-section (Experimental) cm^{-1}mole^{-1} (E)
P29	1261.9693	1261.961(9)	$4.409\pm0.6\%*10^{-21}$
P27	1266.497	1266.489(7)	$7.965\pm0.7\%*10^{-21}$
P22	1277.761	1277.752(9)	$9.256\pm0.9\%*10^{-21}$
P20	1282.2574	1282.252(7)	$1.388\pm1.2\%*10^{-20}$
P18	1286.7564	1286.735(2)	$1.9646\pm1.5\%*10^{-20}$
P16	1291.2632	1291.256(3)	$2.5817\pm0.8\%*10^{-20}$
P14	1295.7789	1295.779(3)	$3.2619\pm0.5\%*10^{-20}$
P12	1300.3193	1300.302(0)	$3.8197\pm0.3\%*10^{-20}$
P10	1304.8771	1304.862(5)	$4.1432\pm0.8\%*10^{-20}$
P9	1307.1649	1307.149(4)	$1.2088\pm1.2\%*10^{-19}$
P8	1309.4592	1309.448(6)	$3.9981\pm1.1\%*10^{-20}$
P7	1311.7602	1311.745(3)	$1.1404\pm1\%*10^{-19}$
P6	1314.0683	1314.053(3)	$3.6697\pm1.6\%*10^{-20}$
P5	1316.3836	1316.372(6)	$9.8195\pm1.3\%*10^{-20}$
P4	1318.7063	1318.689(3)	$2.6828\pm0.8\%*10^{-20}$
P3	1321.0366	1321.018(6)	$6.5447\pm0.5\%*10^{-20}$
P2	1323.3745	1323.355(8)	$1.4978\pm0.9\%*10^{-20}$
P1	1325.72	1325.704(6)	$2.3038\pm1.1\%*10^{-20}$
R0	1330.4343	1330.417(8)	$7.7842\pm0.7\%*10^{-21}$
R1	1332.8028	1332.739(8)	$4.6077\pm1.6\%*10^{-20}$
R2	1335.1787	1335.159(7)	$2.2439\pm1.7\%*10^{-20}$
R3	1337.562	1337.547(1)	$8.7077\pm0.6\%*10^{-20}$

We subsequently compared the line-intensities values obtained from our CRDS experiment with the HITRAN database and other previous FTS data (see the fig. 7.2). Our EC-QCL based CRDS experimental values are also in good agreement with HITRAN database value. We also experimentally evaluated the line intensity values of five rotational lines from P branch of $(v_4+v_5)^2$ using our EC-QCL coupled CRDS technique using the aforementioned method of line intensity determination.

Table 7.2 contains the line positions and line-intensity values obtained from the both FTS and CRDS system.

Table 7.2 *Comparison of line position values and line strength values of forbidden transition $(v_4+v_5)^2$ with previous FTS study*

Line assignment	Centre wavenumber (FTS study by L. Gomez et. al)	Centre wavenumber (Our study) cm^{-1}	Absorption cross-section (Our study) $cm^{-1}mole^{-1}$	Absorption cross-section (FTS study by L. Gomez et. al)
P23	NA	1290.7715	$1.67\pm0.6\%*10^{-21}$	NA
P19	1299.4204	1299.4008	$2.03\pm0.8\%*10^{-21}$	$9.323*10^{-22}$
P17	1303.8196	1303.7956	$1.83\pm1.1\%*10^{-21}$	$8.572*10^{-22}$
P15	1308.2685	1308.2652	$3.59\pm0.9\%*10^{-21}$	$6.70*10^{-22}$
P13	1312.7623	1312.7503	$3.16\pm0.8\%*10^{-21}$	$5.009*10^{-22}$

Next we investigated the N_2-broadening study of C_2H_2 molecule by introducing N_2 in the ring-down cavity (RDC) as a bath gas and we found that each rotational lines of the $(v_4+v_5)^0$ and $(v_4+v_5)^2$ transition exhibited pronounced broadening. During the pressure broadening study, CRDS spectra of each probed rotational lines of both the transitions were recorded at different cavity-pressures retaining the same numbers of C_2H_2 molecules inside the cavity beyond their Doppler-broadened limiting conditions.
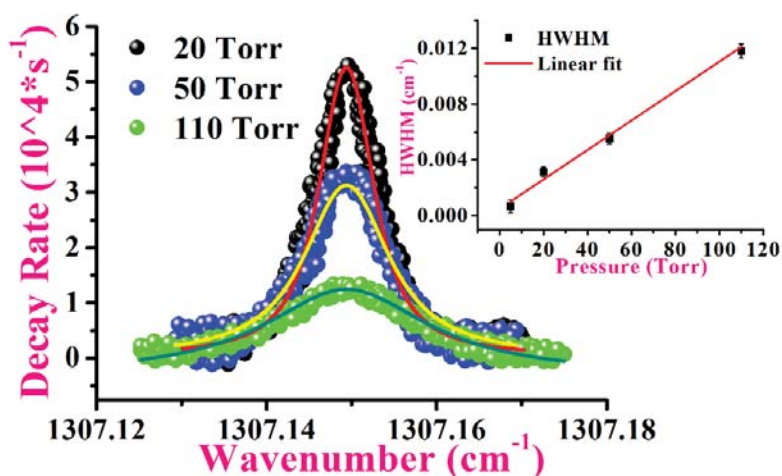
Fig. 7.3 *Variation of absorption spectra of P(9) rotational line of allowed $(\nu_4+\nu_5)^0$ transition of C_2H_2 due to different cavity pressure. The solid lines are Voight profile fit except for 110 Torr pressure, because spectra was fitted to Lorentz profile to encounter the domination of only pressure broadening effect. In the inset figure, the HWHM of the Lorentzian components have been plotted as a function of cavity pressure, from which slope of the curve gives the pressure broadening coefficient value.*

Under this condition, the absorption spectra were fitted with Voigt line shape function with known line centred position (as obtained during absent of bath gas) with fixed Gaussian FWHM and floated FWHM of Lorentzian functions. Figure 7.3 illustrates the pressure broadening effect of CRDS spectra of P(9) rotational line of allowed $(\nu_4+\nu_5)^0$ band. As the pressure increased, it has been found that peak height was diminished significantly with broadened line shape. However, we did not observe any pressure-induced line-centre wavenumber shifts from CRDS spectra. The inset of Fig.7.3 shows the variation of the Lorentzian FWHM of the best-fit Voigt profiles as a function of air pressure. We subsequently calculated the pressure broadening coefficients, γ_0 in the units of cm^{-1}atm^{-1} from the slope of linear regression analysis of such data sets. We also explored the J dependence to the pressure broadening coefficients, as illustrated in Fig 7.4. The experimentally obtained pressure broadening coefficients values are less than the air broadening coefficient values from HITRAN database. However, experimentally obtained broadening coefficient values lie within the HITRAN database error (2%-5%).
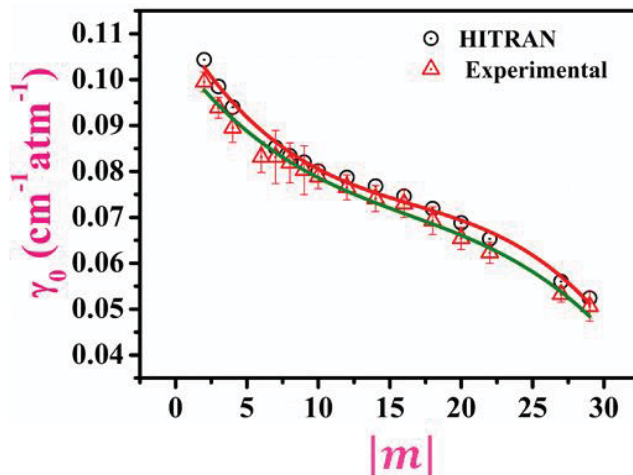
Fig. 7.4 *J-dependence of the air-broadening coefficients γ_0 for both HITRAN database and experimental value. The error bars for experimental value lies within 1 SD value. Air-broadening coefficient γ_0 values from both HITRAN database and experimental result were fitted with simple polynomial profile.*

However in comparison to self-broadening coefficient values from previous study [11], it has been observed that the higher state of C_2H_2 molecules interacts more with same molecules rather than with N_2 environment. Moreover, pressure broadening effect in presence of bath gas for 5 rotational lines of P branch of $\nu_4+\nu_5(\Delta_u)-0(\Sigma_g^+)$ band was also observed. The pressure broadening coefficients for $(\nu_4+\nu_5)^2$ band are summarized in table 7.3. It is required to be mentioned that as partial pressure of the C_2H_2 molecule is around few mTorr, the self-broadening effects are quite negligible under our experimental condition. Next we analysed the limiting sensitivity of C_2H_2 detection in ambient air with aid of the EC-QCL coupled CRDS technique by probing interference free transition lines from $(\nu_4+\nu_5)^0$ band. We have found that minimum detectable concentration can be achieved upto 15ppb at 110 Torr working pressure by probing interference free P(7) line (having strongest absorption line strength) of $(\nu_4+\nu_5)^0$ band.

Table 7.3 *N$_2$ pressure broadened coefficients for rotational lines of both (v_4+ v_5)^0 and (v_4+ v_5)^2 band*

Line	Pressure Broadening coefficient (v_4+v_5)^0 (cm^{-1}atm^{-1})	Pressure Broadening coefficient (v_4+v_5)^2 (cm^{-1}atm^{-1})
P29	0.05057±0.00319	
P27	0.0532±0.00166	
P23		0.07593±0.024
P22	0.06230±0.0023	
P19		0.06934±0.032
P20	0.06540±0.00243	
P17		0.10799±0.019
P18	0.06925±0.003	
P16	0.07296±0.00297	
P15		0.11121±0.027
P14	0.07411±0.00283	
P13		0.08899±0.033
P12	0.07652±0.00274	
P10	0.07883±0.00255	
P9	0.08026±0.0053	
P8	0.08186±0.00435	
P7	0.08314±0.00579	
P6	0.08314±0.00336	
P4	0.0895±0.00316	
P3	0.09389±0.00228	
R0	0.1115±0.00613	
R1	0.09335±0.00115	

Next, we investigated the vibrational transition dipole moment from the line intensities S_{obs} value of each ro-vibrational transition of probed lines retrieved from our EC-QCL coupled CRDS system. The transition dipole moment squared $|R|^2$ can be obtained from the following equation **(21)**:

$$S_{obs}(T_0) = \frac{1}{4\pi\varepsilon_0} \frac{8\pi^3}{3hc} \frac{v_0}{Z_{tot}(T_0)} \exp\left(-\frac{hcE''}{k_B T_0}\right)\left[1 - \exp\left(-\frac{hcv_0}{k_B T_0}\right)\right]|R|^2 L(J,l) \frac{g_s}{g_l} \qquad \textbf{7.1}$$

where $1/4\pi\varepsilon_0 = 10^{36}$ erg cm³D⁻²; h is Planck's constant equal to $6.6260755 \times 10^{-27}$ erg s (1 erg $=10^{-7}$ J); c is vacuum speed of light equal to $2.99792458 \times 10^{10}$ cm s⁻¹; g_s is the statistical weight due to nuclear spin of the lower level (1 for even J and 3 for odd J for fundamental vibrational state Σ_g^+); ν_0 is the transition wavenumber in cm⁻¹; g_l is a weight introduced to be consistent with the works of other authors in case of bands with 'l-type doubling (g_V is equal to 2 in such a case, otherwise, it is equal to 1); $Z_{tot}(T_0)$ is the total partition function at temperature T_0; $L(J, l)$ is the Hönl–London factor, J being the rotational quantum number of the lower level of the transition, and l its secondary vibrational quantum number ($l=l_4+l_5$), E'' in cm⁻¹; is the energy of the lower level; k is Boltzmann's constant equal to 1.380658×10^{16} erg K⁻¹. As $\nu_4+\nu_5$ band belongs to parallel bands ($\Delta l=0$), Hönl–London factors can be written as

$$L(J, l) = (J + 1 + l)(J + 1- l)/(J + 1) \text{ (R-branches)} \quad \textbf{7.2}$$

$$L(J, l) = (J + 1 + l)(J + 1- l)/(J + 1) \text{ (P-branches)} \quad \textbf{7.3}$$

All the E'' energy values for each fundamental transitions of lower state in the equation 7.1 have been taken from the HITRAN database. We also calculated the partition function using the expansion given by Gamache et al in 1990 **(19)** and we obtained $Z_{tot}(T_0) = 550.56$ with prior knowledge of expansion coefficients values.
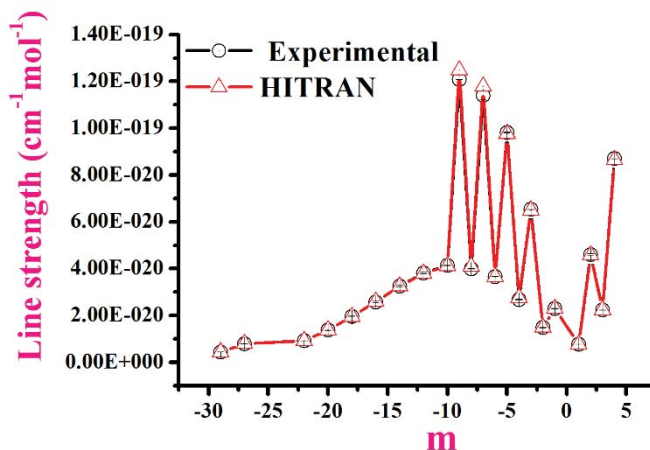
Figure 7.5 *J dependency of line strength value for rotational lines of allowed $\nu_4+{}_5\nu(\Sigma_u^+)$-$0(\Sigma_g^+)$ transition. The anomalous distribution is due to l-type resonance along with Herman–Wallis effect.*

So we utilized the equation 7.1 to calculate the squared dipole moment from the observed line intensities from our EC-QCL system and subsequently they are plotted against m (m being equal to –J and J+1 for *P* branch and R branch respectively) [see the fig. 7.4]. As we found previously (see figure 7.5) that line intensities values have J dependency due to *l*-type resonance and Herman-Wallis effect, we expanded the squared dipole moment with empirical parameters, named as Herman-Wallis constants as in J-Y. Mandin et al **(18)**.

$$|R|^2 = |R_0|^2(1 + A_1m + A_2m^2) \qquad 7.4$$

Where $|R_0|^2$ is the squared vibrational transition dipole moment, and A_1 and A_2 are the Herman-Wallis coefficients. Therefore, to obtain the value of $|R_0|^2$, A_1 and A_2, we have done a least-squares fit of the unweighted $|R|^2$ experimental values keeping $|R_0|^2$, A_1 and A_2 as adjustable parameters.

Table 7.4 *Herman-Wallis constant obtained from our study*

Herman-Wallis constant	Our Study
A_1	$-1.6205*10^{-3}$
A_2	$-8.8163*10^{-5}$
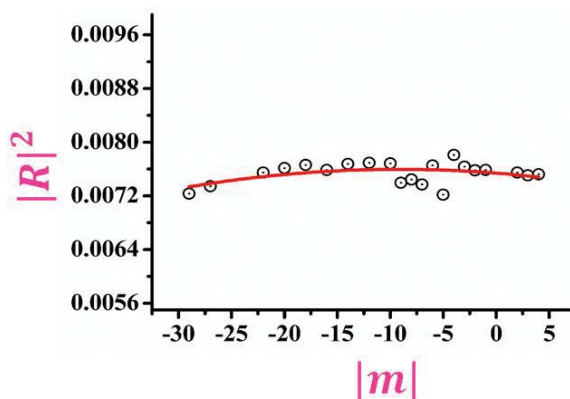
Figure 7.6. *Variation of squared transition dipole moment $|R|^2$ (in D^2) of v_4+v_5 lines of $^{12}C_2H_2$ against m for P and R branch rotational lines. The curve has been obtained using Eqs. (7.1) and fitted with polynomial function to obtain the Herman-Wallis constant.*

In table 7.4, the Herman-Wallis coefficients values have been mentioned and we also compared those values with previous study value obtained by J. Vander Auwera **(9)**. All the $|R_0|^2$ values for all each P and R branch of allowed transition has been mentioned in the table 7.5.

Table 7.5 *Comparison of squared dipole moment values (in D²) obtained from our present work with HITRAN simulation*

Lines	Transition Dipole Moment (μ^2) in D^2 Hitran	Transition Dipole Moment (μ^2) in D^2 Experimental
P29	0.0072	0.00744
P27	0.00733	0.0075
P22	0.00754	0.0076
P20	0.00759	0.00764
P18	0.00762	0.00766
P16	0.00764	0.00756
P14	0.00765	0.00764
P12	0.00765	0.00764
P10	0.00765	0.00763
P9	0.00764	0.00734
P8	0.00763	0.00739
P7	0.00762	0.00732
P6	0.00761	0.0076
P5	0.00718	0.00718
P4	0.00804	0.00777
P3	0.00758	0.0076
P2	0.00757	0.00756
P1	0.00755	0.00758
R0	0.00251	0.00253
R1	0.00751	0.00758
R2	0.00749	0.00755
R3	0.00747	0.00758

7.4 Conclusion

In summary, we exploited our EC-QCL coupled CRDS technique for absolute measurement of line positions, line intensities and N_2-

broadening coefficients of 25 individual rotational lines belonging from both allowed $(\nu_4+\nu_5)^0$ band and forbidden $(\nu_4+\nu_5)^2$ band of C_2H_2 molecule at 7.5 μm wavelength region. The line intensities values for allowed transition, obtained from our system, have 0.6%-1.6% accuracy depending on different rotational lines and the values are also in good agreement with previous FTS data and HITRAN. Whereas line intensity values for rotational lines from P branch belonging from forbidden transition are in small disagreement with previous reported FTS value. We first time measured the N_2- broadening coefficient of 20 lines from allowed transition and 5 lines from forbidden transition with 0.2%-1% accuracy. Subsequently we also measured experimental squared dipole moment value for each rotational line and also calculated Herman-Wallis coefficient values. These experimental results including several spectroscopic parameters will be useful for both superior understandings of other linear molecules and real-time application on atmospheric studies.

7.5 Reference

1. Molecular Physics, Vol. 105, Nos. 17–18, 10 September–20 September 2007, 2217–2241.
2. R. Zander, C.P. Rinsland, D.H. Ehhalt, J. Rudolph, Ph. Demoulin, J.Atmos. Chem. 13 (1991) 359–372.
3. J. Rudolph, A. Khedin, B. Bonsang, J. Geophys. Res. 97 (1992) 6181–6188.
4. K.S. Noll, R.F. Knacke, A.T. Kokunaga, J.H. Lacy, S. Beck, E.Sarabyn, Icarus 65 (1986) 257–263.
5. A. Coustenis, T. Encrenaz, B. Be´zard, G. Bjoraker, G. Graner, M.Dang-NHu, E. Arie, Icarus 102 (1993) 240–260.
6. J. Phys. Chem. Ref. Data 45, 023103 (2016); doi: 10.1063/1.4947297.
7. Matsuura, M., Wood, P. R., Sloan, G.C., & Zijlstra AA. 2006, Mon Not R Astron Soc, 371, 415.
8. J.R. Podolske, M. Lowenstein, P. Varanasi, J. Mol. Spectrosc. 107 (1984) 241–249.
9. J. Vander Auwera, J. Mol. Spectrosc. 201 (2000) 143–150.
10. D. Jacquemart, J.Y. Mandin, V. Dana, L. Re´galia-Jarlot, X. Thomas, P. Von der Heyde, J. Quant. Spectrosc. Radiat. Transfer 75 (2002) 397–422.
11. M. Lepe`re et. al. Journal of Molecular Spectroscopy 242 (2007) 25–30.
12. P. Varanasi and B. R. P. Bangaru, J. Quant. Spectrosc. Radiat. Transfer 14(1974), 839–844.
13. Y. Kabbadj, M. Herman, G. Di Lonardo, L. Fusina, J. Mol. Spectrosc. 150 (1991) 535–565.
14. L.Gomez, D.Jacquemart, N.Lacome, J.-Y.Mandin, J. Quant. Spectrosc. Radiat. Transfer, 110(18) (2009), 2102-2114.
15. S. Okubo, K. Iwakuni, K. M.T. Yamada, H. Inaba, A. Onae ,F.-Lei Hong, H. Sasada, Journal of Molecular Spectroscopy 341 (2017) 10-16.
16. F. M. Schmidt, O. Vaittinen, M. Metsälä, P. Kraus, L. Halonen, Applied Physics B, 101(3) (2010), 671–682.
17. D.Jacquemarta, J.-Y. Mandinb, V.Danab, C.Claveaub, J.Vander Auwerac;1, M.Hermanc, L.S. Rothmana, L. R5egalia-Jarlotd, A.Barbed, Journal of Quantitative Spectroscopy & Radiative Transfer, 82 (2003) 363 – 382.

18. A. Maity, M. Pal, G. D. Banik, S. Maithani and M. Pradhan Laser Phys. Lett., 14(11)(2017), 115701.

19. M.Pal et. al., Journal of Analytical Atomic Spectrometry, 34(5)(2019), 860-866.

20. M.Pal et al., Journal of Breath Research, 13 (2018) 0160.

21. J.-Y. Mandin et al. / Journal of Quantitative Spectroscopy & Radiative Transfer 92 (2005), 239–260.

22. Gamache RR, Hawkins RL, Rothman LS., J Mol Spectrosc 142(1990), 205–19.

Chapter 8

Development of quantum cascade laser based optical sensor for trace monitoring of ambient methane concentrations at various locations

8.1 Introduction

Methane (CH_4), an inflammable gas with an explosive limit of 5–15% concentration in air, is an important safety hazard in fossil fuel industries of natural gas production and storing, coal mining etc [1,2]. Atmospheric CH_4, the second most abundant green-house gas with global warming potential (GWP) of 25 times higher than carbon dioxide (CO_2) in the time horizon of 100 years, has been increased about 166% in concentration since the pre-industrial times [3]. CH_4 is predominantly produced from numerous anthropogenic sources like fossil fuel, dairy farms, paddy fields and natural sources like wetlands located at widespread regions ranging from urban to rural areas. However, the typical atmospheric concentration of CH_4 is nearly 300 times lower than the atmospheric CO_2. Therefore, routine monitoring of different sources of CH_4 with high sensitivity and specificity is essential for better evaluation of atmospheric models.

It is noted that direct absorption spectroscopy (DAS) and wavelength modulation spectroscopy (WMS) are two traditional spectroscopic techniques widely employed in the applications of trace gas sensing [4]. However, low frequency noise in light intensity fluctuations limits the sensitivity of the direct absorption technique. In the wavelength

modulation method, the laser frequency is modulated with a high frequency (kHz) external (modulating) signal and subsequently the demodulated signal is acquired at the higher harmonics of the original signal, thus eliminating the low frequency noise of the laser source. Therefore, wavelength modulation technique provides several orders of magnitude higher sensitivity than the direct absorption method [5]. In the modulation strategy, the amplitude of the second harmonic ($2f$) of the original signal is universally exploited to retrieve the sample concentration. But, the modulation technique requires frequent calibrations to standardize the electro-optic gain parameters.

In recent years, the invention of new-generation quantum cascade laser (QCL) technology marked the revolution in the fields of the optical gas sensor and atmospheric monitoring, facilitating the access to almost the entire mid-infrared (Mid-IR) region [6]. The fundamental and combinational vibrational bands of trace molecules in the mid-IR region can now be easily explored for trace detection of gases with high molecular sensitivity and specificity. Moreover, such QCLs provide room temperature operation, high optical power, compactness, mode-hop-free (MHF) broad tunability (≥ 100 cm^{-1}) and extremely narrow linewidth (≤ 0.0002 cm^{-1}). All these salient features make the QCL-based absorption spectroscopy (QCLAS) an attractive choice for the development of new-generation optical gas sensors.

The wavelength modulation spectroscopy (WMS) coupled with a continuous-wave (cw) QCL, in particular, draws the enormous attention owing to its simplicity, high sensitivity and potential for portability to detect numerous gases in real time. In recent years, some studies focused on CH$_4$ sensing in ambient air exploiting the QCL technology combined with WMS and QCLAS. For example, Cao et al. (2015) demonstrated a sensor based on a QCL operating at 7.73 μm for atmospheric monitoring of CH$_4$ with a minimum detection limit of 8.5 ppb [7]. In another work, Ren et al. (2014) illustrated a QCL based CH$_4$ sensor working at 7.8 μm with a detection limit of 5.9 ppb at the laboratory environment [3]. Furthermore, Mappe et al. (2013) employed the QCLAS technique for measurements of atmospheric CH$_4$ emission fluxes [8]. Recently, Yu et al.

(2016) reported a multi-component optical sensor at 7.8 μm utilizing an external cavity (EC) QCL with a minimum detection limit of 2.2 ppbv for CH_4 sensing [9]. Most of the reported EC-QCL based CH_4 sensors usually utilized a multi-pass cell to enhance the minimum detection limit. However, the optical alignment in a multi-pass cell is relatively critical and time-consuming. Moreover, measurement accuracy is often limited due to interference between optical beams inside the misaligned multi-pass cell. Therefore, we here have reported a CH_4 sensor with a simple gas cell coupled with a *cw* EC-QCL operating between 7.5-8 μm. The minimum detection limit for the simple cell was adjusted probing the strongest transition line of v_4 band of CH_4 centred at 1327.072 cm^{-1} and employing the WMS-2*f* detection strategy. Furthermore, the report of the feasibility of WMS-2*f* strategy for the routine monitoring of the variation of methane concentration around different anthropogenic sources of CH_4 is rather limited.

In this study, we, therefore, applied the 2*f*-modulation strategy in combination with a *cw* EC-QCL operating between 7.5-8 μm for trace detection of atmospheric CH_4. We probed the strongest absorption line of v_4 fundamental vibrational bands of methane in the entire region extending from 7.5-8 μm and thereby achieved a detection sensitivity of 11 ppb within a simple gas cell of only 1.5 metre pathlength. Finally, we employed the EC-QCL-based CH_4 sensor for routine monitoring of different sources of atmospheric CH_4 for several consecutive days to test the feasibility of the system as a field deployable sensor. We subsequently validated our results in comparison with mass-spectrometric measurements.

8.2 2*f*-WMS Theory

Wavelength modulation spectroscopic technique (using tunable diode laser), for detection of a trace gas, was widely used by many researchers and its theory was well established many days ago [10]. Thereby, a brief discussion about WMS principal has been demonstrated here. Basically, in wavelength modulation spectroscopy, the wavelength of the laser is slowly scanned through the probed absorption line along with modulated by high frequency wave. Thus transmitted light intensity

solely depends on the slope of the absorption line. As a result, we get first and higher harmonics after demodulation of the transmitted light. Actually first and higher harmonics of transmitted light is the first and higher derivatives of the absorption line. Thus WMS is recognised as a derivative spectroscopy.

Laser absorption spectroscopy is governed by the well-known Beer lambert equation. When incident laser light scans across the sample absorption region, the transmitted light intensity follows the Beer's law [17-18]:

$$I(v) = I_0(v) \exp[-\alpha(v)L] \qquad \text{(8.a)}$$
$$= I_0(v) \, exp[-S_j(T)P_x\phi_i(v)L] \qquad \text{(8.a.1)}$$

where $I_o(v)$ is the incident laser intensity, $I(v)$ is the transmitted laser intensity, v is the emission frequency, $a(v)$ is the absorption coefficient, $S_j(T)$ is the absorption line strength of jth transition at temperature T, P is the total pressure, x is the mole fraction of the target species, $\phi_j(v)$ is the transition line shape and L is the optical path length. In the low concentration cases ($\alpha(v)L \le 0.05$), Eq.(8.a) can be written as

$$I(v) = I_0(v)[1 - \alpha(v)L] \qquad \text{(8.b)}$$

Modulation spectroscopic techniques are basically classified into two categories, one is a frequency modulation (FM), and another is wavelength modulation (WM). In FM spectroscopy, laser light is modulated at frequencies larger than the target absorption line width, where as in WMS technique; modulation frequency should be kept lower than the absorption line width. In present study makes uses of WMS technique.

In WMS technique, modulated laser frequency can be expressed as

$$v(t) = v_{ave} + aCos\,(wt) \qquad \text{(8.c)}$$

Where v_{ave} is the mean laser frequency, a is the modulation amplitude and w is the angular frequency of the modulation. Taking $\sum_k \binom{n}{k} I_0(v)$ as independent of the laser frequency, Eq. 8.b can be written as

$$I(v) = I_0(v)[1 - \alpha(v_{ave} + aCos\,(wt))L] \qquad \text{(8.d)}$$

So the transmitted light intensity has a time dependent part, which can be expanded into cosine Fourier series corresponding to multiples of w:

$$\alpha\left(\nu_{ave} + aCos\left(wt\right)\right) = \sum_{n=0} H_n(\nu_{ave})Cos\left(nwt\right) \qquad \textbf{(8.e)}$$

Where $H_n(\upsilon_{ave})$ demonstrates the nth Fourier co-efficient of the modulated absorption coefficient. Now incorporating lock-in-amplifier, n[th] harmonic of the modulation frequency can be detected. As detection bandwidth shifts to large frequency region, it gives the advantage to avoid 1) the low frequency drifts in laser intensity and 2) excess laser noise ($\sim 1/f$). Thus signal to noise ratio has been increased immensely.

8.3 Instrumental setup of 2*f*-WMS sensor

A schematic of the QCL based sensor is shown in Fig. 8.1. The physical dimension of the optical sensor is about 100 cm (L) X 45 cm (W) X 35 cm (H) as shown by the dotted line in the Fig. 1. The sensor has currently been tested in the lab environment. In this sensor, a room temperature *cw* EC-QCL (MHF-41078; Daylight Solutions, USA) with mode-hop-free tunability of 1257-1341 cm^{-1} and optical power of ≥ 80 mW was employed as the optical source. An optical isolator (FIO-5-7.8; Innovation Photonics) was utilized to isolate the QCL beam from the back-reflected light of the other optical components present in the set-up.
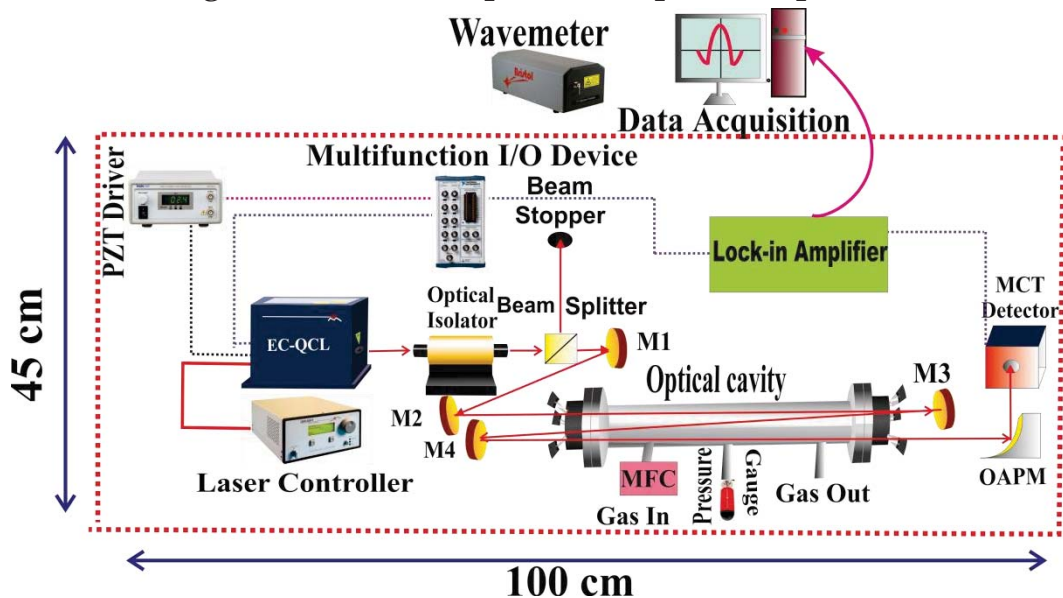

Fig. 8.1 *A Schematic of QCL based optical sensor of CH₄. The dotted line indicates the practical dimension of the sensor. M1, M2, M3, M4 represents the Bending Mirror and OAPM stands for off-axis parabolic mirror.*

The laser beam was split into two using a beam-splitter where most of the beam was directed to a gas cell. However, a tiny fraction of the laser beam was blocked by a zero iris which might be opened occasionally to monitor the wavenumber stability using a wavemeter (621B-MIR; Bristol Instruments). The quartz coated gas cell (CRD-Optics) was 50 cm long with a cell volume of 600 ml and comprised of two ZnSe windows. We utilized two additional gold-coated mirrors just outside of the gas cell to make additional two passes of the laser beam through the cell and thereby enhanced the optical pathlength up to 1.5 metre. However, the present configuration of the gas cell in this sensor is more stable and less complicated than the multi-pass cell like Herriott and White cell. The optical power just before entering the cell was about 35 mW. The final optical signal leaving from the gas cell was subsequently focussed on to a TE cooled, Mercury-Cadmium-Telluride (MCT) detector (PVI-4TE-8-1X1; Vigo System S.A.) using a gold-coated 90° off-axis parabolic mirror. A pressure-controlled mass-flow-controller (MFC) from MKS Instruments was connected to the gas cell to regulate the gas flow in to the cell maintaining the final cell pressure of 150 Torr. A multifunction I/O card (National Instruments BNC-2110) was employed to modulate the QCL using a high frequency sine wave with a frequency of 30 kHz and peak-to-peak voltage (V_m) of 2.5volt whereas a piezoelectric transducer (PZT) driver (MDT693B; Thor Labs) was utilized to scan the laser wavelength over the selected absorption line of CH_4 using a low frequency sine wave (f_{scan}=2.5 Hz). Finally, the signal was demodulated using a lock-in-amplifier (Stanford Research Systems SR830 DSP) with a time constant of 30 milliseconds. The demodulated signal was acquired by a high-speed (100 MS/s) data-acquisition card (5122 PCI National Instrument, 14-bit, 100 MHz bandwidth) and subsequently analyzed by the custom written LabVIEW program.

8.4 Results and Discussions

8.4.1 Selection of transition line of CH₄

In traditional molecular absorption spectroscopy, the detection sensitivity mainly depends on the inherent absorption line-intensity of the target gas molecule.
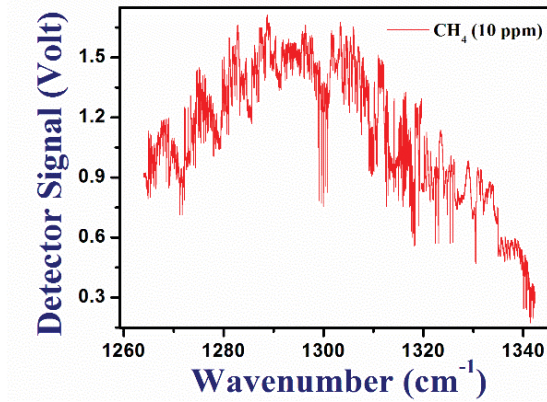
Fig. 8.2 *A direct absorption spectra of standard CH₄ (10 ppm) within the entire tuning region of the QCL for the optical pathlength of 1.5 metre at 50 Torr cell pressure and 296 K temperature*

However, spectral interferences from the other species, which adversely affect the specificity, precision, and the measurement accuracy, are required to be considered for the optimum selection of the absorption line of the target molecule.
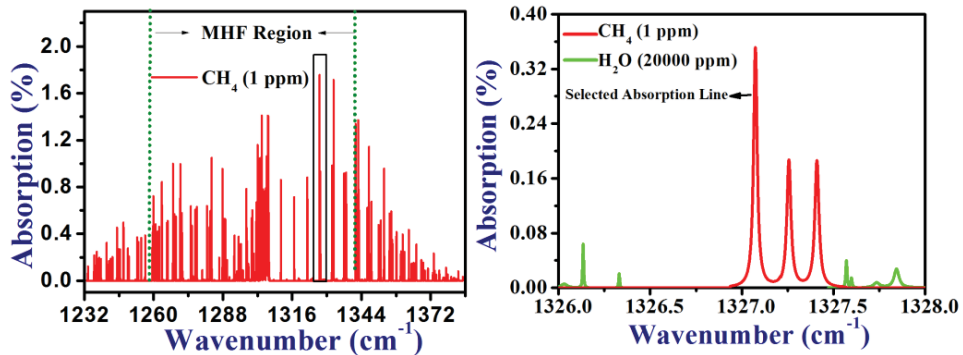

Fig. 8.3 (a) *HITRAN simulation of absorption spectrum of ν_4 fundamental vibrational band of CH₄, originated around 7.6μm, for the mixing ratio of 1 ppm at the experimental conditions of 150 Torr pressure, 296K temperature and optical pathlength of 1.5 metre. The dotted region marks the MHF running range of the present QCL.* **(b)** *The HITRAN simulation of the selected CH₄ absorption line at 1327.072 cm⁻¹ with the major atmospheric constituents at the experimental conditions showing no spectral interferences.*

The present *cw* EC-QCL with MHF tuning range of 1257-1340 cm^{-1} provides us with an access to the almost entire v_4 fundamental vibrational band of CH_4 in this spectral region. The broad tunability of the present QCL has been depicted in the Figure 8.2. We carefully selected the interference free absorption feature of CH_4 with strongest line-intensity within the entire v_4 band of CH_4. The simulated absorption profile of entire v_4 fundamental vibrational bands of CH_4, from the HITRAN database [11], is shown in Fig. 8.3a with the concentration of 1 ppm CH_4. The simulation was carried out under the experimental conditions of 150 Torr pressure, 296K temperature and optical path length of 1.5 metre. In this study, we probed the strongest CH_4 transition line centred at 1327.072 cm^{-1} with line-intensity of 9.61 x 10^{-20} cm^{-1}/(molecule/cm^{-2}). The selected absorption line is also free of the interferences of other major atmospheric constituents like H_2O, CO_2, N_2O and C_2H_2 etc. (Fig. 8.3b) and thereby ensures highly sensitive and molecular-specific monitoring of atmospheric CH_4.

8.4.2 Optimization of the 2*f* modulation signal

In the WMS-2*f* detection strategy, the signal amplitude is strongly associated with the modulation depth which is eventually governed by the modulation frequency. We utilized the modulation frequency of 30 kHz to achieve maximum possible modulation depth of 2.5 GHz owning to the limitation of the present cw QCL (Fig. 8.4 (a)). We, thereafter, exploited the amplitude modulation to maximize the amplitude of WMS-2*f* signal varying the amplitude or voltage (Vm) of the modulating frequency of 30 kHz. We, therefore, measured the amplitude of the WMS-2*f* signal as a function of the modulating amplitude (Vm) and found that the signal-to-noise ratio initially increases with the increase of the modulating amplitude. However, further increase of the modulating voltage results in an increase of the line-width of the 2*f* signal which eventually decreases the signal (Fig. 8.4 (b)).The amplitude of WMS-2*f* signal was then plotted as a function of modulating amplitude (V_m) as shown in Fig. (8.3 (c)) and the maximum WMS-2*f* signal was achieved at the modulation amplitude of 2.8 Volt.
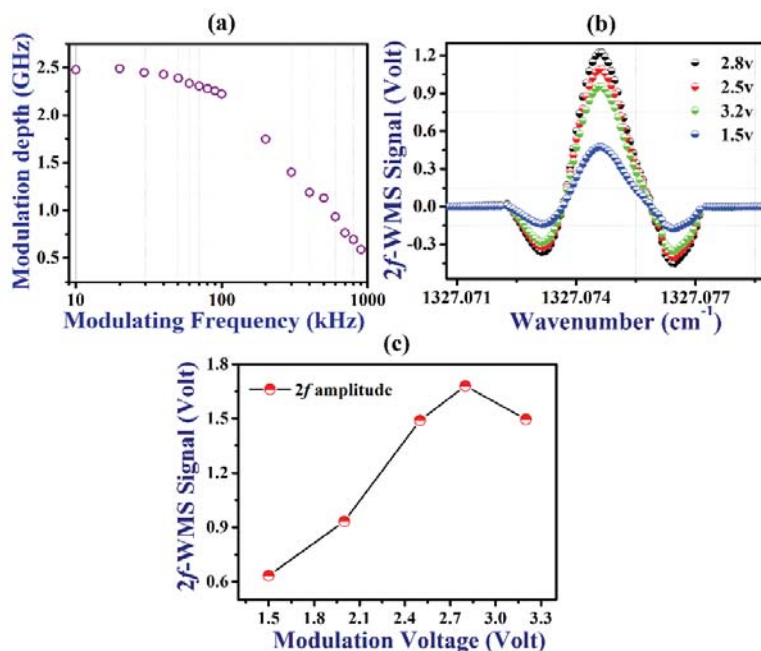
Fig. 8.4 *(a) The variation of the modulation depth within the limited range of modulation frequency of 10 kHz – 1 MHz for the present cw QCL. (b) WMS-2f spectra of 60 ppm of CH_4 centred at 1327.072 cm^{-1} for different modulating voltages at the pressure of 150 Torr. (c) The variation of the amplitude of WMS-2f spectra of 60 ppm of CH_4 as a function of the modulation voltage.*

8.4.3 Direct absorption vs. modulated signal

Figure 8.5 illustrates the typical 1st, 2nd and 3rd harmonic (i.e. 1*f*, 2*f*, and 3*f*) WMS signals of the selected absorption line of CH_4 centered at 1327.072 cm^{-1} for the optimized modulation voltage of 2.8 volts, sample pressure of 150 Torr and mixing ratio of 60 ppm.
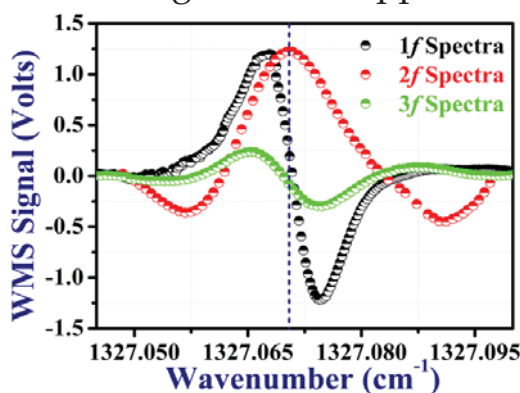
Fig. 8.5 *1st, 2nd and 3rd harmonic profiles of the absorption line of CH_4, centred at 1327.072 cm^{-1} for the mixing ratio 60 ppm at a pressure 150 Torr.*

In this study, we utilized the WMS-2*f* detection strategy to retrieve the sample concentration.
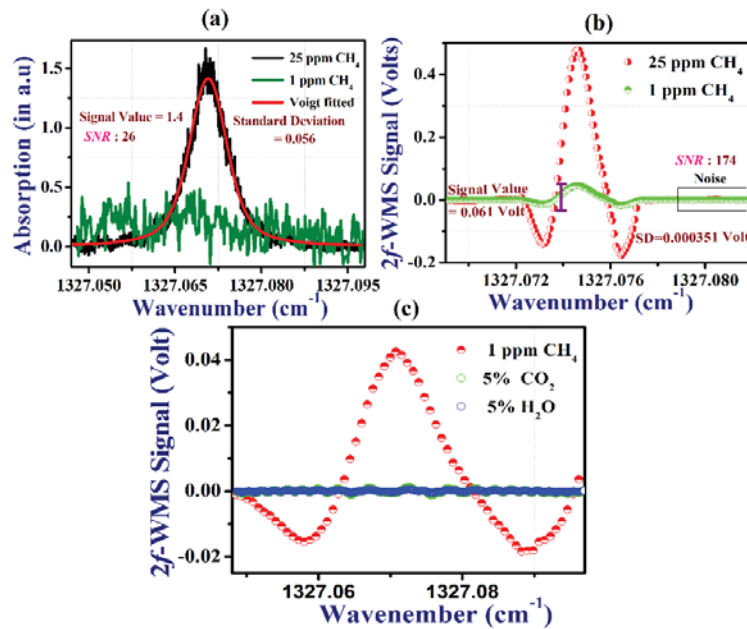
Fig. 8.6 (a) *Direct absorption spectra for 25 ppm and 1 ppm mixing ratios of CH₄. The absorption spectra of 25 ppm of CH₄ is fitted with the voigt function.* **(b)** *WMS-2f spectra of 1 ppm of CH₄ at same experimental conditions with a signal-to-noise ratio (SNR) of 174.* **(c)** *WMS-2f spectra of H₂O (5%) and CO₂ (5%) along with CH₄ (1 ppm)*

A comparison between direct absorption and modulated 2*f*-signal for the different standard concentrations of CH₄ is shown in Fig. 8.6a and 8.6b. It is evident that WMS-2*f* signal provided at least two orders of magnitude higher sensitivity compared to the direct absorption signal at the same experimental conditions. We thereafter checked the potential interferences from two major atmospheric constituents i.e. H₂O and CO₂ at their relative mixing ratios in the environment and no effect was observed at the selected absorption line of CH₄ at 1327.072 cm⁻¹ (Fig. 8.6c), thereby confirming the molecular selectivity of the trace detection of CH₄.

8.4.4 Calibration of WMS-2*f* sensor

We next calibrated the sensor by measuring the WMS-2*f* signals for different standard mixing ratios of CH₄ at the optimized experimental conditions as mentioned before. A good linear correlation (R²=0.9997) was achieved between the 2*f*-amplitude and concentrations of CH₄ (Fig. 8.7a).
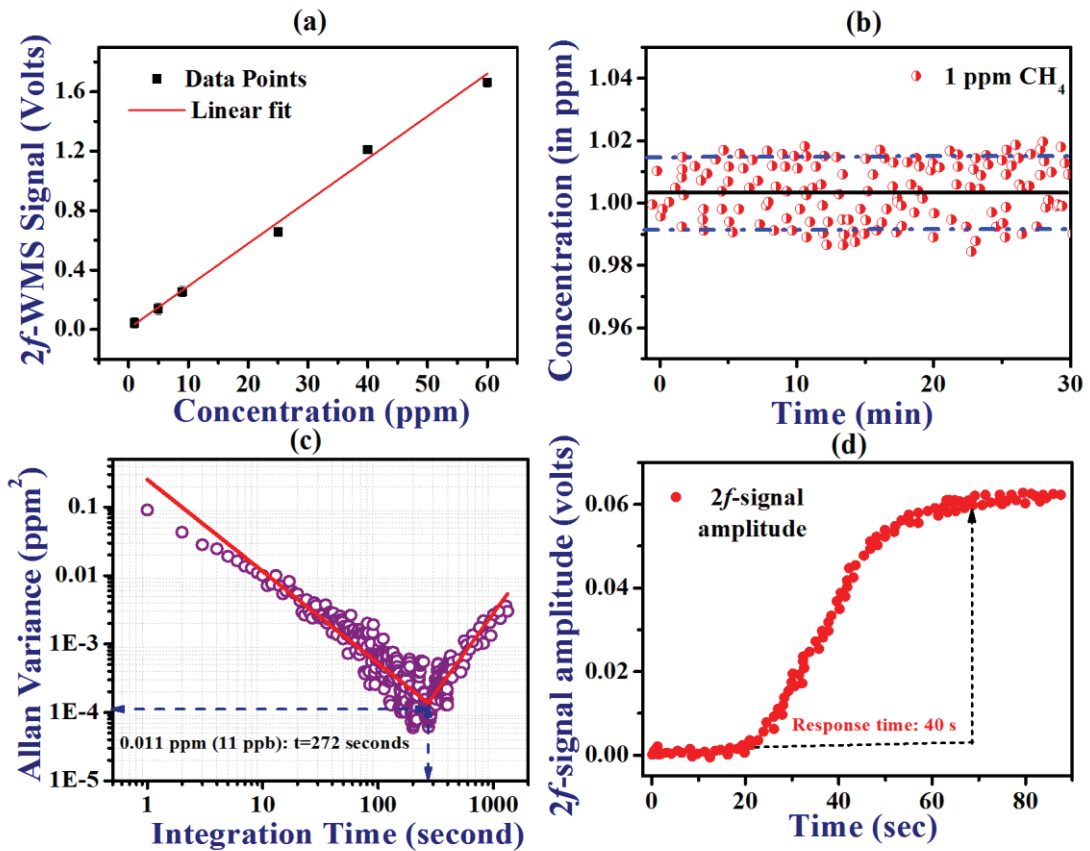
Fig. 8.7 *(a) A calibration curve representing the amplitude of the WMS-2f signal for the different mixing ratios of CH₄. The red line shows the linear fit of the data points. (b) Time variation of the concentration after measuring 1 ppm of CH₄ for 30 minutes. The dotted region represents the 1 standard deviation from the mean value of 1 ppm. (c) Allan variance plot indicating the stability and minimum detection limit of the CH₄ sensor. (d) Measurement of response time by changing the CH₄ concentration from 0 ppmv (zero air) to 1 ppmv.*

Thereafter, we checked the system stability and measurement repeatability by measuring the standard concentration of 1 ppm of CH_4 continuously for the period of half an hour (Fig. 8.7b) and found a measurement accuracy of 7.8 ppb (1 standard dev.) for the entire time of the measurements. Finally, we performed the Allan Variance test [12] (Fig. 8.8c) to evaluate the measurement precision of the sensor. The Allan variance decreases with increasing integration time at the initial phase of the plot which was fitted with a linear line of gradient -1 and the region is termed as white noise region. The optimum integration time was found to be 272 seconds which corresponds to a minimum detection limit of 11 ppb.

Table 8.1 *Comparison of sensitivity limits of different WMS systems reported earlier.*

	Optical Source of WMS system	WMS Technique	Min detectable Concentration of CH$_4$	Detection Sensitivity (ppb* meter)
Cao *et al.* (2015) [7]	QCL at 7.73 μm	• 2*f*-WMS • Multipass Herriott cell with a 76-m path length	8.5 ppb	646
Ren *et al.* (2014) [3]	QCL at 7.8 μm	•2*f*-WMS • Multipass Herriott cell of length 57.6-m	5.9 ppb	339.84
Yu *et al.* (2016) [9]	QCL at 7.8 μm	•Wavelength modulation spectroscopy of second harmonic normalized by first harmonic detection (WMS-2*f*/1*f*) • Multipass cell of length 57.6-m	2.2 ppbv	126.72
Liang *et al.* (2018)[16]	Distributed Feedback laser at λ = 1.654 μm	•2*f*-WMS • Open-path of length 1.45m	130 ppb	188.5
Song *et al.* (2018)[17]	Interband Cascade Laser (ICL) at 3.291 μm	•2*f*-WMS •Multi-pass gas cell length of 16m.	5.84 ppbv	93.44
Ding *et al.* (2016)[18]	Distributed Feedback laser at λ = 1.654 μm	•2*f*-WMS •Multi-pass gas cell length of 10m.	5 ppm	50000
Present Study	Quantum Cascade Laser (QCL) at λ = 7.8 μm	•2*f*-WMS •Multi-pass gas cell length of 1.5 m.	11 ppb	16.5

The further averaging after 272 seconds did not improve the measurement precision in the $1/f$ noise dominated region. The system, for the longer time scale, shifted from $1/f$ noise to drift dominated region of gradient +1 where Allan variance again started to increase. Hence, the measurement parameters of the sensor ensured the highly sensitive detection of trace CH_4. We subsequently compared the detection sensitivity of the present sensor with the other methane sensors based on modern WMS methods (Table 8.1). We finally evaluated the response characteristic of this sensor. A typical response time of about 40 seconds was obtained by changing the CH_4 concentration from 0 ppmv (zero air) to 1 ppmv by simultaneously measuring the WMS-$2f$ signal amplitude.

## 8.4.5 Real time application of sensor by ambient Methane measurement

We next employed the present lab-based sensor for routine monitoring of atmospheric CH_4 originated from various anthropogenic sources to assess the feasibility as a future field-deployable sensor. We identified various sources of atmospheric CH_4 as listed in Table 8.2, within a radius of 10 km around our institute, S. N. Bose Centre, Kolkata and collected air samples in Tedlar bags each day of a week. Each sample was measured thrice and standard 1 ppm of CH_4 was measured between any two successive measurements of the atmospheric samples to ensure the measurement accuracy. Moreover, zero air was measured at the optimized experimental conditions in every occasion after each sample measurement to ensure the removal of the residual of the previous sample. All the measurements were carried out each day within 3 hours after collecting the samples from different sources. It is evident from the Table 8.2 that CH_4 concentration at the local environment varied from 1 ppm to 8 ppm (Table 8.2) depending on the nature of the sources. A map of the different locations of the collected samples has been depicted in Fig. 8.8a. We observed that the level of CH_4 was quite high (4-8 ppm) for the sources like paddy field, and dairy farm in comparison to the atmospheric concentration of CH_4 (~1.8 ppm) present in the Institute campus. We speculate that the anaerobic biodegradation of organic compounds in paddy fields and bacterial action in the digestive tracts of the ruminant

animals in the dairy farm may have possibly attributed to the high evolvement of methane at the respective local environments [13]. In contrast, the biodegradation of the industrial waste product may possibly contribute to the enrichment of CH_4 concentration in the industrial sector [14], but the detailed long-term and continuous monitoring of CH_4 are required to get insight into the actual source dependent CH_4 emission in our study. However, all the atmospheric samples were additionally measured by the residual gas analyzer mass-spectrometry system [15] to validate the measurement accuracy of the QCL- based CH_4 sensor.

TABLE 8.2 *Comparison of CH_4 mixing ratios at the different locations around S. N. Bose Centre, Kolkata.*

	CH$_4$ Concentration in ppm									
	Paddy Field		Industrial Sector		Dairy Farm		Wetland		Institute Campus	
	Morning (06:00-07:00)	Afternoon (15:00-16:00)	Morning (06:00-07:00)	Afternoon (15:00-16:00)	Morning (06:00-07:00)	Afternoon (15:00-16:00)	Morning (06:00-07:00)	Afternoon (15:00-16:00)	Morning (06:00-07:00)	Afternoon (15:00-16:00)
Day 1	3.94±0.039	4.94±0.033	4.2±0.052	4.3±0.055	7.8±0.078	6.9±0.073	2.4±0.023	2.3±0.023	1.87±0.034	1.86±0.024
Day 2	4.3±0.067	4.1±0.057	4±0.037	4.2±0.039	8.2±0.08	8.9±0.076	2.5±0.035	3.5±0.035	1.83±0.044	1.89±0.044
Day 3	4.2±0.065	4.6±0.069	4.6±0.067	4.1±0.061	7.9±0.049	9±0.049	2.5±0.025	3.1±0.025	1.88±0.069	1.98±0.062
Day 4	3.95±0.055	4.3±0.059	4.3±0.032	4.3±0.039	7.7±0.067	8.7±0.067	2.3±0.028	3.2±0.028	1.87±0.024	1.82±0.034
Day 5	4.5±0.034	4.3±0.035	4.8±0.031	4.8±0.034	8.6±0.063	7.6±0.053	2.5±0.022	2.7±0.023	1.83±0.07	1.96±0.07
Day 6	4.8±0.044	4.4±0.041	4.9±0.059	4.9±0.051	8.4±0.069	8.0±0.065	2.6±0.021	2.9±0.027	1.84±0.052	1.94±0.053
Day 7	4.3±0.045	4.6±0.042	5.0±0.055	5.0±0.059	8.2±0.039	8.5±0.049	2.7±0.017	2.3±0.019	1.88±0.027	1.98±0.027

We found an excellent agreement (Fig. 8.8b) between the measurements from both the systems which signifies the robustness and efficacy of the EC-QCL-based sensor for monitoring of atmospheric methane with a wide range of concentrations.
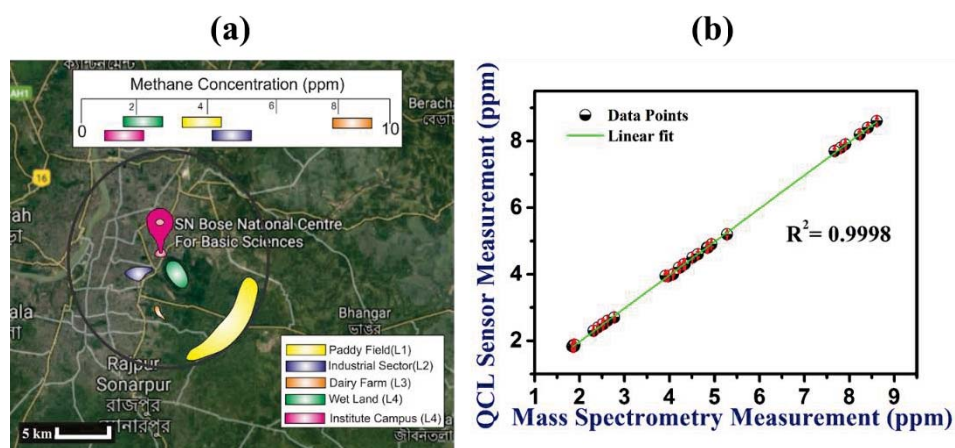
Fig. 8.8 *(a) Map of the different locations around S. N. Bose Centre with the typical ambient concentration of CH₄. (b) A linear regression plot of the mixing ratios of atmospheric CH₄ measured by the QCL-based sensor and RGA-MS system.*

8.5. Conclusion

We demonstrated a CH_4 sensor exploiting the WMS-2*f* detection strategy coupled with a *cw* EC-QCL operating within the range of 7.5-8 μm for high sensitive and molecular-specific monitoring of atmospheric CH_4. We utilized the broad MHF frequency tunability of the QCL to select and simultaneously probe the interference free strongest absorption line of the v_4 fundamental bands of CH_4 and thereby achieved sensitivity in the level of ppb within a short optical pathlength of 1.5 metre. A minimum detection limit of 11 ppb was obtained for the integration time of 272 seconds. We further employed the sensor to monitor the different anthropogenic sources of CH_4 in the atmosphere measuring the local CH_4 concentrations in the off-line mode for a week and the measurement accuracy was subsequently verified by the mass-spectrometric measurements. Therefore, we validated the efficacy of the current QCL-based system as a future field-deployment sensor for routine monitoring of atmospheric methane concentrations at various locations.

8.6 References

1. Q. Gao et al., Tunable multi-mode diode laser absorption spectroscopy for methane detection, Sens. Actuators A: Phys., vol.199, pp.106–110, 2013.

2. Q. Wang, Z. Wang, and W. Ren, Wavelength-stabilization-based photoacoustic spectroscopy for methane detection, Meas. Sci. Technol., vol.28, pp.65-102, 2017.

3. W. Ren, W. Jiang, and F. K. Tittel, Single-QCL-based absorption sensor for simultaneous trace-gas detection of CH4 and N2O, Appl. Phys. B, vol. 117, pp. 245–251,2014.

4. J. Shemshad, S.M. Aminossadati, and M.S. Kizil, A review of developments in near infrared methane detection based on tunable diode laser, Sens. Actuators B: Chem., vol.171, pp.77–92, 2012.

5. G. Hancock, J. H. van Helden, R. Peverall, G. A. D. Ritchie, and R. J. Walker, Direct and wavelength modulation spectroscopy using a cw external cavity quantum cascade laser, Appl. Phys. Lett., vol. 94, pp.201110, 2009.

6. A. Kosterev, G. Wysocki, Y. Bakhirkin, S. So, R. Lewicki, M. Fraser, F. Tittel, and R. F. Curl, Application of quantum cascade lasers to trace gas analysis, Appl. Phys, vol.90, pp.165–176, 2008.

7. Y. Cao, N. P. Sanchez, W. Jiang, R. J. Griffin, F. Xie, Lawrence C. Hughes, Chung-en Zah, and Frank K. Tittel, Simultaneous atmospheric nitrous oxide, methane and water vapor detection with a single continuous wave quantum cascade laser, Optics Express, vol.23(3), pp. 2121-2132, 2015.

8. I. Mappé, L. Joly, G. Durry, X. Thomas, T. Decarpenterie, J. Cousin, N. Dumelie, E. Roth, A. Chakir, and P. G. Grillon, A quantum cascade laser absorption spectrometer devoted to the in situ measurement of atmospheric N2O and CH4 emission fluxes, Rev. Sci. Instrum, vol.84, pp.02103–02111, 2013.

9. Y. Yu, N. P. Sanchez, R. J. Griffin, and F. K. Tittel, CW EC-QCL-based sensor for simultaneous detection of H2O, HDO, N2O and CH4 using multi-pass absorption spectroscopy, Optics Express, vol.24(10), pp. 10391-10401, 2016.

10. Gottipaty Rao, Chakrapani Gudipaty, Daniel Martin, Higher harmonic detection employing wavelength modulation spectroscopy and near infrared diode lasers: An undergraduate experiment, Am. J. Phys. 2009, 9, 821-825.

11. L. Rothman et al., The HITRAN 2012 molecular spectroscopic database, J Quant Spectrosc Radiat Transf., vol.130, pp.4, 2013.

12. P. Werle, R. Mucke, and F. Slemr, The limits of signal averaging in atmospheric trace-gas monitoring by tunable diode-laser absorption spectroscopy (TDLAS), Appl. Phys. B, vol. 57, pp. 131-139 , 1993.

13. G. K. Heilig. The greenhouse gas methane (CH_4): Sources and sinks, the impact of population growth, possible interventions, Popul Environ., vol. 16, pp.109, 1994.

14. K. Minami, A.R. Mosier, and R. Sass. CH4 and N2O: Global Emissions and Controls from Rice Fields and Other Agricultural and Industrial Sources, NIAES Series 2, YOKENDO Publishers, Tokyo, 234, 1994.

15. S. Das, A. Maity, M. Pradhan, and S. Jana. Assessing Atmospheric CO2 Entrapped in Clay Nanotubes using Residual Gas Analyzer, Anal. Chem., vol.88 (4), pp.2205–2211, 2016.

16. Wenke Liang *et al;* Developing CH_4 detection limit at λ = 1.654 µm by suppressing optical interference fringes in wavelength modulation spectroscopy, Sensors and Actuators B: Chemical, Volume 255, Part 3, Pages 2614-2620, 2018.

17. Fang Song *et al;* Interband cascade laser-based ppbv-level mid-infrared methane detection using two digital lock-in amplifier schemes, Appl. Phys. B vol.124, 51, 2018.

18. Wuwen Ding *et al.* Baseline-offset' scheme for a methane remote sensor based on wavelength modulation spectroscopy, Measurement Science and Technology, Vol 27, 2016.

Chapter 9

Spectroscopic measurement of water isotopes (δD, $\delta^{17}O$ & $\delta^{18}O$) for understanding the isotope-selective water-metabolism in human body

9.1 Introduction

Water, the most abundant constituent of body fluids in humans, plays a critical role for various enzymatic and chemical reactions in the body. It is well-established that the mucosal surface of gastrointestinal (GI) tract, specifically proximal intestine, plays a pivotal role in water-metabolism in human body through which ingested water (about 90%) enters into physiological processes and becomes an essential part of human metabolism *(1,2)*. In contrast, the respired water vapor is one of the important excretion routes of liquid water from human body, and during phase change significant isotopic fractionations of the stable hydrogen (H) and oxygen (O) atoms occur between water vapor and condensed water in the respiratory system *(3)*. But, there has been no in-depth and systematic experimental demonstration of isotopic fractionations of the isotopes of H (i.e. deuterium, ^2H) and triple-oxygen isotopes (i.e. ^{16}O, ^{17}O and ^{18}O) in exhaled water during the process of respiration, and factors regulating the isotopic fractionation reactions therein still remain illusive. Moreover, the fundamental mechanisms underlying H and O quadruple-isotopic fractionations of water and their potential links to each other at the physio-biological interface of GI tract are poorly understood.

Some early evidences, however, suggest that the isotopic compositions of body water are strongly influenced by drinking water which contributes > 70% of the H atoms and > 56% of the O atoms in the body water and generally turnover of the body water in humans takes place within 2-3 weeks *(4-5)*. But, how regular consumption of drinking water, as a part of metabolism, affects the δD or $\delta^2 H$ ($^2H/^1H$), $d^{18}O$ ($^{18}O/^{16}O$) and $d^{17}O$ ($^{17}O/^{16}O$) isotopic values of exhaled water during the process of respiration is poorly understood. Furthermore, whether the water vapor in human exhaled breath is isotopically enriched or depleted in D, ^{17}O and ^{18}O in response to the individual's drinking habits-remained unknown. Recently, there has been immense interest in the evaluation of the second-order isotopic parameters like deuterium excess i.e. *d-excess* (*d-excess* = $\delta D - 8\delta^{18}O$) and *^{17}O-excess* [*^{17}O-excess* = $\ln(\delta^{17}O+1) - 0.528 \ln(\delta^{18}O + 1)$] in various water bodies such as in meteoric water and ice cores to understand the hydrological and meteorological processes *[6-8]*. However, their use in the respiration process in human body is still uncommon and the concepts have not so far been elucidated in the human GI tract. The combined measurements of both the excess parameters in human body will facilitate to eliminate the co-variation of the individual isotope ratios (i.e. δD, $\delta^{18}O$ & $\delta^{17}O$) during diverse physiological processes taking place in individual's body in response to the ingestion of various sources of drinking water.

Moreover, any impaired or unusual water absorption in the human physiological system has long been assumed to be a tracer of onset of various gastrointestinal diseases *(2)*. But such long-standing hypothesis has never been elucidated by convincing experimental evidences. Here, we hypothesized that monitoring of isotopic fractionations of water in residual fluid present in the GI tract will bear unique isotopic signatures of any potential deformations or abnormalities of the GI tract, for example in the form of ulcer, gastritis, scar, gastric erosion, inflammation etc. Nevertheless, unravelling the detailed isotopic fractionation processes of water in such a complex biological environment of the human GI tract remains a challenge.

Several lines of evidence also confirmed that the pathogen *Helicobacter pylori* (*H. pylori*) is the prime cause of various deformations in the mucosal surface of GI tract and this infection, as a worldwide healthcare problem, has received enormous attention *(2,9,10)*. However, studies in the past decade also revealed the models of enzymatic action of hydrogenase which produces molecular hydrogen and subsequently catalyzes the exchange of hydrogen isotopes between water and molecular hydrogen: H_2 (gas) + HDO (liquid/vapor) $\rightleftharpoons$ HD + H_2O *(11, 12)*. It is also known that *H. pylori* contains different membrane-bound hydrogenase enzymes *(13)*. However, to date there is no direct experimental evidence of the potential link between *H. pylori* infection and isotopic fractionation of water in human body. Moreover, in connection with the transfer of a deuterium (D) atom in this isotope-exchange reaction, the monitoring of HDO isotopes may impart a distinctive isotopic signature to exhaled water vapor during respiration. Therefore, another aspect of this study was to explore this tantalizing but untested hypothesis by the investigation of quadruple-isotopic signatures of water-metabolism at the physio-bio interface in human body.

Here, we report the first direct experimental demonstration of quadruple-isotopic fractionations of water in ingested drinking water, GI fluid and exhaled breath by using a high-precision laser absorption spectroscopic technique. We explored the underlying mechanisms of δD, $\delta^{18}O$ and $\delta^{17}O$ isotopic values in a coupled physiological and biological exchange process in human body. Subsequently, we also demonstrated the existence of *d-excess* and *^{17}O-excess* parameters in GI fluid and exhaled breath samples along with their potential signatures influenced by impaired or unusual water absorption that can be used as tracers of onset of various deformations of the GI tract. Finally, we have shown that exhaled semi heavy water, $HD^{16}O$ as a new tracer for *non-invasive* assessment of the H. *pylori* pathogen which has enormous clinical implications. This study provides new insights into the isotope-selective water-metabolism across the different compartments of human body.

9.2 Materials and Methods:

9.2.1 Human subjects:

We enrolled 58 human subjects within the age group of 15-66 years [male = 38, female = 20] with a variety of GI deformations such as gastritis, duodenal and gastric ulcer, erosion etc. Based on their medical reports involving gastrointestinal (GI) endoscopy and biopsy-based rapid urease test (RUT) along with ^{13}C-urea breath test (^{13}C-UBT), we classified all the subjects under study in two different groups: H. *pylori* positive (n=42) and H. *pylori* negative patients (n=16). When the both invasive and non-invasive test results showed identical, we confirmed the status of the infection. We excluded the subjects from our study who had undergone recent gastric surgery. We also excluded those subjects who were taking antibiotics, proton pump inhibitors or bismuth containing compounds prior to 4 weeks of the study. The Ethics Committee Review Board of AMRI Hospital, Kolkata provided the ethical approval (Study no.: AMRI/ETHICS/2013/1) to conduct the study, which was carried out according to the approved guidelines and protocols. All the subjects had given their written consent prior to the study.

9.2.2 GI fluid collection and preparation:

During gastrointestinal endoscopy procedure, 10 mL of GI fluid from each subject was aspirated through the suction channel of the endoscope and collected in an airtight mucus extraction inserted in the suction tube. Samples were then immediately stored under -20°C so that the stability of the protein is maintained in the GI fluid until the analysis is done. Fluid samples were centrifuged at 10,000 rpm for 10 min to discard the mucus prior to the analysis. Finally, the filtrate solutions were studied by a laser-based high-precision water isotope analyzer for the measurements of various isotopes without any pre-sampling procedure.

9.2.3 Breath samples collections:

After completing the GI endoscopy procedure in the AMRI Hospital, Kolkata, an empty stomach breath sample was collected from the enrolled patients in a breath collection bag (QuinTron, USA, SL No.

QT00892). The oral breath sample was initially passed through a dead-space volume (~150 mL) of the bag and subsequently the end-tidal breath was stored in a ~750 mL reservoir bag utilizing a one-way valve. Thereafter, within 1-2 days, the ^{13}C-UBT was performed on the patients and they were instructed to follow an overnight fasting (10-12 hours). To perform the ^{13}C-UBT on the patients, at first, a baseline breath sample was collected following ingestion of 4 gm citric acid dissolved in 200 mL of drinking water. The subject has regularly consumed this water in his / her daily life. Then a post-dose exhaled breath sample was collected at 15 min intervals after administration of 75 mg ^{13}C-labeled urea (CLM-311-GMP, Cambridge Isotope Laboratories, Inc., USA) up to 60 minutes.

9.2.4 Water Isotope Analysis:

9.2.4.1 δD, $\delta^{17}O$ and $\delta^{18}O$ measurements in exhaled breath:

The breath samples were analyzed by a Triple-Water Vapor Isotope Analyzer (T-WVIA, 45-EP; Los Gatos Research Inc., (LGR), CA, USA). The analyzer offers the measurement of water vapor isotopologues at a maximal scan rate of 2 Hz. It works in the principle of, where two near-IR diode lasers are coupled with a high-finesse optical cavity with off-axis configuration. One of those lasers scans absorption lines of H_2O, HDO, and $H_2^{18}O$ simultaneously and another laser probes the absorption lines of $H_2^{18}O$ and $H_2^{17}O$ at the same time to give high-precision isotope ratio values. The T-WVIA is coupled to a Water Vapor Isotope Standard Source (WVISS, LGR), vaporization device in order to calibrate the instrument to obtain high-precision water isotopic value. For breath sample measurement, the breath bag was directly connected to T-WVIA via a flexible tube with T-connector and all isotope ratios were measured up to six minutes with a scan rate of 1 Hz accumulating 360 data points for each sample. The typical precisions (1-sigma) of δD, $\delta^{18}O$ and $\delta^{17}O$ of water vapor were 0.2‰, 0.05‰, and 0.05‰, respectively at 100 sec.

9.2.4.2 δD, δ^{17}O and δ^{18}O measurements in drinking water and GI fluid:

The same Triple Isotope Water Analyzer (TIWA-45-EP) was utilized here for simultaneous measurement of the stable isotopes ratios of ^{2}H/^{1}H, ^{18}O/^{16}O and ^{17}O/^{16}O in drinking water as well as in GI fluid. The liquid samples were injected in a heated (≈85 °C) injector block (LGR) via a PAL HTC-xt auto-injector (CTC Analytics) equipped with a Hamilton 1.2 µL, zero dead volume syringe (P/N: 203185/01). The isotopic ratios of δ^{18}O, δ^{17}O, and δD in liquid samples were measured simultaneously at a speed of approximately 90s for each and individual injection. Each drinking water sample was measured six times and each GI fluid sample was measured eight times followed by the measurement of known standard samples from LGR prior to and end of actual sample measurements. In both cases, we averaged the last four measurements to obtain a single, high-throughput sample measurement. The Post Analysis software (LGR, version 2.2.0.12) from LGR was utilized to automatically calibrate the isotope measurement. To check the precision and accuracy of the measurements, we have utilized five commercially available working standards from LGR and the isotopic compositions ranged from −154.0‰ to −9.2‰, −19.49‰ to −2.69‰ and −10.30‰ to −1.39‰ for δD, δ^{18}O and δ^{17}O, respectively. The typical precision (1-sigma) of δ^{18}O, δ^{17}O, and δD values were 0.03‰, 0.03‰, and 0.2‰, respectively in our measurements.

9.2.5 Statistical Method:

We performed the one way analysis of variance (ANNOVA) for normally distributed data and non-parametric Mann-Whitney test for the statistical analyses. We considered the data are statistically significant when the two-sided p-value is < 0.05. We presented all data as mean ± standard deviation (SD). The diagnostic cut-off value was determined by utilizing the receiver operating characteristics curve (ROC), which is drawn by plotting the sensitivity against (1-specificity). We utilized the Box-Whiskers plots to show the statistical distribution of data sets. All the experimental data were analyzed by *Origin Pro.8.0* (Origin Lab Corp., USA) and *Analyse-it Method Evaluation Software*, version 2.30, UK.

9.3 Results & Discussion

9.3.1 Water isotopes measurement of drinking water

As a first step, to investigate the isotopic distribution of δD, $\delta^{18}O$ and $\delta^{17}O$ in drinking water samples, the high-precision isotopic measurements were carried out by an ultra-sensitive laser absorption spectrometer exploiting off-axis integrated cavity-output spectroscopy (ICOS) technique in a vast series of drinking water samples (n=55) which the subjects under study have regularly consumed in their daily life. The δD and $\delta^{18}O$ values in the liquid water samples were spanned from -58.01‰ to -16.52‰, with a mean value of -36.59±10.64‰ (1SD) and -8.15‰ to -2.34‰, with a mean value of -5.41±1.47‰ (1SD), respectively. The $d^{17}O$ values of drinking water samples were also distributed from -4.58‰ to -1.24‰ [mean value = -2.92±0.79‰ (1SD)]. These values are the characteristic signatures of quadruple-isotopic compositions in drinking water samples under investigation. However, the most important features observed in our experiments are in the values of *d-excess* [*d-excess* = $\delta D - 8\delta^{18}O$] which were distributed between -0.18‰ and 11.98‰ with an average value of 6.73±2.51‰ (1SD). Early studies demonstrated that the individual isotopic compositions of δD, $\delta^{18}O$ and $\delta^{17}O$ along with the values of *d-excess* in drinking water usually reflect the isotopic compositions of various sources of water bodies involving ground and surface water in a specific area over time *(4,14,15)*. Therefore, the H and O isotopic compositions of various water bodies are most likely to be accounted for the isotopic values in drinking water samples consumed by humans on a regular basis in our experiment.

9.3.2 Water isotopes distribution of respiratory water vapor

The respiratory water vapor is one of the important excretion routes of liquid water from human body. Therefore, to investigate how the individual's habit of drinking water has influenced the breath isotopic compositions of water during the respiration process, we subsequently explored the O and H isotopic fractionations of water vapor in human exhaled breath. We performed the experiments on 55 human subjects in 10-12 hours fasting conditions (i.e. empty-stomach breath samples). Those

subjects have regularly consumed such drinking water under the investigation. Figure 9.1 depicts the Box-Whiskers plots of the quantitative variations of all water isotopes in exhaled breath samples (n=55) and the data are the first experimental observations in such physiological conditions. The exhaled $\delta^{17}O$ and $\delta^{18}O$ values were spanned from -8.98‰ to -6.59‰ with a mean value of -8.77±0.98‰ and -15.52‰ to -11.368‰, with a mean value of -13.69±1.23‰ respectively, whereas the δD values were distributed between -132.91‰ and -107.12‰ (mean value= -119.63±7.27‰), suggesting the exhaled breath water vapor becomes more depleted in δD. Taken together, these new data provide a complete picture of the distribution of exhaled H and O isotopes of water vapor during the respiration process in humans.
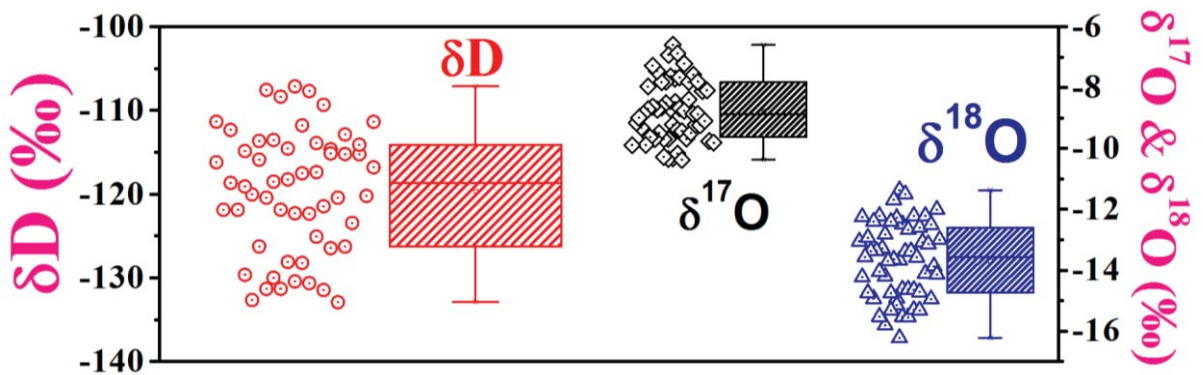
Fig. 9.1 *Box-Whiskers plots of the quantitative variations of δD, $\delta^{18}O$ and $\delta^{17}O$ isotope ratios in human exhaled breath samples (n=55)*

## 9.3.3 Relation of water isotopes between drinking water and exhaled air

We then presented the results of linear regression plots of δD, $\delta^{18}O$ & $\delta^{17}O$ in exhaled breath and drinking water samples (Fig.9.2). We obtained moderate positive correlations for δD (R^2=0.8235) and $\delta^{18}O$ (R^2=0.8699) isotopes of water between exhaled breath and drinking water, whereas in case of $\delta^{17}O$, the correlation was not significant (R^2=0.6594). Our findings, therefore, suggest that the natural metabolic routes of excretion of HDO and ^{18}O isotopes of liquid water in human body are not solely through exhaled breathing, suggesting that there might be some missing link between the underlying processes.
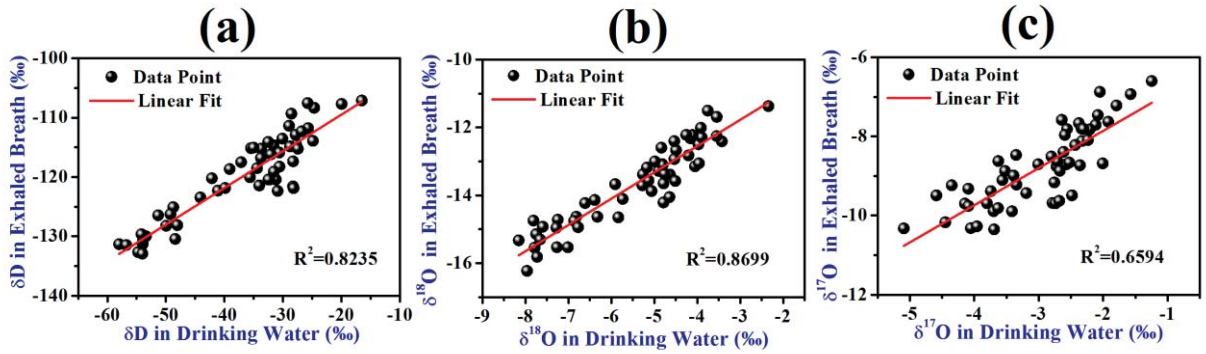
Fig.9.2. *Linear regression plots of all water isotopes between exhaled water vapor and drinking water.*

9.3.4 Water isotopes measurement of G.I fluid

We next investigated the distribution of δD, $\delta^{17}O$ & $\delta^{18}O$ isotopes in GI fluid to gain insight into the quadruple-isotopic fractionations of water occurring in such a complex biological environment that has never been explored before. Figure 9.3 demonstrates the direct experimental observations of the distribution of isotopic compositions of water in the GI fluid, which was aspirated through the suction channel of the endoscope after over-night fasting of 10-12 hours from the same human subjects (n=50) under study during their gastrointestinal endoscopy procedure in a Hospital, Kolkata.
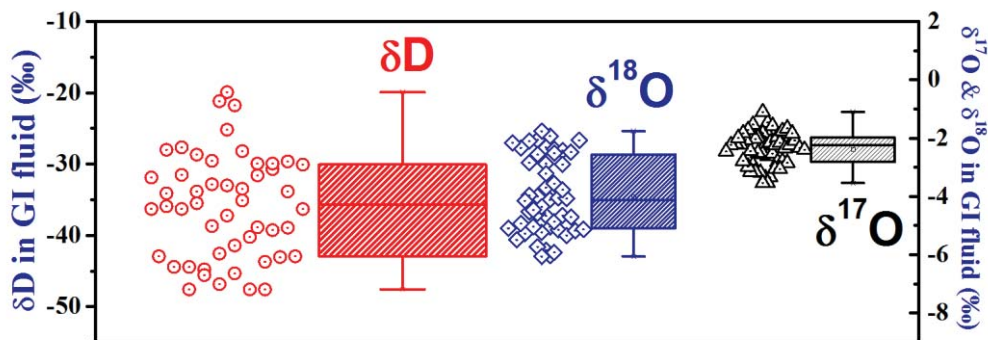

Fig. 9.3. *Box-Whiskers plots of the quantitative variations of δD, $\delta^{18}O$ and $\delta^{17}O$ isotope ratios in GI fluid (n=55)*

The residual GI fluid after 10-12 hours fasting condition provides the equilibrium isotopic fractionation of water corresponding to the signature of the transport mechanism of water through the mucosal surface of the GI tract. However, in our study, the δD values spanned from -47.59‰ to

-19.90‰ with a mean value of -35.91±7.30‰, whereas $\delta^{18}O$ & $\delta^{17}O$ isotope ratios ranged from -6.06‰ to -1.75‰ (mean value = -3.98±1.29‰) and -3.53‰ to -1.09‰ (mean value = -2.37±0.57‰), respectively. These data are the characteristic signatures of isotopic compositions of water in GI fluid and will provide useful baseline information to understand the physiological trends of human body through water-metabolism across the different compartments of human body.

9.3.5 Influence of exhaled air water isotopes by G.I fluid water isotopes

To investigate how the isotopic compositions in GI fluid are reflected in exhaled breath during respirations, we subsequently explored their potential links by evaluating the linear regression plots of water isotopes.
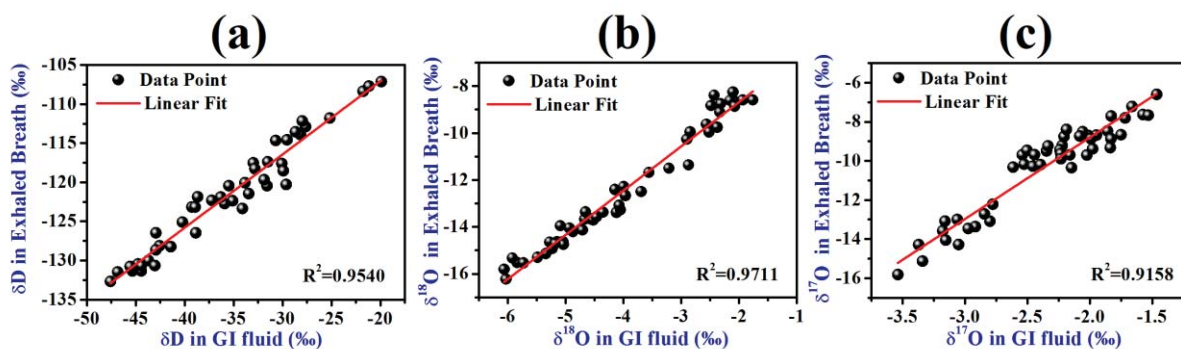
Fig. 9.4 *Correlation of three water isotopes δD, δ¹⁸O & δ¹⁷O value between human exhaled water vapor and GI fluid.*

Figure 9.4 shows the linear regression curves of exhaled water vapor and GI fluid for δD, δ¹⁷O & δ¹⁸O. We observed the significant improvements of the correlations not only for δD (R^2=0.9540) & δ¹⁸O (R^2=0.9711) values, but also for the values of δ¹⁷O (R^2=0.9158) isotopes. The differences in all the isotope ratios are most pronounced between exhaled breath and GI fluid. In addition, we found that the quadruple-isotopic signatures of the GI fluid reflect the isotopic compositions of the drinking water regularly consumed by humans. More importantly, we observed that the isotopic values of δD, δ¹⁷O & δ¹⁸O in exhaled breath were markedly depleted in comparison to the values in GI fluid. Therefore, in light of these observations of our data of isotopic fractionations on water-metabolism

demonstrate the coupling between physiological and biological exchange in human body. This conclusion was further supported by two more direct experimental studies (described later on) performed on the same human subjects who really suffered *H-pylori* diseases as well as various gastrointestinal deformations in their GI tract diagnosed by endoscopy and biopsy tests.

9.3.6 *d-excess* and ^{17}O-*excess* parameters of GI fluid, exhaled breath and drinking water samples

Next, in connection with the above measurements, we extensively evaluated the *d-excess* and ^{17}O-*excess* parameters of GI fluid, exhaled breath and drinking water samples to understand the isotopic coupling between them in human body (see Fig. 9.5). We found that the magnitudes of *d-excess* values were significantly depleted (p<0.001) in the residual GI fluid in comparison to the values of drinking water, suggesting that the lighter isotopic species of consumed water, that is, HDO were absorbed through the GI tract in much faster rate in contrast to the heavier isotopic species of water, containing ^{18}O ($H_2^{18}O$). Our findings thus confirm that these processes fractionate isotopes of water in a mass-dependent way. Moreover, in our experiment we also found that the *d-excess* values of exhaled water vapor were further diminished. A part of the liquid-phase water, which is circulating throughout the body, is diffused into the lungs in the form of vapor to be finally respired out of the circulation system. The highly diminished *d-excess* values of respired water vapor suggest that the heavier isotope of $H_2^{18}O$ is diffused into exhaled breath at a much faster rate in comparison to the lighter isotopic species of HDO. This phenomenon signifies that the transformation from liquid to vapor phase and subsequent diffusion of water vapor inside the lungs follows the mass-independent isotope-exchange process. A previous study indicates that ^{18}O-isotopes of O_2 are rapidly exchanged between water and dissolved carbon dioxide during human respiration [3]. Therefore, this supports our conclusion of the mass-independent isotope-exchange reaction in human respiratory system. In contrast, we did not observe any statistical significant differences (p>0.05) of ^{17}O-*excess* values between drinking water and residual GI fluid, suggesting that the

144

absorption rate is almost similar for both ^{17}O and ^{18}O-isotopes of water through the GI tract. However, we observed substantially depleted *^{17}O-excess* values in exhaled breath. This observation indicates that the heavier ^{18}O-isotopes are diffused into the lungs at a higher rate in comparison to the lighter ^{17}O-isotopes, which also supports our earlier observation of the *d-excess* values in exhaled breath. Therefore, our experimental findings strongly point to fundamental mechanisms underlying the mass-independent isotope-exchange processes and thus offering a possible way to disentangle the competing effects of isotopic fractionations of water during respiration.

In the above context, we have also calculated the isotope-fractionation factors of exhaled breath (α) with respect to GI fluid for all water isotopes by using this equation: $\alpha = (\delta_{exhaled\ breath} + 1000)/(\delta_{GI\ fluid} + 1000)$, where $\delta_{exhaled\ breath}$ and $\delta_{GI\ fluid}$ are the normalized values of $\delta^{18}O$, $\delta^{17}O$, and δD of exhaled breath and GI fluid, respectively. The isotope fractionation factor for α was ranged from 0.88912 to 0.9389 with a mean value of 0.9147±0.0110 (1SD), whereas the factors for ^{17}O & ^{18}O in exhaled breath were exhibited from 0.99176 to 0.9962 [mean value = 0.9935±0.0010 (1SD)] and 0.9881 to 0.9941 [mean value = 0.9925±0.0021 (1SD)], respectively.
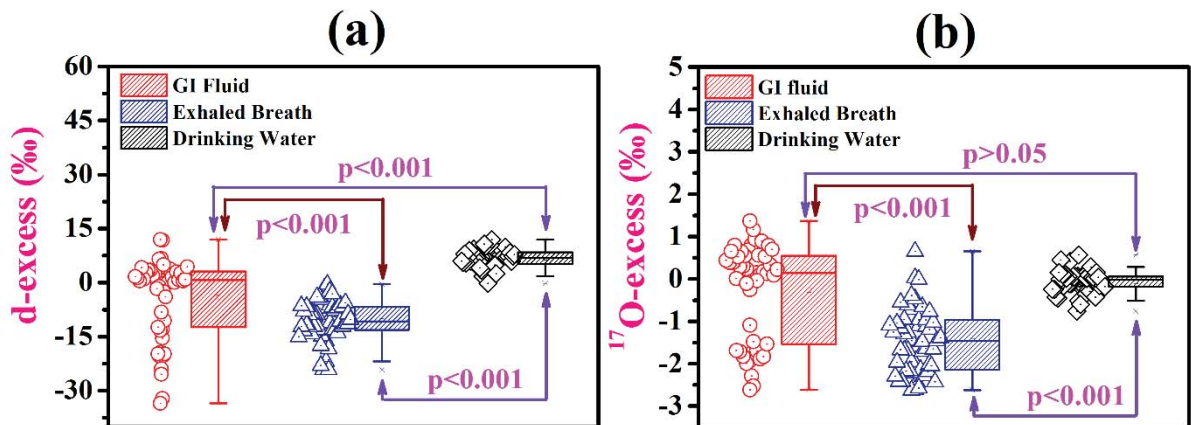
Fig. 9.5 *Distribution of second-order isotopic parameters i.e. d-excess and ^{17}O-excess values of GI fluid, exhaled breath and drinking water samples.*

The values of the fractionation factors for ^{17}O and ^{18}O-isotopes in exhaled water were quite high in comparison to the values of α and the degree of fractionation was mass-independent. Taken together, our findings confirm that significant isotopic fractionations occur of

quadruple-isotopes of water in human GI tract. The fractionations are associated with the respiration processes and indicate that exhaled water vapor bears mass-independent isotopic signatures.

9.3.7 Excretion kinetics of water isotopes of human exhaled breath and its clinical application

We further explored the time-dependent excretion kinetics of exhaled δD, $\delta^{17}O$ and $\delta^{18}O$ of water for individual persons who actually suffered *H. pylori* infection in order to understand how the isotopic fractionations of water are affected in exhaled breath due to the presence of *H. pylori* pathogen in the gastric environment. Figure 9.6(a,b,c) depicts the typical time-dependent excretion kinetics patterns of H and O isotopes of water in exhaled breath for H. *pylori* infected (n= 42) and non-infected persons (n=16) following ingestion of 75 mg ^{13}C-enriched urea with 200 mL of drinking water. The excretion kinetics of δD, $\delta^{17}O$ and $\delta^{18}O$ in exhaled water vapor associated with urease activity of the *H. pylori* pathogen in GI fluid were expressed as the delta-over-baseline (DOB) values relative to the Vienna Standard Mean Ocean Water (VSMOW) i.e. $\delta_{DOB}D‰$ = $[(\delta D‰)_{t=t}$ - $(\delta D‰)_{t=basal}]$, $\delta_{DOB}^{18}O‰$ = $[(\delta^{18}O‰)_{t=t}$ - $(\delta^{18}O‰)_{t=basal}]$ and $\delta_{DOB}^{17}O‰$ = $[(\delta^{17}O‰)_{t=t}$ - $(\delta^{17}O‰)_{t=basal}]$, respectively. Interestingly, we observed marked isotopic enrichments of $\delta_{DOB}D‰$ values in exhaled water vapor over the time for *H. pylori* negative persons, whereas a significant depletion of $\delta_{DOB}D‰$ values was observed for the *H.pylori* infected persons. Moreover, the experimentally obtained $\delta_{DOB}D‰$ values associated with the respiration were statistically significant ($p<0.005$) between *H.pylori*-positive and negative individuals during the 1-h excretion kinetics, thus unveiling a missing link between the isotopic fractionations of $HD^{16}O$ in exhaled breath and *H. pylori* infection in GI environment. However, the isotopic depletion of exhaled δD values for *H. pylori* infected subjects observed in our study is most likely responsible for hydrogen isotope-exchange as mentioned earlier. Early evidences [10, 12, 13] suggest that during this exchange process, molecular H_2 present in the GI tract may react with HDO to produce the HD and H_2O [H_2 (gas) + HDO (liquid/vapor) $\rightleftharpoons$ HD + H_2O], which may be catalyzed by hydrogenase enzyme secreted by *H. pylori* pathogen and

this may cause significant depletion of $\delta_{DOB}D‰$ values in exhaled breath samples. Our findings therefore suggest that the changes in $\delta D‰$ values of water in the proximal intestine may contribute to the pathogenesis of *H. pylori* infection and the exhaled $HD^{16}O$, so called semi heavy water, as a potential tracer for *non-invasive* assessment of this pathogen. Furthermore, in case of $\delta^{17}O$, we observed a slight difference of the excretion kinetics patterns between *H.pylori* positive and negative persons ($p<0.05$) but for $\delta^{18}O$, there were no statistically significant ($p>0.05$) fractionations observed between infected and non-infected individuals. Considering these results, our study is thus bringing a new dimension of knowledge for better understanding of the quadruple-isotopic fractionations of water-metabolism in the hydrogenase-mediated bacterial environment of the GI tract.
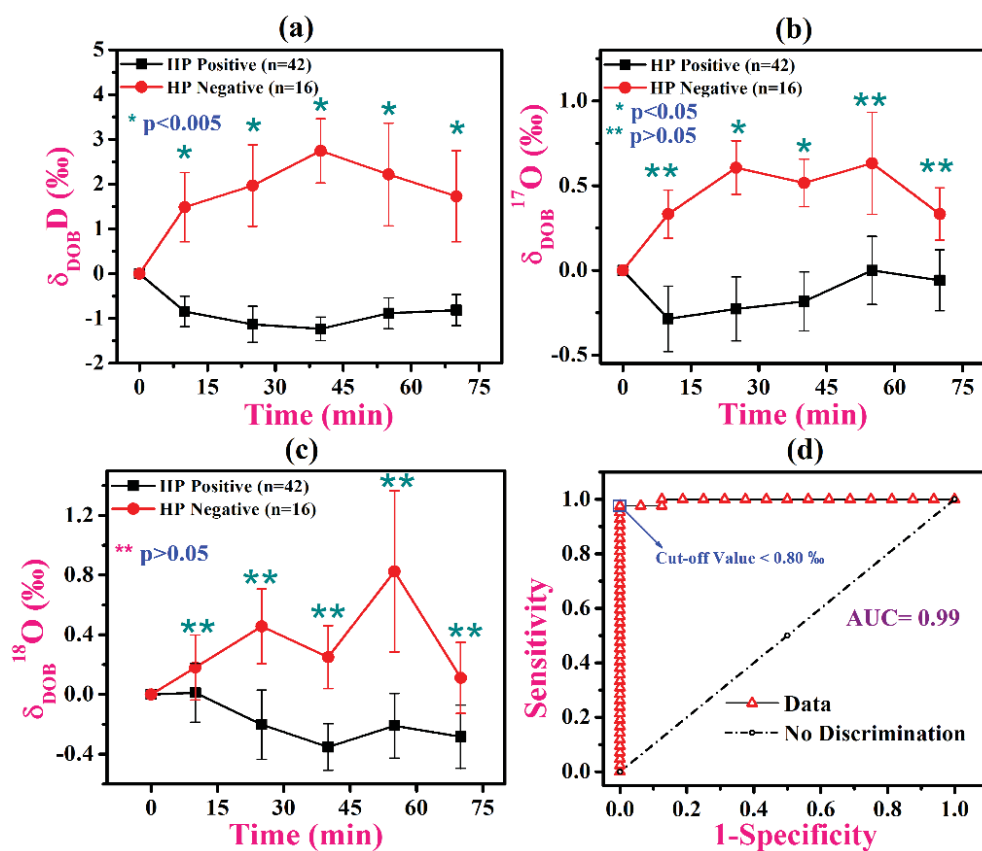

Fig.9.6. *Excretion kinetics of $\delta^{18}_{DOB}D‰$, $\delta^{18}_{DOB}O‰$ and $\delta^{17}_{DOB}O‰$ values of exhaled water vapor for H.pylori positive and H.pylori negative individuals (a, b, c). Values are mean ± SD. (d) Receiver operating characteristics curve (ROC) analysis for exhaled δD values; $\delta_{DOB}D‰$ (cut-off) < 0.8‰ at 30 min.*

Next, in an attempt to explore the potential clinical applications of isotopic fractionations of water in GI fluid linked with the respiration process, we determined the optimal diagnostic cut-off value of exhaled δD. We specifically utilized the respired δD isotope because the excretion kinetics for these isotopes were markedly distinct and statistically significant ($p<0.005$) between positive and negative persons (Fig. 9.6a). We used the receiver operating characteristics curve (ROC) analysis for exhaled δD values (Fig. 9.6(d) to understand the precise classification and diagnosis of *H. pylori* infection in a non-invasive manner. Our analysis revealed that individuals with $\delta_{DOB}D‰$ (cut-off) $< 0.8‰$ at 30 min in exhaled water vapor were considered to be *H. pylori* infected persons when the subjects were cross-verified with the gold-standard invasive endoscopy and biopsy-based rapid urease tests (RUTs). This corresponded to the diagnostic sensitivity of ~98% and specificity as close to 100% with an accuracy of 99%, thus introducing a new concept to distinctively track the *H. pylori* infection in GI tract through the isotopic signatures of water-metabolism in the human body.

9.3.8 Water isotopic fractionations associated with any kind of deformations of the GI tract

Finally, to gain a deeper insight into the isotopic fractionations of water associated with any kind of deformations of the GI tract, we performed critical assessments of *d-excess* and ^{17}O-*excess* values of the residual GI fluid.
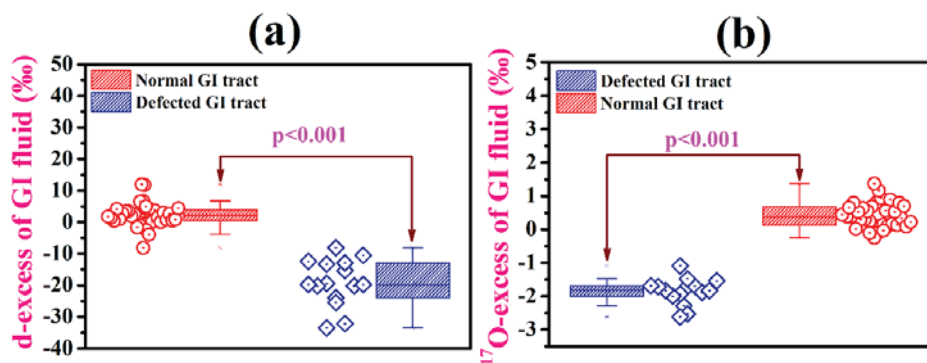
Fig.9.7. *Box-Whiskers plots of the quantitative variations of d-excess and ^{17}O-excess values in GI fluid between individuals with normal GI tract (n=35) and defected GI tract (n=15).*

The careful inspection on the data set in our experiment revealed that there are two distinct sets of data points for the second-order isotopic excess parameters within the individual group. The two data sets have been further illustrated in Fig. 9.7 and subsequently we evaluated these results with their corresponding gastrointestinal endoscopy reports.

A few representative endoscopic pictures of the various portions of the GI tract of the human subjects under study are shown in Fig. 9.8. We interestingly found that the magnitudes of *d-excess* and *^{17}O-excess* values of residual GI fluid have been highly depleted (about 4 to 6 times) in the individuals having deformed GI tract in the form of (I) gastric ulcer, (II) patchy gastritis, (III) pyloric channel ulcer, (IV) duodenal erosion, (V) active duodenal ulcer etc. in contrast to the individuals with normal GI tract. This observation directly supports the previous long-standing hypothesis that any deformation in GI tract might alter the isotopic fractionation of water during absorption through it. The findings also clearly indicate a higher degree of mass-dependence isotopic signatures during water absorption following the sequence of $HDO^{16} > H_2O^{17} > H_2O^{18}$ in presence of several defects of the GI tract.
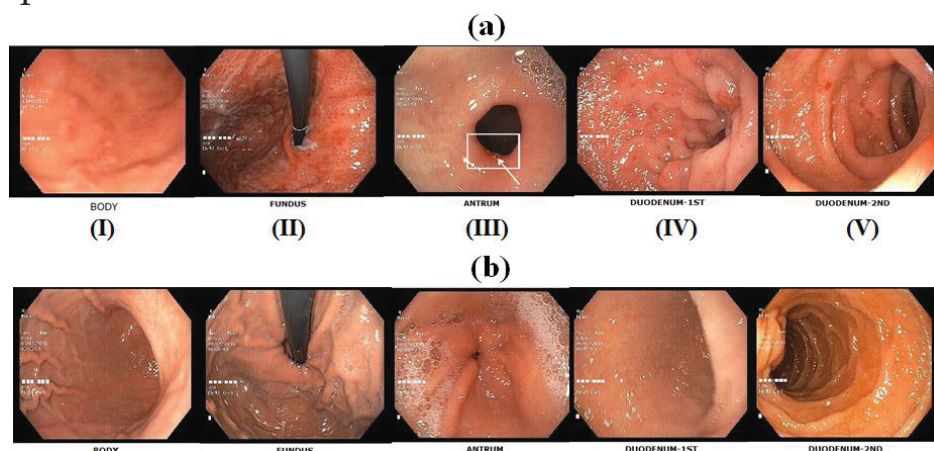
Fig.9.8. *Representative endoscopic pictures of the various portions of the GI tract of the subjects under study. (8a) represents various deformations or abnormalities of the GI tract in the form of (I) Gastric Ulcer **(P22)**, (II) Patchy gastritis **(P38)**, (III) Pyloric channel Ulcer **(P29)**, (IV) Duodenal erossion **(P6)**, (V) Active duodenal ulcer **(P6)**; (8b) represents endosocpic reports of normal GI tract **(N5)**.*

The GI fluid becomes more enriched in $\delta^{18}O$ and thus results in highly negative excess values. We therefore postulate that the isotopic

signatures of *d-excess* and ^{17}O-*excess* of water in GI fluid influenced by impaired or unusual water absorption can be used as tracers of onset of various deformations of the GI tract. These results when juxtaposed, provide the direct evidence for water-metabolism-derived quadruple-isotopic signatures to detect the defects of GI tract along with bacterial *H. pylori* infection therein. In a nutshell, various isotopic-signatures of water-metabolism involving different water-isotopolouges having different masses at various compartments of the body are depicted in Fig. 9.9
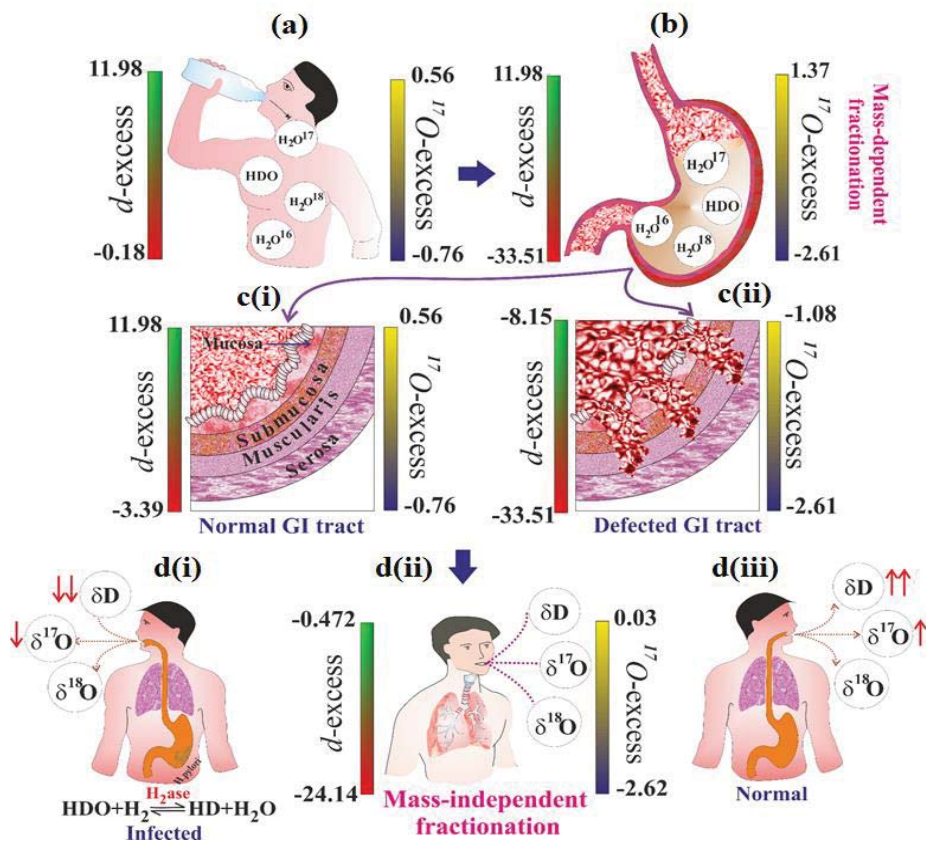
Fig.9.9 *Pictorial representation of the various isotopic signatures of water-metabolism in terms of d-and ^{17}O-excess values at the different compartments of the body: (a) Ingested drinking water; (b) absorption of water in GI fluid; c(i) & c(ii) distribution of the excess values in normal and defected GI tract conditions; and d(i) & d(iii) change in δD and δ^{17}O values during respiration in presence and absence of H. pylori pathogen; double upper and lower arrows represent highly enriched and highly depleted values, respectively whereas, single arrows correspond to moderate changes of the values; d(ii) distribution of excess values in the condition of mass-independent isotopic fractionations in the respiratory system. The values are not in scaled.*

9.4 Conclusions

In summary, we have given the first clear experimental evidences of quadruple-isotopic signatures of water-metabolism at the biological and physiological interface processes. Our study revealed the evidences of the mass-dependent isotopic fractionation of water in human GI tract, whereas mass-independent isotope exchange-reaction was observed in the respiratory system. This will deepen our understanding of the underlying mechanisms of isotopic fractionations of water and new data can be used as indices to quantify the isotopic fractionation processes as well as to disentangle the competing effects of fractionation during respiration. This study also provides evidences of the *H. pylori*-derived isotopic signature of HDO, so called semi heavy water, as a potential tracer for non-invasive assessment of the pathogen. In another application, we have also shown that the isotopic-signatures of impaired or unusual water absorption in GI tract can be used as tracers to track the onset of various defects or abnormalities in the form of gastric ulcer, patchy gastritis, pyloric channel ulcer, duodenal erosion, active duodenal ulcer etc., thus validating the long-standing hypothesis as mentioned earlier. These striking findings give new insight into the isotope-selective water-metabolism in human body and thus opening a new concept that will have enormous applications in human physiology and medical science. Finally, this study has made major advances in our understanding of water-metabolism-derived quadruple-isotopic signatures at the physio-bio interface in human body. This will allow us to explore a new arena of isotopic fractionations in chemical and biophysical processes involving different isotopologues of water.

9.5 References

[1] J. B. Leiper, Intestinal water absorption – implications for the formulation of rehydration solutions. *Int J Sports Med.* **19**, S129–S132 (1998).

[2] G. I. Sandle, Salt and water absorption in the human colon: a modern appraisal. *Gut.* **43**, 294-299 (1998).

[3] S. Epstein, L. Zeiri, Oxygen and carbon isotopic compositions of gases respired by humans. Proc. *Natl. Acad. Sci.* **85**, 1727-1731 (1988).

[4] S. P. O'Gradya, L. E. Enrighta, J. E. Barnettea, T. E. Cerlinga and J. R. Ehleringera, Accuracy and precision of a laser-spectroscopy approach to the analysis of δ^2H and $\delta^{18}O$ in human urine. *Isotopes in Environmental and Health Studies.* **46**, 476–483 (2010).

[5] D. W. Podlesak, A. Torregrossa, J. R. Ehleringer, M. D. Dearing, B. H. Passey, T. E. Cerling, Turnover of oxygen and hydrogen isotopes in the body water, CO_2, hair, and enamel of a small mammal. *Geochimica et Cosmochimica Acta.* **72**, 19–35 (2008).

[6] B. Luz, E. Barkan, M. L. Bender, M. H. Thiemens, K. A. Boering, Triple-isotope composition of atmospheric oxygen as a tracer of biosphere productivity. *Nature*, **400**, 547–550 (1999).

[7] B.Luz, E. Barkan, Variations of $^{17}O/^{16}O$ and $^{18}O/^{16}O$ in meteoric waters, *Geochimica et Cosmochimica Acta*, **74**, 6276-6286 (2010).

[8] C. Tian, L. Wang, K. F. Kaseke. B. W. Bird, Stable isotope compositions (δ^2H, $\delta^{18}O$ and $\delta^{17}O$) of rainfall and snowfall in the central United States, *Scientific reports*, **8**, Article number: 6712 (2018).

[9] A. Maity, M. Pal, S. Maithani, B. Ghosh, S. Chaudhuri, M. Pradhan, Molecular hydrogen in human breath: a new strategy for selectively

diagnosing peptic ulcer disease, non-ulcerous dyspepsia and *Helicobacter pylori* infection, *J. Breath Res.* **10,** 036007 (2016).

[10] A. Maity, M. Pal, S. Som, S. Maithani, S. Chaudhuri, M. Pradhan, Natural ^{18}O and ^{13}C-urea in gastric juice: a new route for non-invasive detection of ulcers, *Anal. Bioanal. Chem*. **409**, 193–200 (2017).

[11] J. P. Collman, Coupling H_2 to electron transfer**,** J. P. *Nat. Struct. Biol.* **3**, 213 (1996).

[12] S. Vogt. E. J. Lyon, S. Shima, R. K. Thauer, The exchange activities of [Fe] hydrogenase (iron–sulfur-clusterfree hydrogenase) from methanogenic archaea in comparison with the exchange activities of [FeFe] and [NiFe] hydrogenases, *J. Biol. Inorg. Chem*. **13**, 97–106 (2008).

[13] J. W. Olson, R. J. Maier, Molecular hydrogen as an energy source for Helicobacter pylori, *Science,* **298** 1788–1790 (2002).

[14] D. Leslie, K. Welch, W.B. Lyons, Domestic water supply dynamics using stable isotopes d^{18}O, dD, and d-Excess, *Journal of Water Resource and Protection*. **6**, 1517-1532 (2014).

[15] H. F. Yeh, J.W. Lee, Stable Hydrogen and Oxygen Isotopes for Groundwater Sources of Penghu Islands, Taiwan. *Geosciences*. **8**, 84 (2018).

Chapter 10

Summary of the thesis and Future perspective

10.1 Summary of the results

10.1.1 Simultaneous monitoring of stable hydrogen sulphide (H$_2$S) isotopes

The simultaneous monitoring of three stable isotopes of hydrogen sulphide (H$_2$S), i.e. H$_2^{32}$S, H$_2^{33}$S, and H$_2^{34}$S, within a single laser scan of 0.4 cm^{-1} has been achieved by means of a continuous-wave (cw) external-cavity quantum cascade laser (EC-QCL) coupled to high-resolution cavity ring-down spectroscopy (CRDS) near 7.5 µm. The measurement precisions of ^{32}S, ^{33}S, and ^{34}S isotopes of H$_2$S were found to be 1190 ppb, 13 ppb, and 124 ppb for the integration times of 264 sec, 261 sec, and 247 sec, respectively. The mode-hop-free (MHF) tunability (1257 cm^{-1} to 1340 cm^{-1}) of the EC-QCL was subsequently exploited to identify the interference-free 9 transition lines of H$_2^{32}$S and H$_2^{33}$S arising from the fundamental bending vibration (ν_2) for the trace detection of H$_2$S isotopes. A limiting sensitivity (1σ) of 20 ppb of total H$_2$S concentration was achieved for an integration time of 250 sec by targeting the transition of (4,4,1)→(5,5,0) centred at ~1292.857 cm^{-1}. Finally, simultaneous monitoring of multiple trace species such as CH$_4$, N$_2$O, and H$_2$S in a single laser scan of 0.05 cm^{-1} was demonstrated with high sensitivity and molecular specificity. The present study may lead to several potential future applications ranging from understanding of sulphur isotope geochemistry and fractionations to environmental sensing.

10.1.2 N$_2$O concentration measurement by employing CRDS technique in gastric environment

Over the past several decades, it has been generally believed that the microbial nitrification and denitrification are not significant processes in human gastrointestinal tract. Moreover, the underlying physiological link between exhaled nitrous oxide (N$_2$O) and aerobic denitrification in the gastric environment is still largely unknown. In this report, we provide the direct experimental evidence of aerobic denitrification process in human gastrointestinal tract by evaluating concentrations of dissolved N$_2$O and its precursor nitrite (NO$_2^-$) ion in the gastric juice along with exhaled N$_2$O concentration using high precision laser spectroscopy technique (CRDS). Moreover, in vitro studies of gastric fluid in patients reveal a new mechanism of nitrification of ammonium ion (NH$_4^+$) followed by denitrification of NO$_2^-$ leading to the formation of N$_2$O in gastric environment which is eventually excreted in exhaled breath. The observation was subsequently validated under in-vivo physiological conditions exploiting the urease activity of the gastric pathogen *Helicobacter pylori*. Consequently, our findings established a strong physiological link between exhaled N$_2$O and the bacterial infection in stomach. This deepens our understanding of the unusual microbial denitrification in the gastric environment, providing new insights into the activities of human-associated microorganisms which eventually affect the human physiology and health.

10.1.3 Spectroscopy study of C$_2$H$_2$

External cavity quantum cascade laser coupled cavity ring-down spectroscopy (CRDS) has been exploited here to quantify the rotational line intensities and N$_2$-broadening coefficients for both allowed $(\nu_4+\nu_5)^0$ and forbidden $(\nu_4+\nu_5)^2$ band of C$_2$H$_2$. The line intensities of $(\nu_4+\nu_5)^0$ band of C$_2$H$_2$ obtained from our CRDS set-up are in good agreement with the HITRAN and previously reported FTS studies. We reported N$_2$-broadening coefficient values for 16 P branch lines and 4 R branch lines of $(\nu_4+\nu_5)^0$ band and 5 P branch lines of $(\nu_4+\nu_5)^2$ band. Subsequently, we

determined the dipole moment of $(\nu_4+\nu_5)^0$ band from experimentally obtained line strength values.

10.1.4 Development and real time application of EC-QCL based gas sensor

We report a room-temperature continuous-wave (*cw*) mode-hop-free (MHF) external-cavity quantum cascade laser (EC-QCL) based mid-infrared methane (CH_4) sensor operating between 7.5 and 8 μm in the mid-IR molecular fingerprint region. We utilized the 2*f*-wavelength modulation spectroscopy (2*f*-WMS) for high sensitive monitoring of atmospheric CH_4. The strongest interference-free absorption-line in the ν_4 fundamental vibrational band of CH_4 centred at 1327.072 cm^{-1} was probed to achieve a minimum detection limit of 11 parts-per-billion (ppb) within a relatively small optical pathlength of 1.5 metre for an integration time of 272 seconds. The current cw EC-QCL with MHF frequency tuning capability exploiting the 2*f*-WMS detection strategy was subsequently employed for routine monitoring of trace CH_4 levels at the different anthropogenic sources present in the environment. Our findings suggest that the present QCL-based system could lead to the realization of a compact and field-deployable portable sensor for real-time routine monitoring of several other trace gases with high sensitivity and specificity within the tuning range of the laser.

10.1.5 Analysis of quadruple water isotopes using laser spectroscopy method

Water, the major body fluid in humans, has four main naturally occurring isotopologues, $H_2{}^{16}O$, $H_2{}^{17}O$, $H_2{}^{18}O$ and $H^2H^{16}O$ (i.e. $HD^{16}O$) with different masses. The underlying mechanisms of the isotope-specific water-metabolism in human gastrointestinal (GI) tract and respiratory system are poorly understood and remained illusive for several decades. Here, we present the direct experimental evidences of quadruple-isotopic signatures of water-metabolism at the interface of biological and physiological processes. Our study revealed the evidences of the kinetic mass-dependent isotopic fractionation of water in GI tract, whereas mass-independent isotope exchange-reaction was observed in the respiratory

system, thus offering a new way for understanding the underlying mechanisms involving different water-masses and also allowing to disentangle the competing effects of isotopic fractionation processes during respiration. In applications, we showed that water-metabolism-derived quadruple-isotopic signatures due to impaired or unusual water absorption in GI tract can be used as potential tracers to track the onset of various abnormalities along with bacterial infection therein. These findings are thus bringing a new dimension of knowledge for better understanding of the isotope-selective water-metabolism at the physio-bio interface in human body that will have enormous applications in human physiology and biomedical science.

10.2 Future Work

10.2.1 CRDS based Propofol sensor

Propofol has been used as an intravenous anaesthetic drug during surgery for sedating patients. Therefore, its real-time concentration monitoring in human exhaled breath is important to check the condition of a patient undergo surgery. The conventional mass spectrometry-based gas sensor has become less sensitive to detect propofol concentration as its estimated concentration is in the range of parts per billion (10^{-9}, ppb). Therefore, the quantitative measurement of propofol using high sensitive optical spectroscopy based method is suitable choice for online concentration tracking in clinical environment. As cavity ring-down spectroscopy has been proved its field deployment efficacy for measuring ultra-low concentration of trace molecules, thus it can be utilized for online propofol detection. From the NIST webbook, it has been found that propofol has strong line strength in 8 µm (within our QCL tuning range), which arises due to C-C or C-H stretching. So, our developed CRDS set up coupled with EC-QCL (as demonstrated in chapter 4) can be utilized to sense propofol by probing particular transition line, which has minimum interference with other essential trace molecules in exhaled air.

10.2.2 Development of cavity enhanced absorption spectroscopy technique coupled with wavelength modulation strategy

In chapter 3, it has been elaborated that cavity-enhanced spectroscopy technique associated with wavelength modulation (WM) approach can be utilized to obtain ultra-high sensitivity up to parts per trillion (10^{-12}, ppt) level due to its simultaneous noise reduction and optical path enhancement properties. This detection strategy is also useful for sensing multi trace molecules irrespective of their overlapping absorption lines in atmospheric pressure.